UNIVERSIDADE FEDERAL DE MINAS GERAIS
Instituto de Ciências Exatas
Programa de Pós-graduação em Física

Rafael Ricardo Rojas López

CHARGE AND SPIN DYNAMICS IN TWO-DIMENSIONAL SEMICONDUCTORS

Belo Horizonte
2023

Rafael Ricardo Rojas López

CHARGE AND SPIN DYNAMICS IN TWO-DIMENSIONAL SEMICONDUCTORS

Thesis presented to the Graduate Program in Physics of the Instituto de Ciências Exatas of the Universidade Federal de Minas Gerais and the Zernike institute for Advanced materials of the University of Groninge as a partial requirement to obtain the title of double PhD degree in Physics.

Supervisor: Paulo Sérgio Soares Guimarães
Co-supervisor: Marcos Henrique Diniz Guimarães
Co-supervisor: Caspar H. van der Wal

Belo Horizonte

2023

Dados Internacionais de Catalogação na Publicação (CIP)

R741c Rojas López, Rafael Ricardo.
Charge and spin dynamics in two-dimensional semiconductors / Rafael Ricardo Rojas López. – 2023.
114f. : il.

Orientador: Paulo Sérgio Soares Guimarães.
Coorientadores: Marcos Henrique Diniz Guimarães e Caspar H. van der Wal.
Tese (doutorado) – Universidade Federal de Minas Gerais, Departamento de Física.
Bibliografia: f. 96-113.

1. Semicondutores. 2. Propriedades ópticas. 3. Heteroestrutura. I. Título. II. Guimarães, Paulo Sérgio Soares. III. Guimarães, Marcos Henrique Diniz. IV. van der Wal, Caspar H. V. Universidade Federal de Minas Gerais, Departamento de Física.

CDU – 537.311.322 (043)

Ficha catalográfica elaborada por Romário Martins Ribeiro – CRB6 3595
Biblioteca Professor Manoel Lopes de Siqueira – Departamento de Física - UFMG

Universidade Federal de Minas Gerais
Instituto de Ciências Exatas
Programa de Pós-Graduação em Física
Caixa Postal 702
30.123-970 Belo Horizonte - MG - Brasil

Telefone (xx) (31) 3409 5637
(xx) (31) 3409 5633
Fax (xx) (31) 3409 5688
(xx) (31) 3409 5600
e-mail pgfisica@fisica.ufmg.br

ATA DA SESSÃO DE ARGUIÇÃO DA 421ª TESE DO PROGRAMA DE PÓS-GRADUAÇÃO EM FÍSICA, DEFENDIDA POR RAFAEL RICARDO ROJAS LOPEZ orientado pelo professor Paulo Sérgio Soares Guimarães e coorientado pelos professores Marcos H. Diniz Guimarães e Caspar H. van der Wal, para obtenção do grau de **DOUTOR EM CIÊNCIAS, área de concentração Física**. Às 11 horas e 15 minutos de três de outubro de dois mil e vinte e três reuniu-se, na Sala Magna da University of Groningen, The Netherlands, a Comissão Examinadora, composta pelos professores **Paulo Sérgio Soares Guimarães** (Orientador - Departamento de Física/UFMG), **Marcos H. Diniz Guimarães** (Coorientador - University of Groningen), **Caspar H. van der Wal** (Coorientador - University of Groningen), **Leandro M. Malard** (Departamento de Física/UFMG), **Simone S. Alexandre** (Departamento de Física/UFMG), **J. Gerard Roelfes** (University of Groningen), **Jianting Ye** (University of Groningen) e **Jagoda L. Slawinska** (University of Groningen) para dar cumprimento ao Artigo 37 do Regimento Geral da UFMG, submetendo o Mestre **RAFAEL RICARDO ROJAS LOPEZ** à arguição de seu trabalho de Tese de Doutorado, que recebeu o título de **"Charge and spin dynamics in two-dimensional semiconductors"**. O candidato fez uma exposição oral de seu trabalho durante aproximadamente 50 minutos. Após esta, os membros da comissão prosseguiram com a sua arguição, e apresentaram seus pareceres individuais sobre o trabalho, concluindo pela aprovação do candidato.

Groningen, 03 de outubro de 2023.

Paulo S. S. Guimarães, orientador, UFMG

Marcos H. D. Guimarães, co-orientador, University of Groningen

Caspar H. van der Wal, co-orientador, University of Groningen

Leandro M. Malard, UFMG

Simone S. Alexandre, UFMG

Jianting Ye, University of Groningen

Jagoda L. Slawinska, University of Groningen

J. Gerard Roelfes, University of Groningen, The Netherlands

Candidato: Rafael Ricardo Rojas Lopez

A mis padres Rosaura y Ricaurte
y a mi hermana Yamile

Acknowledgements

Finishing my Ph.D. makes me reflect on the long academic journey that I started back in 2010, little knowing that it would bring me to this day. Becoming a doctor in Colombia is a privilege that very few can achieve. That is why I want to start by thanking the first person who set me on this path, **Herbert Vinck**. I am sure that his efforts to encourage students to critical thinking and choose an academic career have changed the lives of many people, including my own. I look forward to the day when Colombia can provide more opportunities for students with limited financial means to fully pursue their careers there.

I would like to thank my supervisors because I was very lucky to have not just great scientists, but also great guides through this hard path. **Paulo**, I will always be very grateful to you as, from the first day in Brazil, you have been supportive, present, and always willing to help me in all academic, bureaucratic, and life-related struggles. Your experience and approachable nature have been of central importance to my formation. **Marcos**, thanks for helping me to understand the ways of modern academic life, how to improve my academic skills, and how to speed up my workflow. Your passion for physics and time management skills are very inspiring, I hope one day I can get there myself. I am honored to be one of your first PhD students. Also, I am very happy about your recent promotion, all my best wishes to you and your group. **Caspar**, thanks for your support and help whenever it was necessary.

I want to thank Professors **Maxim Pchenitchnikov**, **Leandro Malard**, **Alberto Curto**, and **Jaroslav Fabian** for being part of my reading committee, and Professor **Simone Alexandre** for being part of my examination committee. Feedback is always a great opportunity for improvement.

Now, I want to thank the people who helped me at different stages of my journey.

To the people from the LCPNano: **Amanda**, **Daniele**, and **Diego** for your help whenever needed with the WiTec. Also, to the staff from the NanoLabNL. **Johan**, thank you for your help with moving the cryostat and in general for keeping the laboratories running. Furthermore, thank you for keeping us safe and ensuring we are not overworked. It can be tricky close to the deadlines, but it is important to stay healthy. **Hans**, thank you for your help with cryogenic-related demands. **Frits**, thank you for your help with the design and production of mechanical pieces. It was nice to share an office with you, always in a good mood and designing perfect pieces for the group. To **Marleen**, **Ana Luiza**, and **Marilia** thanks for your help and assistance with all kinds of bureaucratic matters.

I would also like to thank **Bart van Wees** for his academic feedback during the FND group meetings. They helped me to reflect on my results and improve my presentation skills. **Bernardo Neves**, thank you for the collaboration in our work. Your comments and guidance regarding the KPFM technique were essential for the understanding of our results. **Maíra**, thank you for your dedication to the KPFM measurements, but also for the conversations and good memories we share together in the group. I want to thank **Silvia Alencar** for his support and assistance with all the documentation needed in the last stage of my PhD.

I had the fortune of doing my master's and PhD in the Semiconductors laboratory at UFMG. There, I met **Henrique**, **Túlio**, and **Juliana**, who supported me and became good friends. Thank you for the wonderful times and engaging scientific and philosophical conversations. I always found myself reflecting upon topics after our discussions. You are all great scientists and I wish you a great careers. I also want to thank **Ingrid**, **Bárbara**, **Thiago**, and **Campo**, the old members of the group from whom I learned, discussed, and shared different moments of my PhD. From Groningen, I want to thank the people from the big FND group: **Jan**, **Adam**, **Cédric**, **Aaron**, **Rixt**, **Feng**, **Dennis**, **Alexey**, **Xu**, **Obed**, **Frank**, **Xiangyang**, **Joop**, **Job**, **Tian**,**Talieh**, **Anouk**, **Azminul**, **Perihan**, **Crystal**, **Ping**, and **Boxuan**, thank you for receiving me well into the group. It was always fun and pleasant to share time during group outings, at lunch, or on any occasion.

Being a foreigner can be a challenging experience. In Brazil, I was lucky enough to meet **Alix**, **Eduard**, **Gaby**, and **Ezequiel**. Thank you, because you were my Brazilian family, with all kinds of fun, happy, and good times during our time living together. Pandemic times were challenging, but by facing it together, we managed to overcome many difficulties. **Raúl**, **Luis Pedraza**, **Luis Elvis**, **Milena**, little **Vicky**, **Paty**, **Vicky**, **Pilar**, **Leo Calasanz**, **Manuel**, **Manuela**, **Juliana**, **Gustavo**, **Alfonso**, and all the friends I made in Brazil, thanks for all the happy memories I have with you. My time in Brazil was much better because of you. I want to thank my paranymph **Anna**. My time in the Netherlands gave us the chance to spend more time together and grow closer. Thank you for the good moments living together. I appreciate how you always offered me your

help and invited me to your plans. **Feitze**, thanks for your help moving out when, at that time, you did not even know me. You became a very good friend and it was always nice to share a tea, a meal, or play a game. **Niels**, thank you for your kindness. Also, thanks for all the meals and the good talks. **Freddie**, I am glad we crossed paths. Thanks for your help and patience working together with the Cryovac. Also, thank you for introducing me to Pandas and Pymeasure; they became some of my most appreciated skills. And thank you for always being there to lend a hand, inviting me to climb, and simply being a friend. **Carmem**, thank you for receiving me in the Netherlands. But in particular, thank you for inviting me for Christmas. That night with your family was heartwarming. **Sytze**, it was very nice to share an office with you. Thank you for your kindness, for always being willing to help, and for the academic and non-academic conversations. Your impressive memory and the interesting facts you shared during our chats were always enjoyable to hear. **Carolina**, **Diego**, **Lina**, **Dinorah** my Hispanic crew in the Netherlands. It was nice to speak some Spanish far away from home, share experiences, or dance salsa. **Mauricio**, **Camilo**, **Lorena**, and all my friends in Colombia, thank you for your support despite the distance.

Among my friends, two of them hold a special place in my life. **Luisa**, we shared a long path from Colombia to Brazil for our PhD. Thank you for your company, friendship, our shared party plans, and engaging political and philosophical discussions that provided a very needed break from work. **Sergio**, thanks for your support and loyal friendship despite the distance all these years. Thank you for helping me with the design of the thesis cover. I was glad to count on you for this.

To conclude, and of utmost significance, I want to thank my family. Gracias **papá** y **mamá**, sólo por ustedes es que he podido llegar hasta aqui. Sus enseñanzas, su apoyo, y su amor me guian y me dan fuerzas para seguir cada dia. A mi hermana, **Yamile**, por su apoyo y cariño. Porque la fuerza, determinación y persistencia con sus proyectos me han inspirado a seguir su ejemplo en mi propio camino. A **Chris** por su cariño, generosidad, y buena energía cuando nos encontramos. Gracias a **Dani** porque, aunque sin saberlo, con su ternura le ha sacado varias sonrisas a su tio, especialmente valiosas en medio del estrés por escribir su tesis. À minha namorada **Juliana**, pelo seu grande apoio, amor e parceria, fundamentais para me fortalecer a cada dia. Obrigado por escolher ser minha companheira nesta jornada, mesmo diante dos desafios da vida acadêmica, como foi durante o meu tempo na Holanda. Mucas gracias tambien a todos mis **tios**, y **primos** que siempre se preocuparon por mi, y me apoyaron para que siguiera adelante. Muito obrigado a **Patricia**, **Poliana**, **Paulo** e **Paola**, minha nova familia Brasileira que me acolheu com muito carinho nessa fase final do doutorado. Merci à **Marie Claude**, **Christian**, et **Antoine** ma famille française, pour votre soutien et affection.

I am thankful to the funding agencies CAPES, CNPq, FAPEMIG, and NWO, as

well as to the Zernike Institute for Advanced Materials and the Physics Department of the Universidade Federal de Minas Gerais for the financial support that made possible this thesis.

Thanks Brazil and the Netherlands

Resumo

Os materiais em camadas bidimensionais (2D) abriram uma das áreas mais promissoras da física do estado sólido, pois fornecem uma ampla gama de fenômenos físicos em nanoescala, adequados para física aplicada e fundamental. Os dicalcogenetos de metais de transição semicondutores (TMDs, na sigla em inglês) estão entre os materiais em camadas mais estudados devido ao seu caráter bandgap direto com propriedades excitônicas robustas. Além disso, seu forte acoplamento spin-órbita fornece a esses materiais uma rica física relacionada ao spin que pode ser explorada em campos como a opto-spintrônica. Nesta tese, estudamos opticamente a dinâmica de carga e spin de TMDs semicondutoras quando em contato com substratos de arsenieto de gálio (GaAs) e ao aplicar um campo magnético externo. Nós encontramos que quando os TMDs semiconducting são colocados em GaAs há uma transferência da carga entre eles. Isso pode resultar na dissociação ou transferência completa dos excitons de um material para o outro, que pode ser controlada escolhendo a dopagem do substrato, ou usando diferentes TMDs como MoS_2 ou WSe_2. Além disso, estudamos a dinâmica de spin de uma monocamada de $MoSe_2$ sob um campo magnético externo perpendicular ao plano da amostra. Observamos que o campo magnético pode efetivamente controlar a dinâmica de spin na monocamada, de acordo com uma rápida transferência de buracos entre os estados do vale presentes neste material. Portanto, nossos resultados fornecem referências iniciais sobre a dinâmica de carga e spin em semicondutores 2D, dependendo do substrato e dos campos magnéticos aplicados, o que pode permitir sua aplicação em novos dispositivos.

Palavras-chave: Dicalcogenetos de Metais de Transição, GaAs, MoS_2, WS_2, WSe_2, heteroestrutura, monocamada, óptica ultrarrápida, dinâmica de cargas, propriedades ópticas.

Abstract

Two-dimensional (2D) layered materials have opened one of the most promising areas in solid state physics, as they provide a broad range of physical phenomena in the nanoscale, suitable for applied and fundamental physics. Semiconducting transition metal dichalcogenides (TMDs) are among the most studied layered materials due to their direct bandgap character with robust excitonic properties. Moreover, their strong spin-orbit coupling provides these materials with a rich spin-related physics that can be explored in fields like opto-spintronics. In this thesis, we optically study the charge and spin dynamics of semiconducting TMDs when in contact with gallium arsenide (GaAs) substrates and when applying an external magnetic field. We found that when semiconducting TMDs are placed on GaAs there is a charge transfer between them. This can result in the dissociation or full transfer of the excitons from one material to the other, which can be controlled by choosing the doping of the substrate, or by using different TMDs such as MoS_2 or WSe_2. Furthermore, we study the spin dynamics of monolayer $MoSe_2$ under an external magnetic field perpendicular to the sample plane. We observe that the magnetic field can effectively control the spin dynamics in the monolayer, in agreement with a fast hole transfer between the valley states present in this material. Therefore, our results provide initial benchmarks on the charge and spin dynamics in 2D semiconductors, depending on their substrate and applied magnetic fields, which can enable their application in novel devices.

Keywords: Transition metal dichalcogenides, GaAs, MoS_2, WSe_2, $MoSe_2$, 2D materials, monolayer, ultrafast optics, charge dynamics, optical properties.

Contents

CHAPTER 1

Introduction

The technological revolution that we have experienced in the last twenty years is without any doubt one of the biggest and fastest in history. Within this process, it has become routine for us to see the release of more powerful smartphones, laptops, and all kinds of technological devices coming out each year. This is the result of a deep understanding of matter, light, and their mutual interaction which allows us to find new ways for controlling the physical phenomena involved in the design of those devices. Nevertheless, miniaturization and the demand for high computing capability are pushing the industry to new limits, with challenges such as higher importance of quantum effects on nanodevices as well as their high energy consumption. The discovery of new materials plays a central role in optimizing the performance of components, such as transistors, required for further size reduction.

The discovery of graphene and its properties in 2004 [1] became of high interest as a possible solution to the next generation of nanotechnology. This new material consisting of a monoatomic carbon layer exhibits several attractive properties such as high flexibility, excellent electrical conductivity than metals, and very high tensile strength, among others. However, despite these attractive features, its lack of electronic bandgap is a disadvantage for many applications. Fortunately, the success of graphene drove attention towards van der Waals crystals, resulting in the discovery of hundreds of new atomically-thin materials with all kinds of properties. Within the more relevant, we can find black phosphorus (BP), hexagonal boron nitride (hBN), transition metal dichalcogenides (TMDs), and layered ferromagnets, among others, that emerged to increase the range of possible applications of bidimensional materials by simply combining and stacking them.

In this thesis, we will focus on the study and characterization of the semiconductor

group of the transition metal dichalcogenides. In particular, we will focus on the study of the effects of the environment, such as the substrate, and the magnetic field, on the optical properties and the charge and spin dynamics of monolayers of TMDs. We envision our results as a tool for a better understanding of these materials and a path through control and application of those properties in the area of optoelectronic- and optospintronic nanodevices. In this chapter we introduce the central theoretical concepts, starting by the definition and main properties of the TMDs and how they interact with external out-of-plane magnetic fields. Afterwards, we will describe some environmental and proximity effects on the properties of TMDs, as for instance impurities and the dielectric constant of the substrate. We also present a brief state-of-the-art on the dynamic and non-equilibrium processes of optically excited charges and spins in semiconducting TMDs. Finally, we present an outline of this thesis to guide the reader through the content of the different chapters.

1.1 Transition Metal Dichalcogenides

Transition metal dichalcogenides are a family of materials with the form MX_2, with M a transition metal such as molybdenum or tungsten (Mo, W), and X a chalcogenide element such as sulphur or Selenium (S, Se) (see Figure 1.a). They are hexagonal multilayer structures, with X-M-X covalent bonds within a layer and van der Waals bonds between layers. This graphene-like configuration allows the fabrication of monolayer samples through techniques such as mechanical exfoliation or chemical vapor deposition (CVD).

One of the most attractive properties of these materials is their transition from an indirect bandgap semiconductor in the bulk to a direct bandgap in the monolayer limit (see Figure 1.b). The latter enables a more efficient band-to-band excitation and recombination making it more attractive for optical and electronic applications [2–4]. This transition substantially amplifies the intensity of light interaction, producing photoluminescence in the visible and near-infrared regions. Their crystal properties make the binding energy of the excitons one of the largest observed in semiconductors, reaching values of hundreds of meV [5]. This also favors the emergence of charged excitons (trions) that open new possibilities and applications by controlling the lineshape of the emission of the monolayer [6, 7]. Section 2.3 will discuss further details of excitonic phenomena.

Additionally, monolayer TMDs possess unique spin-related properties that make them particularly appealing for a field of nanotechnology called spintronics. The d-orbitals of the transition metal give rise to a strong spin-orbit coupling (SOC), which is especially relevant at the $K_\pm$ points, or valleys, of the Brillouin zone, Figure 2a [8]. When transitioning from a bulk to a monolayer structure, the inversion symmetry is broken, giving rise to coupled spin and valley physics [8–11]. The two valley species are energy degenerated and

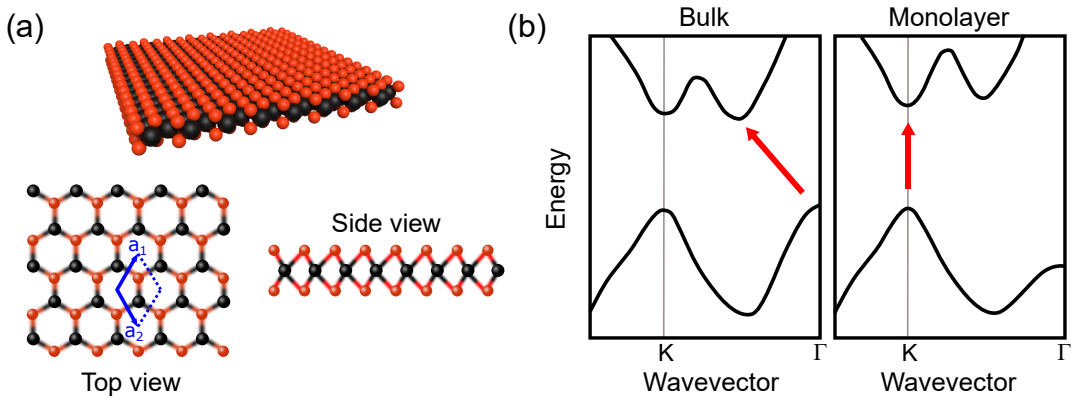

Figure 1 – (a) Representation of the crystal structure of a monolayer TMD in various angles. (b) Transition of the band structure from bulk to monolayer illustrated. The red arrows represent the lowest energy electronic transition from the valence band to the conduction band at each panel.

with spin states connected via time-reversal symmetry (Figure 2b). These properties enable optical control of the injection or detection of spin-polarized carriers in the material by using circularly polarized light. Electronic spins up (+1/2) and down (-1/2) can be excited at different valleys of the conduction band of the material, facilitating the generation, manipulation, and study of electronic spins [12–14].

Over the last ten years, the study of these properties keeps rising and the results are highly promising for the development of more efficient (nano)devices in areas as (opto)electronics [15–18], (opto)spintronics [19–22] and basic research as in works of single-photon generation [23] and polaritonics [24].

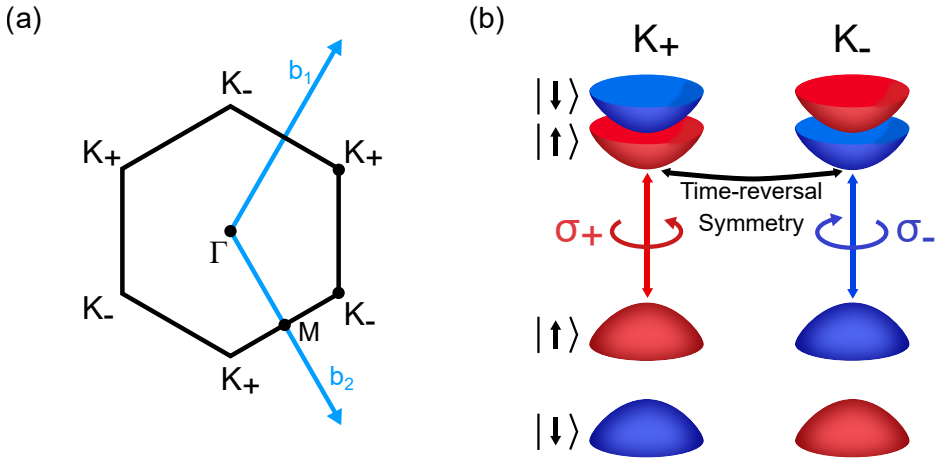

Figure 2 – (a) Reciprocal lattice with the main high symmetry points and the unit vectors of the first Brillouin zone. (b) Representation of the band structure at the high symmetry K_+ and k_- points with their spin state configuration.

1.1.1 Spin state configuration

As the electronic states involved in the direct bandgap transitions are mainly related to the transition metal atoms, there are two spin-state configurations in semiconducting TMDs: molybdenum-based and tungsten-based (Figure 3). According to optical selection rules, an electron at the top of the valence band can only transition to an electronic spin state in the conduction band that has the same spin as the initial state [8, 9, 25]. For molybdenum-based TMDs, this results in a direct relationship between the lower and higher states of the conduction and valence band, respectively. On the other hand, for tungsten-based materials, we have to excite the electrons to a higher energetic state in the conduction band. This increases the role of dark transitions in tungsten-based monolayers [26, 27]. When using out-of-plane excitation, electrons with a spin s are unable to transition to states with different spins, whether they are in the conduction or valence band. For instance, if an electron relaxes to the lowest conduction band state via a spin-flip scattering process, it will become prohibited for the electron to relax back to the valence band state through radiative recombination [28]. For this reason, they are called dark states.

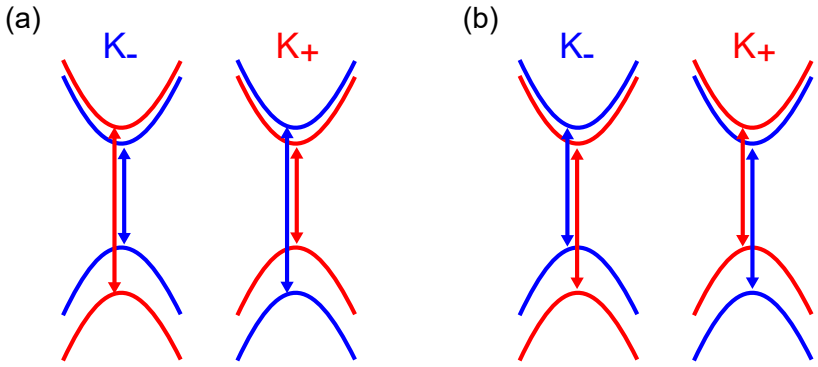

Figure 3 – (a) Band structure representation, near the $K\pm$ points, of molybdenum-based TMDs, and for (b) tungsten-based TMDs.

1.2 The valley-Zeeman effect

When an external magnetic field is applied perpendicular (out-of-plane) to the monolayer surface, the spin states will interact with it generating a Zeeman energy shifting. For TMDs, we can describe the energy shift as $-\vec{\mu} \cdot \vec{B}$, and in the case of a monolayer lying in the xy plane, it can be expressed as $\mu_z B_z$, with μ_z representing the total magnetic moment that couples with the field. To determine this magnetic moment, we will focus on the electrons in the Bloch states at the band edge *i.e.* the K_+ and K_- points, where the direct electronic transitions occur. For TMDs, the total magnetic moment consists of two components: spin and valley/orbital contributions [29–33].

The first component, the spin, will have the usual behavior with the magnetic field, where opposite-spin states shift their energy in the same amount but in opposite directions. Therefore, the usual spin magnetic-dipole moment of the electron will describe this contribution as $\mu_s^{c,v} = -s\mu_B$, with μ_B the Bohr magneton of the electron and $s = \pm 1$ a spin direction index. However, this will not reflect a change in the resonances of $K_\pm$ valleys as in both cases the energy shift is naively the same and the optical transitions conserve the spin.

The second component can be naively understood as the contribution of two parts. The first one is the orbital angular momentum, also called intracellular contribution, which depends on the properties of the specific atomic states involved in the transitions at the $K_\pm$ points. As mentioned before, the origin of these states is the d-orbitals of the transition metal. However, different orbitals compose the valence and conduction bands. The latter has its origin mostly in the d_{z^2} orbital, which possesses a zero angular momentum contribution $m_l = 0$ and results in a zero magnetic moment for the conduction band $\mu_l^c = 0$. On the other hand, the states at the top of the valence band at the $K_\pm$ points arise from the hybridization of the $d_{x^2-y^2}$ and d_{xy} orbitals in the form $d_{x^2-y^2} \pm i d_{xy}$, where the +(-) sign refers to the K_+ (K_-) valley. In this case, the electronic configuration will provide an azimuthal angular momentum along the z axis of $m_l = \pm 2\hbar$, resulting in a magnetic moment of $\mu_l^v = -(e/2m_e)l_z = \mp 2\mu_B$ [8, 9, 30–33].

Finally, the valley/orbital component is a wave-function-related contribution that arises from the particular winding configuration of the Bloch function at the K_+ and K_- points. Due to the origin of this component, also called intercellular contribution, which needs to take into account the neighbor states, it is common to use for instance a two-band [30, 32] or three-band [33] tight-binding model to determine the magnetic moment contribution. In a simple approach, we can assume symmetry of the electron-hole configuration and therefore the calculations lead to a magnetic moment contribution of $\mu_k^{c,v} = -\tau\mu_B(m_e/m_{eff})$ where m_e is the mass of the free-electron, m_{eff} is the electron-hole symmetric carrier effective mass and $\tau = \pm 1$ the valley quantum number. Otherwise, for a more precise approach, the electron-hole symmetric mass should be broken and consider the independent masses of each band, simply resulting in exchange m_{eff} by the effective masses of the conduction (m_{eff}^c) and valence (m_{eff}^v) bands.

With all the individual contributions determined, we can now calculate the expected energy shift due to the interaction with the magnetic field. First, we will calculate the change in the conduction band which is given by $\Delta E_c = -(\Delta\mu_s^c + \Delta\mu_l^c + \Delta\mu_K^c)B_z$ where we have defined the difference on magnetic momentum as $\Delta\mu = \Delta\mu_{k_+ - k_-}$. As the two K valleys have opposite spin and valley quantum numbers, this will leave us with $\Delta E_c = -(-2\mu_B - 2\mu_B(m_e/m_{eff}))B_z$. For the case of the valence band, the spin and valley function contribution will be similar but this time we will have the orbital angular

momentum contribution that leaves us with an energy shift of $\Delta E_v = -(-2\mu_B - 4\mu_B - 2\mu_B(m_e/m_{eff}))B_z$. We can now calculate the total Zeeman effect as $\Delta E = \Delta E_c - \Delta E_v$, that lead us to

$$\Delta E = -4\mu_B B_z. \tag{1.1}$$

This total shift in energy can be more easily understood through Figure 4.a where each contribution is represented with arrows. We obtain in this way a breaking of the energy and valley degeneracy, with each valley having a different energy state and a different bandgap. As the energy breaking arises from the different origin of the band states in the conduction band and the unique valley properties of this system, this effect is also called the *valley Zeeman effect*.

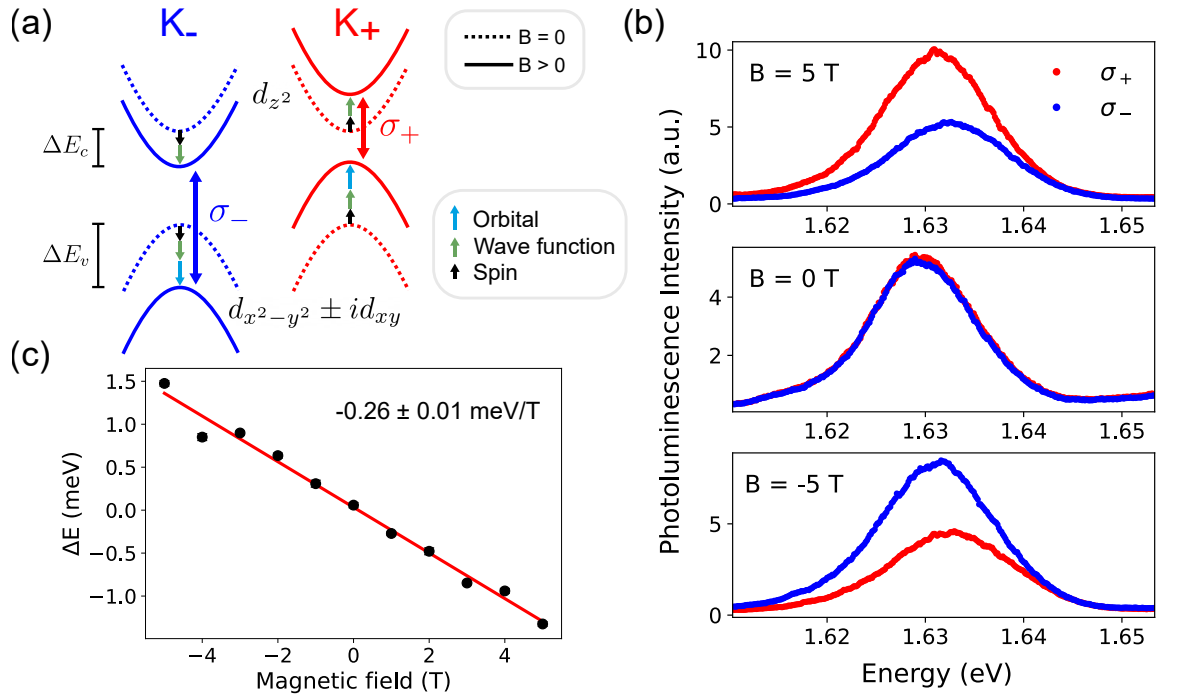

Figure 4 – (a) Representation of the $K_\pm$ band shift under a positive magnetic field. The black, cyan, and green arrows represent the different contributions to the band shift. (b) Photoluminescence spectra of a monolayer $MoSe_2$ showing the break of the valley energy degeneracy at high magnetic fields. (c) The extracted difference of the photoluminescence peaks $E_{\sigma_+} - E_{\sigma_-}$ at different magnetic fields presenting a linear behavior. Measurements performed by the author as part of the analysis for chapter 5. T = 6 K.

One way to track the change in energy is by measuring the photoluminescence with circularly polarized light to excite and measure excitons at a specific valley. In Figure 4b we see how the energy emission of valley K_+ (K_-) shifts towards a lower (higher) energy when a positive magnetic field is applied. Also, by symmetry, we observe how the shift in

energy switches when we reverse the direction of the magnetic field to a negative value. Therefore, we can characterize the magnetic response of the material by determining a magnetic g^{vl}-factor of one valley. For this, we can define the following relation [29, 32]

$$E_{\sigma_+} - E_{\sigma_-} = g^{vl}\mu_B B \tag{1.2}$$

where $E_{\sigma_\pm}$ is the center of the peak of photoluminescence emission when detecting the light of the valley excited by $\sigma_\pm$ polarized light. Hence, we can write

$$g^{vl} = \frac{E_{\sigma_+} - E_{\sigma_-}}{\mu_B B} \tag{1.3}$$

and characterize the valley change by measuring the difference of the emission peaks of two valleys excited circularly polarized at different magnetic fields. Figure 4c presents this difference for the case of a monolayer of $MoSe_2$ resulting in $g^{vl} = -4.5 \pm 0.2$. This experimental result is consistent with other reports [32] but it is also consistent with the result in Equation 1.1 through the simple relation $E_{\sigma_+} - E_{\sigma_-} = \Delta E_c - \Delta E_v$.

It is worth noting that in our previous analysis, we should have considered the change in the exciton binding energy due to the magnetic field. However, as this dependence is expected to be quadratic with the field and therefore, not observed in the experiments, the binding energy is assumed to be constant over the magnetic fields [34, 35]. Finally, the previous experimental and theoretical analysis can be clearly understood for the case of excitons, nevertheless, the analysis of the trion peak dependence can be more complex [30–33]. In the different reports, the trion dependence with the magnetic field presents divergences, mostly for the tungsten-based TMDs, where dark states become of high importance [33, 36]. As trions are a three-carrier compound system, its analysis may need a deeper description of the possible state configurations where also different recombination paths may play an important role in photoluminescence peak. In this thesis, our focus will be on $MoSe_2$ monolayer that has been reported to exhibit a magnetic field dependence of the trion peak very similar to the exciton behavior [30, 32].

In case of interest in a first principles calculation analysis, we refer the reader to the theoretical studies described in references [37, 38].

1.3 Environmental and proximity effects

Many of the interesting phenomena of 2D materials, such as TMDs, arise from the change in the properties of the material in the transition from bulk to the single layer. However, the ultra-thin character of these layers results in a high sensitivity to their environment and proximity effects that end up modifying their physical properties.

Within the environmental effects we can include their interaction with gases, for instance with the air, that can degrade the monolayers by generating oxidation in chalcogen vacancies [39]. Despite that semiconducting TMDs are considered air-stable, it is common to have chalcogen vacancies in single layers, either from their synthesis or in the edges of the flakes [40]. When interacting with the air, the defects in the lattice allow the oxidation and degradation of the sample that modify the properties of the pristine material, such as the conductivity or optical quantum-efficiency [41]. This characteristic is the core idea in the fabrication of gas sensors based on TMDs, where the natural interaction of the monolayer with determined gases can be enhanced by the deposition of particles and produce promising sensors [42].

The reduced dimensionality of monolayer TMDs makes them highly sensitive to their dielectric environment, which can significantly alter their intrinsic properties. In particular, the Coulomb interaction that mediates the excitonic properties of TMDs can be strongly influenced by a substrate with a strong dielectric effect. In the case of high dielectric constants, the binding energy of the excitons, trions, and even the electronic band gap of the monolayer are modified. This effect can be even more problematic if we consider the case of a single layer that is not in homogeneous contact with the substrate, resulting in a flake with variations of the properties along the surface [43].

Another effect related to the substrate is the charge transfer to/from the monolayer. Depending on the material of the substrate (*e.g.* metal, semiconductor) the interaction with the TMD will result in a charge transfer between the materials to reach electrostatic equilibrium. In this case, the change in the charge density of the monolayer can result in a different response of electric transport or intensity of emission of charged excitons (trions).

Furthermore, the substrate can also induce interference effects depending on the sample configuration. This effect is particularly important in samples with one or multiple interfaces, like oxide, or isolating layers. When studying optical properties, laser beams can suffer multiple reflections in those interfaces and generate constructive or destructive interference, screening the real properties of the sample [44].

During the fabrication of a sample, the monolayer should be either transferred to the substrate or grown on it. In any case, monolayers can be damaged in the process, by developing cracks, or growing domain boundaries that open space for defect states. Also, monolayers can be submitted to stress resulting in wrinkles or bubbles which will produce a non-uniform strain distribution over the surface. This affects the phonons dynamics as well as the emission energies/intensities of the monolayer [45]. In Figure 5a we illustrate some of the main effects described before. Overall, these effects open space for studying different ways to control the properties of these materials and challenge the community in order to increase and improve the applications of 2D TMDs.

In recent years, the possibility of stacking different layered materials opened infinite

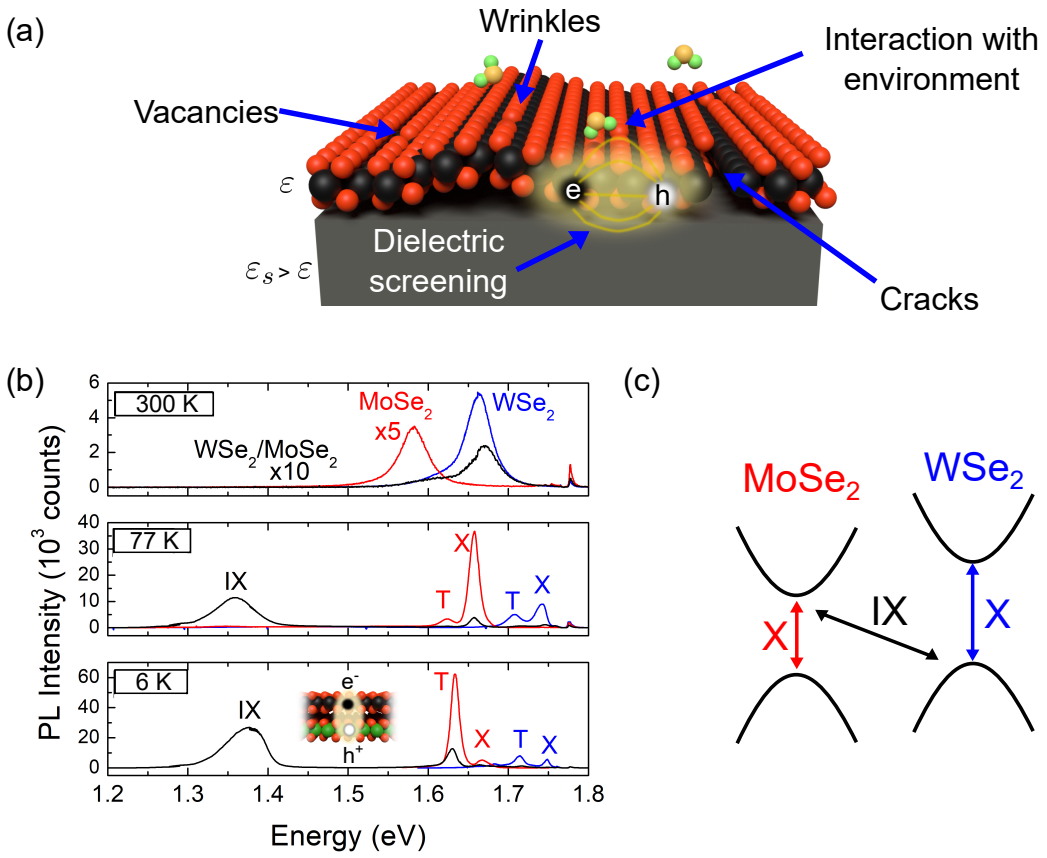

Figure 5 – (a) Illustration of some of the environmental effects discussed in the text: chalcogen vacancies, wrinkles of the monolayer, interaction with compounds present in the environment, cracks and dielectric screening. The representation includes an exciton with the electric flux lines in the exciton being modified due to the presence of a substrate with a dielectric constant ε_s larger than the constant ε of the TMD. (b) Photoluminescence spectra of a $WSe_2/MoSe_2$ heterostructure. The three panels show the spectra of the individual layers (in red and blue) and in the heterostructure (black) at room temperature, 77 K, and 6 K. The main emission peaks are labeled: exciton X, trion T, and interlayer exciton IX. (c) Band offset of the heterostructure representing the main transitions. PL measurements were performed by the author.

possibilities of combinations and physics due to proximity effects. In particular, in the case of semiconductors, it was observed that by stacking two monolayers of different TMDs, a new photoluminescence emission peak emerged. In these heterojunctions, when optically exciting the sample, one of the excited carriers can remain in one layer while the other migrates to the other layer and bind together in the so-called interlayer exciton. In Figure 5b we observe the photoluminescence of a heterostructure of $WSe_2/MoSe_2$ at different temperatures. We observe that at room temperature the only visible peaks are the individual emissions from the excitons of each layer. However, when lowering the temperature, a low energy peak starts to emerge and dominates the emissions of the sample. This can be more clearly understood from the band structure configuration (Figure 5c)

where the interlayer exciton is represented.

In addition to this effect, the different lattice constants of the two layers and a twist angle between them results in a (moiré) super lattice exhibiting new physical properties such as superconductivity. However, as these topics fall out of the scope of this thesis, for a detailed description of these phenomena we refer the reader to additional references [46–48].

1.4 Charge, spin and valley dynamics in TMDs

Here, we will provide a brief introduction to some of the main processes that occur under non-equilibrium conditions, from the excitation to recombination of charges/spins as well as some of the challenges for their determination. The spin state configuration of the initial and final states is of central importance in this process, as selection rules and the usual quantum mechanical restrictions dominate the transitions.

As described before, optical selection rules allow the excitation of an electron in a spin state $|\uparrow\rangle$ ($|\downarrow\rangle$) when exciting with circularly polarized σ_+ (σ_-) light. This means that in the case of linearly polarized light excitation, which can be expressed as a linear combination of both circular polarizations, both spin states will be equally excited. Experimental results have shown that the process of excitation of the electron until it binds and forms an exciton, is around 30 fs for monolayer MoS_2 [49], with similar ultrafast, sub-picosecond, formation times for WSe_2 and WS_2 [50,51]. For the case of trion formation, longer times have been observed as it requires first the formation of the exciton and then the binding with an extra carrier, which overall has a smaller binding energy when compared to the exciton. In that case, experimental works observed trion formation times of around 2 to 5 ps in $MoSe_2$ and MoS_2 respectively [52, 53].

After excitons and trions are generated, the recombination path will depend on various factors, such as whether the material is bright or dark, environmental and proximity effects and the quality of the sample. In addition to these variables, the experimental technique used to measure these processes introduces an additional challenge to the understanding of the charge/spin dynamics in TMDs. As a result of the combination of the aforementioned variables, there can be significant discrepancies in the literature when comparing specific lifetime processes in TMDs. However, the different reports provide ranges of characteristic times when the processes can take place as well as statistics for shining light on this matter.

The radiative recombination of excitons, for instance, has been reported to have lifetimes ranging from a few to hundreds of picoseconds at low temperatures before they recombine radiatively. Meanwhile, trions have lifetimes that can vary from tens to hundreds of picoseconds, depending on the case. For their recombination, trions first dissociate

their extra carrier which can result in a recoil effect that reduces the energy of the peak generating in this way a long-tailed emission to the low energy side [54].

The above-mentioned lifetimes will depend on variables such as temperature, excitation power, and energy. At low temperatures, the low density of phonons and thermal effects will enhance the lifetimes of radiative recombination processes by up to two orders of magnitude. In the case of the excitation power, high values can result in a high density of photoexcited charges generating many-body effects such as the formation of biexcitons, increase the rate of exciton-exciton annihilation, Auger scattering, and even a Mott transition to an electron-hole plasma [55]. Therefore, to reduce this effect, it is recommended to work at low excitation regimes below 100 $\mu W/\mu m^2$ or for pulsed excitation, 15 $\mu J/cm^2$ [56]. For the case of the excitation energy dependence, which is commonly used in the context of time-resolved measurements for selecting the desired state to populate, for instance in resonance with the exciton, trion, below the bandgap, or at a much higher energy. In the last case, the excess of energy will result in the generation of non-radiative effects such as phonons, that will release the energy of the electron to relax to the bottom of the conduction band. The larger the excitation energy with respect to the bandgap, the more non-radiative phenomena will get involved in the relaxation.

Additional scattering processes present in the relaxation of TMDs can involve intra- or inter-valley scattering of carriers. The first one can involve a change of spin state (spin flip) that can turn a bright state into a dark one or vice-versa. These processes are expected to be short-lived as they do not require additional momentum and instead are usually phonon-assisted. On the other hand, the inter-valley scattering process can involve or not a change of spin state and is one mechanism of the system for decreasing a spin imbalance, for instance, when one valley was optically populated. In this case, the scattering times can change depending on if the conduction or the valence band is being considered. In the conduction band, very short lifetimes have been reported (few ps) and can include the assistance of an intermediate state at the Q point of the Brillouin zone [57, 58]. It is worth pointing out that in both, intra- and inter-valley scattering processes, phonon scattering is one of the main mechanisms that gives place to the transitions.

Finally, one of the processes expected to have an important role in the long decay time scale is resident carrier recombination. Most of the TMDs are naturally doped or their doping can be modified by adding doping elements or by applying electric fields via gate voltages. In these cases, resident carriers, whether localized or free, have been observed and associated as a long-lived process that can last up to the nanosecond time scales [58–60].

Additional information regarding experimental details can be found in section 2.5, where we explain the pump-probe technique, broadly used to study the dynamics of different systems, and also in chapters 4 and 5 where we will unveil the charge and spin

dynamics of monolayer TMDs under different conditions.

1.5 This thesis

In this thesis, we explore the effect of a semiconducting substrate and an external magnetic field on the natural properties of monolayer TMDs. In particular, we are interested in the study of the optical and excitonic properties of these materials and how their dynamics changed in two scenarios: the presence of GaAs substrates and the effect of strong magnetic fields on the spin dynamics. The thesis is organized as follows:

- **Chapter 2** presents the experimental techniques and concepts required for the subsequent chapters. Additional theoretical concepts will also be introduced to complement and connect this introduction chapter with the experimental techniques. In particular, we introduce optical techniques such as photoluminescence and Raman spectroscopy but also scanning probe microscopy techniques, such as atomic force microscopy and Kelvin probe force microscopy. Finally, we present the optical pump-probe techniques and how we use them for measuring the time-resolved dynamics in our samples, for instance for differential reflectivity and the magneto-optic Kerr effect.

- **Chapter 3** presents the study of the charge transfer between monolayers of MoS_2 with their GaAs substrates. By comparing the photoluminescence emission of a control sample (isolated monolayer) and the emission of monolayers on GaAs substrates with different doping levels we observe the change in the density of charges in the monolayer by tracking the trion peak. We also use scanning Kelvin probe microscopy to determine the work function and establish the band offset of the different samples. In this way, we model the charge transfer in the system and suggest a type-I band alignment, which explains the strong mitigation of the photoluminescence in the junctions.

- **Chapter 4** presents the time-resolved differential reflectivity as a tool to analyze the charge dynamics in the WSe_2/GaAs system. We compare the change dynamics of a monolayer on GaAs and an electrically isolated monolayer, which allows us to also establish a band offset of the junction. Furthermore, we study the dynamics of the sample at different excitation energies and temperatures to determine the role of processes such as phonons and resonances.

- **Chapter 5** shows how a magnetic field can control the light-induced spin accumulation in a monolayer of $MoSe_2$. We use the magneto-optic Kerr effect in a pump-probe setup to determine the dynamics of spins in the monolayer under different circularly

polarized light excitations. By applying strong out-of-plane magnetic fields, we observe how the spin dynamics change and how it is possible to control the optically generated spin accumulation. Our results are explained by a rate-equation model for determining the dominant processes in the dynamics and estimating the decay times.

- **Chapter 6** presents the general conclusions of the thesis and the perspectives that it opens up.

CHAPTER 2

Experimental Methods

In this chapter, we present the experimental techniques and methods used in this thesis as well as additional physical concepts that complement the previous chapter for a better understanding of each technique. We start by describing how monolayers of transition metal dichalcogenides (TMDs) are obtained and how to make samples to measure and understand their different optical properties. Then, we present additional optical and excitonic properties of these materials and how to measure them through photoluminescence and Raman spectroscopy. Moreover, we explain how to use surface scanning techniques to determine the topography of the samples, with atomic force microscopy, or electronic properties, as the work function, via scanning Kelvin probe microscopy. Furthermore, we present the experimental implementation of the optical pump-probe techniques discussed in chapter 1 and how they are used to measure time-resolved properties in TMDs, such as transient reflectivity. Finally, we introduce the magneto-optical Kerr effect and the experimental details for measuring time-resolved spin dynamics in TMDs.

2.1 Exfoliation of TMDs

There are different ways of obtaining single layers of transition metal dichalcogenides (TMDs), with mechanical exfoliation and chemical vapor deposition (CVD) being among the most commonly used techniques in the literature. CVD involves growing TMDs, with the desired thickness, in a solid substrate starting with chalcogen and transition metal individual reactants to interact in controlled conditions such as temperature and pressure [61]. This technique has the advantage of allowing the production of flakes significantly larger than other techniques. However, it comes with challenges such as the

control of defects or different crystal domains. On the other hand, mechanical exfoliation, originally used in graphene, takes advantage of the weak van der Waals interaction between layers to mechanically separate them down to the monolayer limit. Although monolayers obtained through this technique are smaller compared to CVD, it offers the advantage of minimizing impurities within the crystal. Additionally, the process is simple and eliminates the need for extensive or costly equipment.

In this thesis, we use mechanical exfoliation as it can provide monolayers large enough to characterize the properties of the material ($\sim$10 μm), reduce impurities, and fulfills the needs of our work. For obtaining a monolayer by mechanical exfoliation, one should take a piece of adhesive tape, place it over one small piece of crystal of the TMD, and slowly peel it back off. Two types of adhesive tape are commonly used for this purpose: Scotch tape and Nitto (blue) tape [62]. In particular, we used the latter as it generates fewer glue residues in the flakes that can interfere with the study of the optical properties of the monolayers. In order to improve the number and area of few-layer regions, the tape should be glued into itself and peeled back off to make a new exfoliation of the TMD. After repeating this process a few times, the exfoliated material can be transferred from the tape to the desired substrate. However, in the case of GaAs substrates, the optical contrast with the TMD single layers is significantly limited, requiring the adoption of the gel film transfer method for its enhanced convenience [63]. Furthermore, this technique provides more control for positioning the monolayer in specific areas in the substrate, for instance, a clean homogenous region in the substrate and allows to stack flakes of different materials. The process starts with the exfoliated material in the blue tape, which is transferred onto a piece of polydimethylsiloxane (PDMS) film (Figure 6a) and it is then mapped with an optical microscope to identify the single layers by optical contrast. When a potential single layer is identified, a fluorescence microscope is used to see the fluorescence of the flake, and thus, have certainty of having obtained a single layer (Figure 6b) [2].

Subsequently, the PDMS film, with the transferred flakes attached, is aligned with a previously cleaved and cleaned substrate and gently pressed against it (Figure 6c). Without separating them, the junction is heated to 80 °C for five minutes to enhance the transference of the monolayers (Figure 6d). The gel is then slowly peeled back to prevent the breaking of the transferred flakes (Figure 6e). Finally, the monolayers can be identified on the substrate, and their exact positions should be recorded for subsequent measurements (Figure 6f).

After identifying the flakes, it is convenient to observe their fluorescence again, to confirm the state of the monolayer, determining possible cracks or defects produced during the transfer. However, for the case of MoS_2 and WSe_2 on GaAs, monolayer fluorescence is highly quenched due to the interaction with the substrate. Therefore, in these cases, we use dark field (DF) imaging, which provides an image of the scattered light by any edge

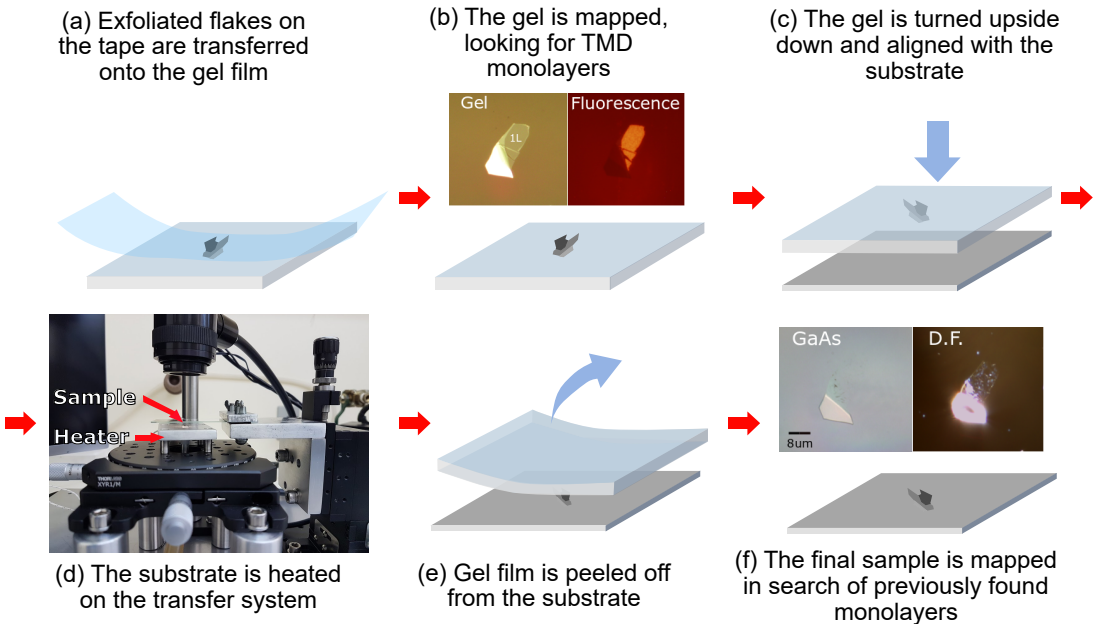

Figure 6 – Schematic illustration of the sample fabrication process. Insets: (b) optical images of a flake on the gel (b, left), its fluorescence (b, right); (f) after transferred on GaAs as viewed by bright field (left), and dark field (right).

or defect on the surface.

2.2 Raman Spectroscopy

Raman spectroscopy is a powerful optical characterization technique that allows us to study the vibrational modes of a given material. When the light interacts with a crystal lattice or molecule, the electric field affects the charge distribution inducing dipoles or changes in the polarizability. The interaction between light and matter gives rise to oscillation modes (phonons) on the lattice, which in turn scatter light in various ways. These light-matter interactions can be classified based on whether they can be detected using Raman spectroscopy or not. If the associated polarizability changes due to the coupling with the electric field, the mode will be called Raman active and otherwise, an inactive one.

Experimentally, a laser beam excites a crystal lattice or molecule, driving it up to a virtual state for its subsequent relaxation in one of three possible paths. First, the system can return to the same initial state, by scattering photons with the same energy as the incoming beam (Rayleigh/elastic scattering). Second, the sample can absorb energy from the light reducing the energy of the scattered photons with respect to the incoming ones (Stokes scattering). Third, the system can lose energy in the interaction, resulting in the scattering of photons with an energy higher than the energy of the incoming beam

(anti-Stokes scattering). Figure 7a illustrates a Raman spectrum with the three possible scattering processes. After measured, the spectrum is usually presented as a difference between the wavenumber of the excitation beam and the scattered light:

$$R_s = \left(\frac{1}{\lambda_{exc}} - \frac{1}{\lambda}\right), \tag{2.1}$$

with R_s defined as the Raman shift in cm^{-1}, λ_{exc} is the wavelength of the excitation beam and λ is the wavelength of the scattered light.

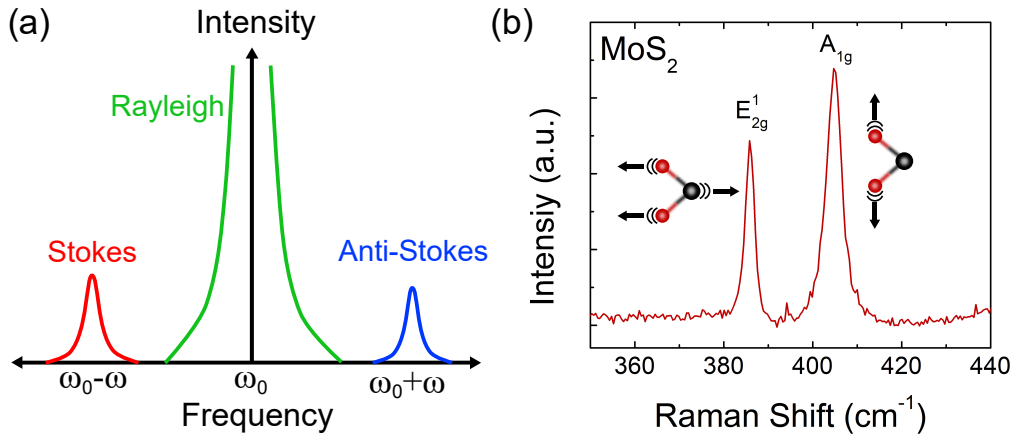

Figure 7 – (a) Illustration of the three types of scattering processes studied in Raman spectroscopy. (b) Characteristic Raman spectra of a monolayer MoS_2 showing the two strongest vibrational modes. Illustrations of the modes are presented close to their respective peaks.

Transition metal dichalcogenides exhibit different Raman modes in both monolayer and bulk forms. Among them, two modes have garnered significant interest for characterizing the thickness of flakes: E^1_{2g} (in-plane oscillation) and A_{1g} (out-of-plane oscillation). The reduction of the number of layers reduces the van der Waals interaction of the crystal generating a change in the frequency of the vibrations due to the weaker restoring forces acting on the atoms. As a result, the above-mentioned Raman modes will suffer an energy shift towards lower frequency oscillations. This phenomenon is particularly intense in the case of the out-of-plane oscillation mode as its interaction is strongly dependent on its neighbor layers. On the other hand, in-plane mode E^1_{2g} is strikingly observed to shift towards higher oscillation frequencies, which has been associated with long-distance Coulomb interactions. For MoS_2 and WS_2 flakes this effect is particularly intense, as well-resolved E^1_{2g} and A_{1g} Raman peaks start to approach each other while reducing the number of layers [64–66]. For MoS_2 the characteristic difference between these modes is as small as 19 cm^{-1}, while for WS_2 this value is observed to be 61 cm^{-1}. Figure 7b shows a

typical Raman spectrum of a monolayer of MoS_2 exhibing intense, narrow, E^1_{2g} and A_{1g} peaks.

A typical experimental setup for Raman spectroscopy consists of a light exciting source (laser), a diffraction grating/monochromator and a sensor. The photons emitted or scattered by the sample arrive at the diffraction grating which separates them by their wavelength and also determines the range of the spectrum that will be analyzed. The photons scattered by the grating are detected by a sensor (CCD) which transforms the light into electrical signals that are converted by software into a spectrum.

	Raman mode (cm^{-1})	
TMD	E^1_{2g}	A_{1g}
WS_2	357	418
MoS_2	384	404
WSe_2	-	249
$MoSe_2$	286	239

Table 1 – Experimental values of the two main active Raman modes in TMD monolayers [67].

For our measurements, we used a WITec [68] *alpha 300A* experimental setup available in the LCPNano facilities at UFMG. The samples were excited with a 532 nm wavelength laser with a power of 0.3 mW [1] and focused on the sample with a 100x objective. Table 1 presents the position, at room temperature, of the two main active Raman modes in different monolayer semiconducting TMDs.

2.3 Photoluminescence

Photoluminescence spectroscopy allows us to study the light emitted by a sample due to electronic transitions. This technique involves optically exciting a sample using a laser beam, with an energy larger than the energy of the bandgap of the material, to promote electrons from the valence band to an excited state in the conduction band. In this process, the absence of the electron in the valence band is understood as an effective positive charge (hole) that will bind to the excited electron due to electrostatic interaction. Therefore, the excited electron (and hole) start to lose energy to the system, relaxing non-radiatively to the bottom (top) of the conduction (valence) band. Afterwards, the electron and hole recombine emitting light with an energy lower than the laser beam. Figure 8a illustrates this process for a graphical visualization.

[1] Warning: a high laser power can damage the single layers. This power is enough to see weak emissions without damages. Nevertheless, a short exposition time (a few seconds or less) is recommended.

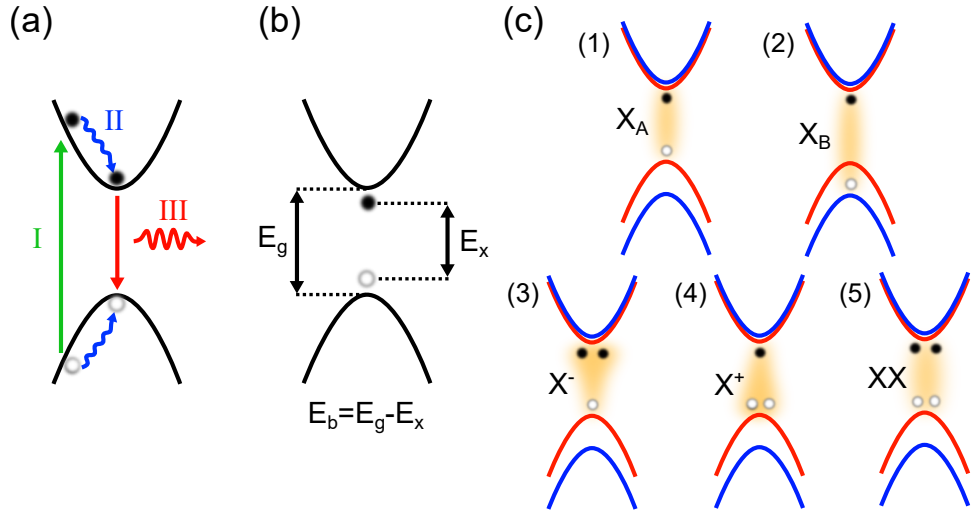

Figure 8 – (a) Schematics of photoluminescence steps: first, the optical excitation of an electron in the valence band (I); therefore, relaxation of the electron (hole) to the bottom (top) of the conduction (valence) band (II); finally, electron and hole recombine emitting a photon with the characteristic energy of the material (III). (b) Representation of the bandgap energy E_g, exciton energy E_x, and its relation with the exciton binding energy E_b. (c) Representation of the main excitonic states observed in TMDs: (1) the A-exciton X_A, (2) B-exciton X_B, (3) negatively charged exciton (trion) X^-, (4) positively charged exciton (trion) X^+, and the (5) bi-exciton XX.

In semiconductors, when the excited electron and hole relax, before recombining, they bound together due to Coulomb interaction forming the so-called exciton. They receive this name as they present electron-hole joint properties different than the ones of the individual carrier compounds. For this reason, this bound state is also known as a quasiparticle, exhibiting, for instance, its own dynamics, moving as a single entity transporting charge and momentum. In the TMD study field, they play a central role, especially in monolayers. Their direct bandgap structure as well as their in-plane confinement makes the electron-hole Coulomb interaction unusually strong when compared with traditional semiconductors. As a result, when the exciton decays (electron-hole recombination) the energy of the emitted photon E_x is lower than the bandgap energy E_g. In Figure 8b we can observe these two energies and shows how their difference relates to the exciton binding energy E_b.

In addition to excitons, the strong electrostatic interaction in monolayer TMDs also allows the formation of more complex systems. Figure 8c present the main quasiparticles that take place in these materials and can be detected in photoluminescence spectroscopy. Due to the large spin splitting in the $K_\pm$ points, two types of excitons can emerge depending on their spin state. They are the A-exciton Figure 8c.1 and the B-exciton Figure 8c.2 with a larger emission energy. Moreover, in samples with a high density of charges, excitons

have the capability to bind with an additional carrier, resulting in the formation of a charged exciton known as a trion. The trion can either be negatively charged (8c.3) or positively charged (8c.4), depending on the dominant charge carriers in the system. Finally, in conditions with an even higher density of charges and low thermal effects, two excitons can bind together to form the four-carrier quasiparticle called biexciton (8c.5)

Experimentally, the main elements for performing photoluminescence (PL) spectroscopy are the same as mentioned for Raman spectroscopy: an excitation source (laser beam), with an energy larger than the energy of the bandgap of the material and a spectrometer for collecting and diffracting the emitted light for further analysis. The difference between the two techniques is the origin of the process: scattered light in the first case, and emitted light in the second one. In this work, two setups were used to measure PL, one for room temperature measurements in chapter 3, and another for low-temperature and high magnetic fields PL in chapter 5. In the first case, we used the same commercial *WiTec alpha 300A* system as for Raman measurements, with a diffraction grating of 600 l/mm for the acquisition of broad-range spectra and a 100x objective to reduce the spot size and improve the control and precision of the spot in the sample to excite. For high magnetic fields measurements, we assembled the experimental setup presented in Figure 9, which we will proceed to describe.

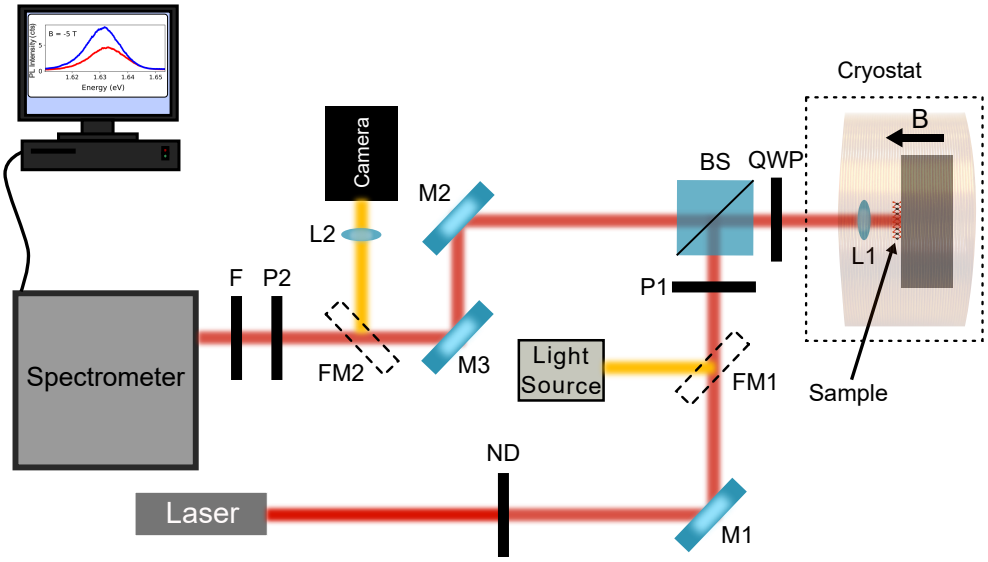

Figure 9 – Diagram of the experimental setup used for measuring photoluminescence spectroscopy at low-temperatures and high magnetic fields.

For excitation, we used a laser diode of 690 nm (1.797 eV) in a Thorlabs temperature-controlled laser diode mount LDM9T/9. By using this wavelength, we can excite the sample above, but close to the bandgap of the $MoSe_2$ reducing non-radiative processes. Also, we use a low excitation power (100 μW) to reduce the photodoping and many-body effects. Since the laser beam emerges from the mount with high divergence, we employed a

combination of converging lenses and a pinhole (not shown in the diagram) to collimate an shape the beam. This collimation process resulted in a beam diameter of approximately 4 mm. We set the laser power with a neutral density filter (ND) before the beam is directed to the sample by a mirror (M1) and a beamsplitter (BS). To focus the light on the sample we use a cold lens (Thorlabs C230TMD-B) which sits inside the cryostate. The sample is placed in a chip carrier and positioned with an attocube piezostack for x, y, and z movements. The flake is identified by illuminating it with a white light source directed towards the sample using a flip mirror (FM1). The reflected light is then redirected to a camera using a second flip mirror (FM2). For the control of the polarization in the excitation and detection, the ideal is to circularly polarize the excitation and detection beams. One common way to do this is as follows:

1. Linearly polarize the excitation beam with a polarizer (P1).
2. Align a quarter-wave plate (QWP) at 45° respect to $P1$ axis to generate circularly polarized light excitation.
3. The light emitted by the sample will pass again through the QWP but, due to the change in the direction of propagation, the effective angle of the QWP will suffer a mirror effect. When passing by the QWP the circularly polarized light will transform to linearly polarized, for instance vertical or horizontal, depending on the polarization (right or left circularly polarized).
4. Finally, a polarizer (P2), also called an analyzer, in the angle of interest is placed before the spectrometer for the detection of circularly polarized light. A filter (F) is placed in front of the spectrometer to prevent any scattered laser light to enter.

For performing this procedure, it is necessary to precisely set the angles of the QWP, set the polarization of excitation, and the analyzer P2, for the detection, at each measurement. This can be particularly challenging when working with manual rotating mounts (our case) to select the angle of the polarizer, where the precision can be limited. This can result in an increase in the spurious effects in the measurements. Moreover, the rotating mounts, such as the one used for the QWP, commonly contain magnetic-field sensitive components that make the handling of the piece challenging when working at high magnetic fields in the cryostat. Hence, to reduce these unwanted effects we performed the following alternative procedure:

1. We linearly polarized (vertically) our excitation beam with P1.
2. We aligned the fast axis of the QWP with the polarization of P1. This implies that the QWP will not change the polarization of the beam and we excite our sample

with linearly polarized light. In the case of zero magnetic field, this will excite both valleys and the energy degeneracy will result in the emitted light being also linearly polarized. However, in the case of non-zero magnetic field, breaking the valley energy degeneracy will result in a dominant circular polarization at a certain energy. When the emitted circular polarized light passes through the QWP, it is transformed into linearly polarized at +45° and -45°, with respect to the fast axis of the QWP, depending on the type of circular polarization.

3. Finally, by aligning the analyzer P2 at the mentioned angles, we select the polarization of the light that we want to measure.

By using this procedure, we reduce the number of optical components to be adjusted between measurements to just one (the analyzer) increasing the speed of the measurements and reducing the chances of introducing spurious effects. Additionally, as we excite the sample with linearly polarized light, we obtain a strong signal for emitted light of both emitted polarizations, contrary to the case of, for instance, exciting the sample in a single circular polarization and detecting the two emitted polarizations with the analyzer.

The photoluminescence measurements in chapter 5 were performed at low temperatures to reduce thermal effects and each spectrum was acquired three times with a 20-second collection time each, for further average and noise reduction.

2.4 Scanning probe microscopy

Scanning probe microscopy (SPM) is a family of techniques that allows the visualization and characterization of the surface of the materials on the micro and nanoscopic scale. SPM is characterized by the use of a probe, *e.g.* a tip, that scans the surface of the sample measuring the physical property of interest. Among the most used techniques, we can mention atomic force microscopy (AFM), scanning Kelvin probe microscopy (SKPM), scanning tunneling microscopy, magnetic force microscopy, among others. Here, we use AFM and SKPM due to their convenience for characterizing the topography and electronic properties of our samples.

2.4.1 Atomic force microscopy

Atomic force microscopy (AFM) is among the most used SPM techniques and focuses on the determination of the topography of a given sample in up to a nanometric resolution. For this purpose, the technique uses a cantilever with a pointy tip that will act as the probe of the system. In the non-contact mode, used in our work, the probe will scan a selected region of the sample while oscillating at a given frequency with intermittent

contact with the surface of the specimen. Simultaneously, a laser is directed towards the back end of the tip, and a photodiode registers the reflection. When the tip interacts with the surface of the sample, such as at edges or higher regions, the natural oscillation frequency is altered, causing a change in the amplitude of oscillation of the reflected laser beam (see Figure 10a). By detecting these changes, it becomes possible to establish a surface profile of the sample.

In our experiments, we used a Bruker Multimode 8 with a Nanoscope V controller, at normal atmospheric pressure and room temperature.

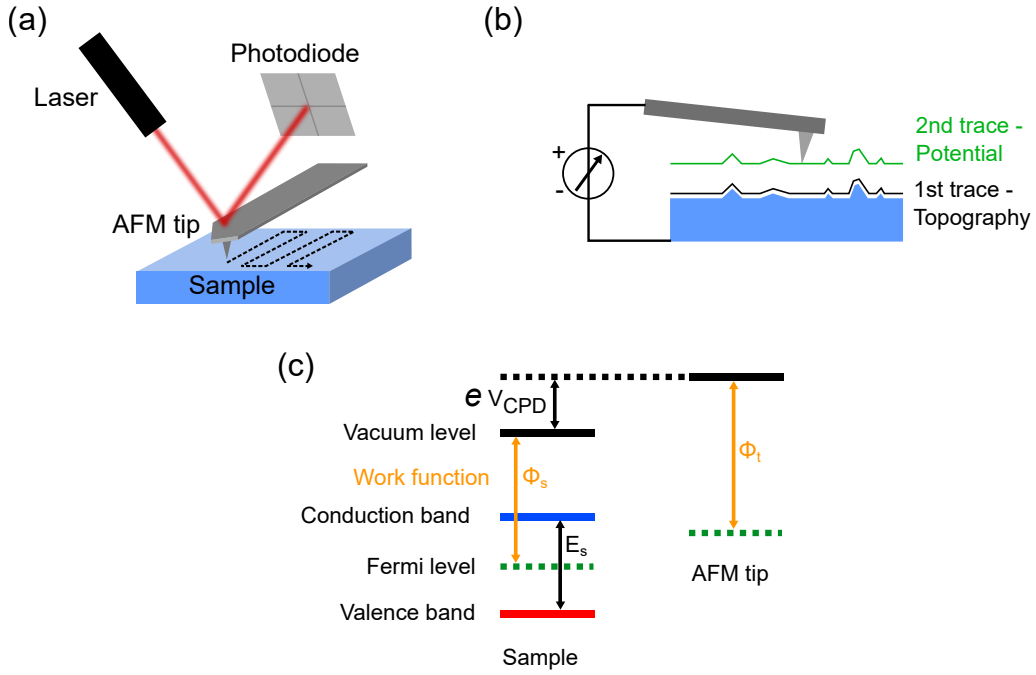

Figure 10 – (a)Illustration of the AFM experimental setup configuration. (b) Representation of an SKPM measurement procedure. (c) Band structure and main energy relations between different states.

2.4.2 Scanning Kelvin probe microscopy

Scanning Kelvin probe microscopy (SKPM) also called Kelvin probe force microscopy (KPFM) is one type of atomic force microscopy that measures the contact potential difference (CPD) between a sample and the AFM tip. This physical quantity is directly related to the work function of the sample, which relates the energy difference between the Fermi level of the sample and the vacuum level.

The SKPM technique begins with a conventional AFM scan with a conducting tip to obtain the topographic profile of the surface. Then, the tip retraces the same area using the acquired profile as a reference, maintaining a constant distance of a few nanometers from the surface while applying a constant bias voltage between the tip and the sample (see

Figure 10b). In this configuration, the sample surface and the probe act as parallel plates of a capacitor. In order to facilitate detection, the cantilever is modulated either in frequency (FM) or in amplitude (AM) of oscillation, resulting in a change in the capacitance of the probe-sample system [69]. This change in capacitance leads to a corresponding alteration in the force between the tip and the surface. Variations in the texture or materials of the sample affect this force, which is then detected as changes in the deflection of the laser beam that is directed back to the photodetector.

The contact potential difference V_{CPD} between the probe tip and the surface, can be related to the work function of the material as

$$V_{CPD} = \frac{\phi_s - \phi_t}{e}, \tag{2.2}$$

with $\phi_{t(s)}$ the work function of the tip (sample) and e the electron charge.

Additional details on the SKPM theory can be consulted in [70, 71].

2.5 Pump-probe technique

Electronic and phononic processes in semiconductors are characterized by dynamics that take place within the femto- to nanosecond time scales. Before the invention of ultrashort (fs) pulsed lasers, accessing and studying these processes posed significant challenges. The main difficulty stemmed from the requirement of a system capable of exciting the sample with timescales shorter than the studied phenomenon lifetime. Additionally, detection systems with high velocities were necessary to surpass the speed of the phenomenon itself. In the pump-probe technique, pulsed lasers are combined with high detectivity and signal processing systems to unveil the different relaxation processes involved in a sample. Nowadays, this technique has become one of the most widely employed optical tools for studying the dynamics and temporal evolution of various systems. Its applications span across diverse fields, ranging from quantum optics to life science [72, 73].

In a pump-probe technique, two pulsed laser beams are necessary: one that excites the sample out of equilibrium (pump), and a second pulse beam that measures the state of the system (probe). Also, a delay device is employed to control the time delay between the pump and probe pulses, allowing for precise temporal resolution. It can be, for instance, a motorized linear stage with a couple of mirrors that changes the optical path of one of the beams with respect to the other. The signal from the probe pulse is then detected, and therefore, signal amplification and processing techniques are applied to enhance the measured response and extract valuable information about the dynamics and relaxation processes in the sample.

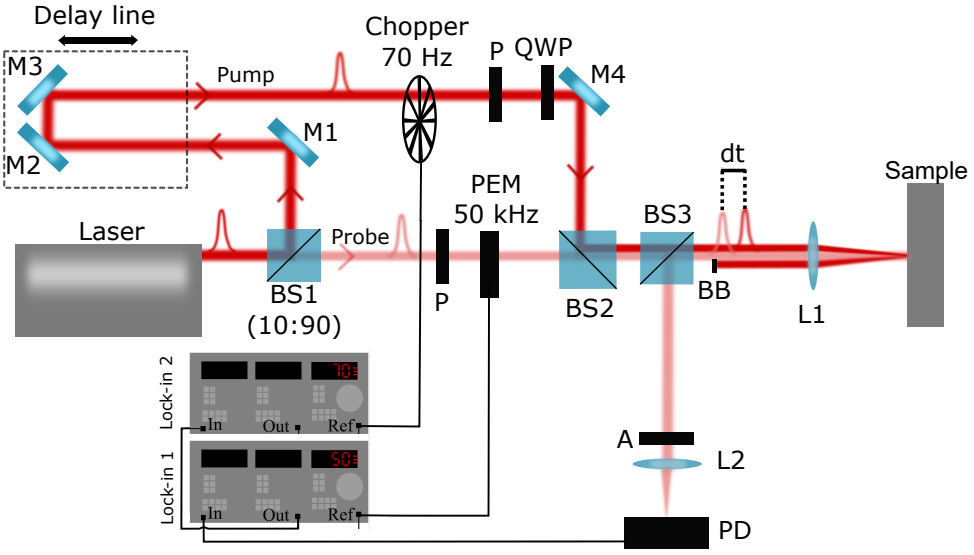

Figure 11 – Representation of the main elements in a pump-probe experimental setup.

Figure 11 presents the main elements involved in our pump-probe experimental setup. First, a Titanium-sapphire pulsed-laser with a nominal pulsewidth of 50 fs and a repetition rate of 80 MHz is used as the excitation source. Using a beamsplitter (BS1 10:90), the incident beam is split into two with the pump beam having a higher power intensity than the probe beam. The reason for this is that the pump beam is expected to perturb the system and drive it out of equilibrium. In contrast, the probe beam is used solely for measurement purposes to determine the current state of the system without introducing any additional excitations.

In the pump beam, a delay line allows to change the optical path and control the delay time between the pump and probe beams. Afterwards, a signal modulator, as a chopper or a photoelastic modulator (PEM), can be introduced to enhance the signal detection. Also, additional elements such as polarizers or wave-plate retarders can be added to manipulate the polarization of the beam to excite the sample tailored to the interest of the measurement. A beamsplitter (BS2) joins the path of the pump and probe beams which are aligned parallel, and very close, in the direction of a lens (L1) which focuses the beams on the sample. When reflected, the pump beam is blocked by a beam blocker (BB) to enhance the signal detection of the probe.

In the probe beam path, after BS1, polarizers and modulators are also commonly used to control and later detect the beam. When reflected from the sample, the probe is oriented by using a beamsplitter (BS3) and focused by a lens (L2) into a photodetector. For polarization analysis, we use a polarizer (A) before the detection, to select specific information from the sample. Most of the studied phenomena in ultrafast optics are weak in intensity, therefore, it is necessary to amplify and filter the signal to minimize noise

originating from the environment. For this purpose, one or both laser beams should be modulated in frequency as mentioned before. The modulators are connected to lock-in amplifiers, electronic devices, that receive the reference frequency of the modulator as well as the detected signal to compare them, filter, and amplify the signal of interest.

2.5.1 Cryogenic measurements

In our work, we are interested in low-temperature and high magnetic field pump-probe measurements. For that purpose, we used a *Cryovac* helium bath cryostat with a 7 T superconducting split coil magnet and a variable temperature insert (VTI). Figure 12a shows a schematics of the cryostat, in a profile view, presenting the main chambers: the sample space in the core, the liquid Helium (LHe) and liquid nitrogen (LN) chambers, all spaced by vacuum. The split-coil superconducting magnet is located in the LHe space, while the sample is placed in the middle of the magnet, in the core chamber.

In the figure, it is also presented an inset with the region of the sample, showing the three-axis attocube piezo-stage, used to precisely control the position of the sample and the spot of interest in the flakes. Also, the figure indicates the lens, a C230TMD-B from Thorlabs, with an effective diameter of 5.5 mm, used to focus the laser beams into the sample. This short diameter, as well as the short visual field close to it, resulted in additional challenges in guaranteeing the quality and fidelity of the measurements. In this regard, we introduced a confocal-like configuration to enhance the blocking of the pump beam.

Figure 12b presents our experimental setup for pump-probe measurements at low temperatures and high magnetic fields. For the filtering of the pump, we first introduced the lens L1 which changes the focal point of the beam and results in a larger spot size on the sample. When the pump and probe beam are reflected from the sample, they pass through the lenses L3 and L4, with the same focal length (f) and spaced by $2f$. Due to the introduction of L1, the pump and the probe will focus on different spots. As both beams are spatially separated, it just rests to find the focal point of the pump and place the beam blocker (BB). It is worth noting that the use of the BB proved to be the best option after attempting to filter the pump with pinholes or using an iris. The latter two options, in addition to blocking the pump, significantly reduced the probe signal, resulting in increased noise. On the other hand, by using the BB, we can specifically block the side of the probe where there is overlap with the pump.

We used a double modulation configuration, with a chopper at 70 Hz at the pump beam, and a photoelastic modulator (PEM) at 50 kHz at the probe beam. In this configuration, the signal of the photodetector is sent to a first lock-in, which is referenced to the PEM, allowing filter and amplify the signal coming from the probe. Thereafter,

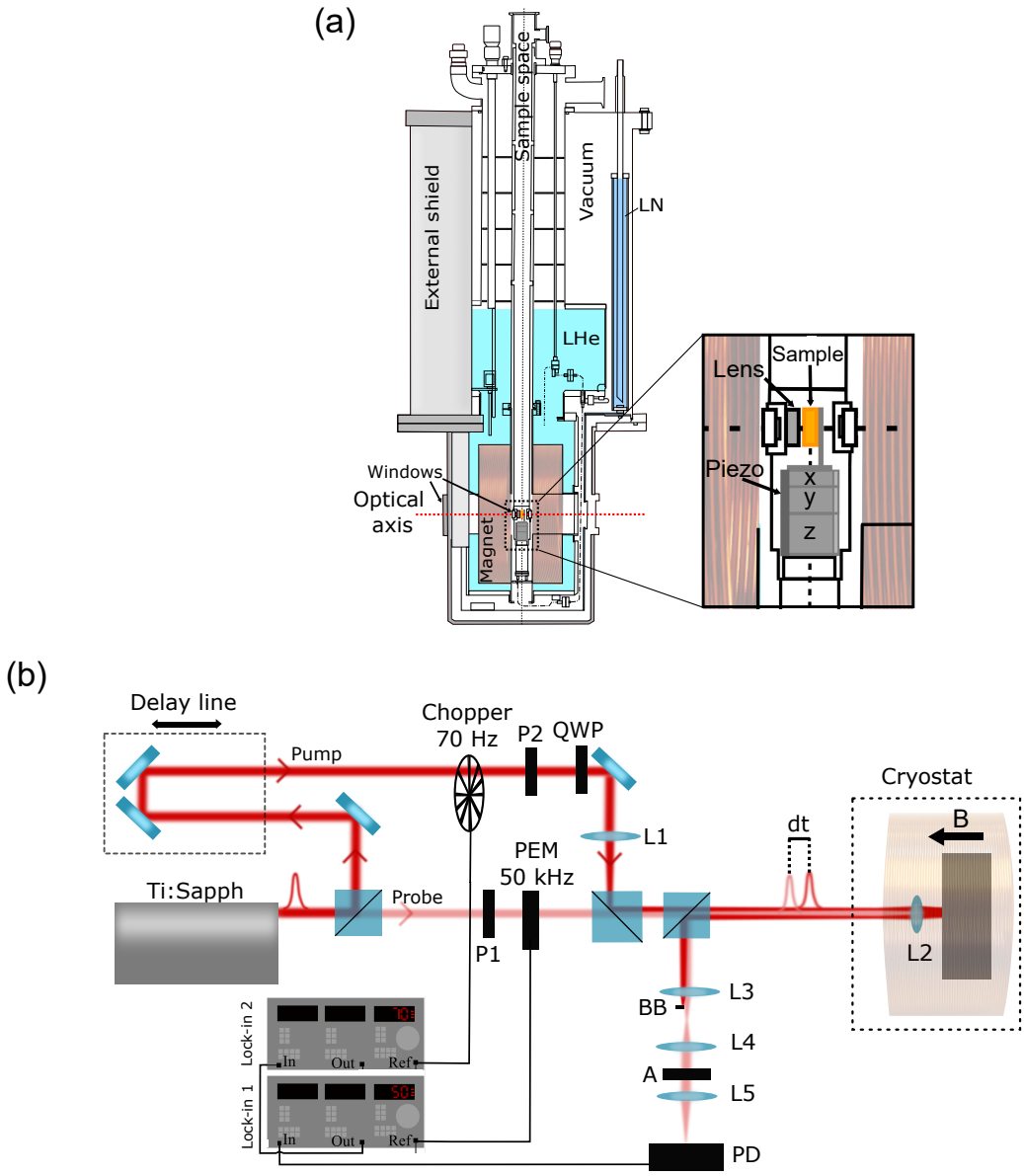

Figure 12 – (a) Illustration of the cryostat with a VTI used in our experiments. (b) Experimental setup used in the time-resolved measurements.

the output signal from the first lock-in is sent to a second lock-in amplifier which has the chopper as its reference. In this way, it is possible to enhance the amplification and filtering of the probe beam signal which is modulated by the pump beam.

2.6 Magneto-optical Kerr effect

Among the spin-related properties in TMDs, this thesis is focused on the characterization and control of the spin population and its dynamics in monolayer TMDs. One of the most used techniques for this purpose is the magneto-optic Kerr effect (MOKE). Despite that this technique is conceived for the measurement of magnetization in materials, it can

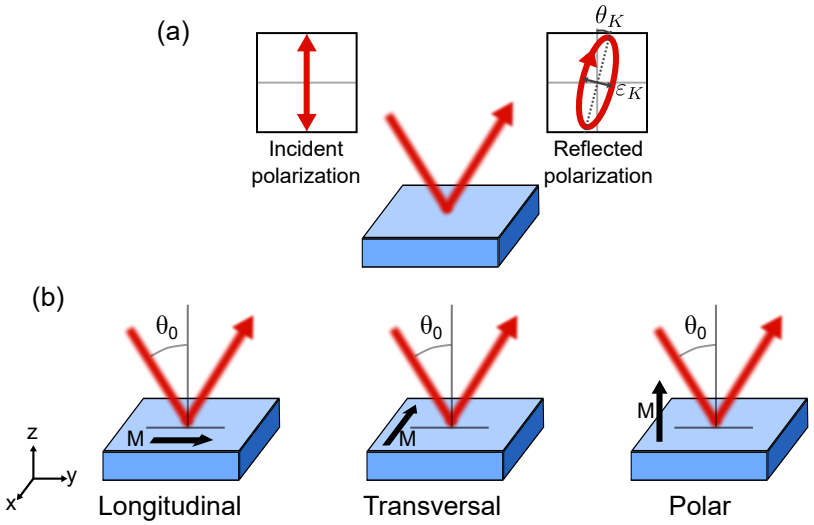

Figure 13 – (a)Representation of the magneto-optical Kerr effect. (b) Geometries of the three types of Kerr effect: longitudinal, transversal, and polar.

also be used in semiconducting TMDs which do not possess an intrinsic magnetization. As discussed in section 1.1, the optical selection rules allow to excite one spin population using circularly polarized light. While excited, this optically-induced spin imbalance in the material can be seen as a transient magnetization of the region in the monolayer that can now be measured using magneto-optic Kerr effect.

In MOKE, a linearly polarized light beam interacts with a sample and when reflected, this interaction will change the polarization of the beam (see Figure 13a). To formally describe this process, we should start considering the dielectric tensor $\boldsymbol{\epsilon}$ of a given material, which models the interaction between the material medium and the electromagnetic radiation via $\vec{D} = \boldsymbol{\epsilon}\vec{E}$, where

$$\boldsymbol{\epsilon} = \begin{pmatrix} \tilde{\epsilon}_{xx} & \tilde{\epsilon}_{xy} & \tilde{\epsilon}_{xz} \\ \tilde{\epsilon}_{yx} & \tilde{\epsilon}_{yy} & \tilde{\epsilon}_{yz} \\ \tilde{\epsilon}_{zx} & \tilde{\epsilon}_{zy} & \tilde{\epsilon}_{zz} \end{pmatrix}, \tag{2.3}$$

$\vec{D}$ is the electric displacement, $\vec{E}$ is the electric field, and each tensor element $\tilde{\epsilon}_{ij}$ is complex. In the classic description of MOKE, the magnetization of a sample can be considered to be in one of three configurations: longitudinal, transversal, and polar (see Figure 13b). In the longitudinal case, the magnetization lies on the plane of the sample but in the plane of incidence of the light beam, while in transversal it is perpendicular to the plane of incidence. In polar MOKE the magnetization points out of the plane of the sample and the light beam is usually aligned perpendicular to the surface of the sample (parallel to the magnetization).

In monolayer TMDs, the spin accumulation induces a polar-like transient magneti-

zation that simplifies the $z-$components of the dielectric tensor. Furthermore, due to the inherent symmetry of monolayer TMDs, equation 2.3 can be written as

$$\boldsymbol{\epsilon} = \begin{pmatrix} \tilde{\epsilon}_{xx} & \tilde{\epsilon}_{xy} & 0 \\ -\tilde{\epsilon}_{xy} & \tilde{\epsilon}_{xx} & 0 \\ 0 & 0 & \tilde{\epsilon}_{zz} \end{pmatrix}. \tag{2.4}$$

Determining the two in-plane eigenvectors, we find:

$$\vec{E}_{\pm} = \begin{pmatrix} E_x \\ E_y \end{pmatrix}_{\pm} = \frac{1}{\sqrt{2}} \begin{pmatrix} 1 \\ \pm i \end{pmatrix}, \tag{2.5}$$

which are the Jones vector representations for left and right circularly polarized light (σ_+ and σ_-). Also, the respective eigenvalues are determined to be $\lambda_{\pm} = \tilde{\epsilon}_{xx} \pm i\tilde{\epsilon}_{xy}$. This meaningful result, indicating the circular polarization of light as the basis of propagation, is the core for the following analysis.

It is now convenient to diagonalize $\boldsymbol{\epsilon}$ to simplify our analysis. Calculating, we obtain

$$\boldsymbol{\epsilon} = \begin{pmatrix} \tilde{\epsilon}_{xx} + i\tilde{\epsilon}_{xy} & 0 & 0 \\ 0 & \tilde{\epsilon}_{xx} - i\tilde{\epsilon}_{xy} & 0 \\ 0 & 0 & \tilde{\epsilon}_{zz} \end{pmatrix}. \tag{2.6}$$

That can be easily compared to the complex refractive index of the medium through the relation $\boldsymbol{\epsilon} = \tilde{\boldsymbol{n}}^2$. Therefore, we can define the refractive indexes for left $\tilde{n}_+^2$ and right $\tilde{n}_-^2$ circularly polarized light as:

$$\tilde{n}_+^2 = \tilde{\epsilon}_{xx} + i\tilde{\epsilon}_{xy}, \tag{2.7}$$

$$\tilde{n}_-^2 = \tilde{\epsilon}_{xx} - i\tilde{\epsilon}_{xy}. \tag{2.8}$$

Now that we have a description of the response of the medium to light, we can consider a light beam and describe how it changes after the interaction with the material. If we consider an incident, linearly polarized beam in the x-direction, in Jones vector representation we can write it as a linear combination of circular polarization as ($\vec{E}_{\pm}$ for the e-field from $\sigma_{\pm}$ polarized light):

$$\vec{E}_x = \frac{1}{\sqrt{2}}(\vec{E}_+ + \vec{E}_-). \tag{2.9}$$

To describe how the beam changes, we should apply Fresnel analysis which defines the reflection coefficients for left ($\tilde{r}_+$) and right circularly polarized light ($\tilde{r}_-$) in a spherical basis as:

$$\tilde{r}_+ = r_+ e^{i\phi_+}, \tag{2.10}$$

$$\tilde{r}_- = r_- e^{i\phi_-}, \tag{2.11}$$

where $r_\pm$ the amplitude and $\phi_\pm$ the phase of the circularly polarized light after being reflected. Hence, we can define the Kerr rotation θ_K and ellipticity ε_K by [74, 75]:

$$\theta_K = \frac{1}{2}(\phi_+ - \phi_-), \tag{2.12}$$

$$\varepsilon_K = \frac{r_+ - r_-}{r_+ + r_-}, \tag{2.13}$$

which describes the rotation of the polarization as the relative change in the phase of the two circular polarization states, while the Kerr ellipticity is characterized by a relative change in the amplitude. Under this formalism, we can now define the Fresnel reflection coefficient for a linearly polarized beam propagating in the z-direction as

$$\tilde{r} = \frac{1 - \tilde{n}}{1 + \tilde{n}}. \tag{2.14}$$

Combining this relation with the reflection coefficients in the circularly polarized basis in equations 2.10 and 2.11 and equations 2.7 and 2.8, we can obtain the expression for the magneto-optic Kerr effect complex phase

$$\Phi = \theta_K + i\varepsilon_K = -\frac{\tilde{\epsilon}_{xy}}{\sqrt{\tilde{\epsilon}_{xx}(\tilde{\epsilon}_{xx} - 1)}}, \tag{2.15}$$

where we have used the deffinitions in equations 2.12, 2.13, and it has been considered $|\tilde{\epsilon}_{xy}| \ll |\tilde{\epsilon}_{xx}|$ and small rotation angles θ_K. From here, we can observe that if $\tilde{\epsilon}_{xy} = 0$, in an isotropic media, then $\theta_K = 0 = \varepsilon_K$.

2.6.1 Time-resolved MOKE

For measuring time-resolved MOKE, we use the pump-probe technique with the experimental configuration described in section 2.5.1. Here we will describe the polarization configuration of both beams and how the signal is detected. As described in the previous section, we will consider the polar MOKE configuration, with the light beam propagating perpendicular to the surface of the monolayer.

First, regarding the pump beam, depending on the polarization of interest we set the QWP at $\pm 45°$ with respect to the axis of the polarizer P2 which defines whether we

excite with right or left circularly polarized light. For the case of the probe, we use the Jones calculus formalism to write the linearly polarized beam at 45° as:

$$\vec{E}_0 = \frac{1}{\sqrt{2}}\begin{pmatrix}1\\1\end{pmatrix}. \tag{2.16}$$

Then, the beam passes by the photoelastic modulator (PEM) which is a birefringent crystal that compresses periodically in one direction. Due to this oscillation, the PEM modulates the propagation velocity between the x an y components of the light which results in a phase difference and the oscillation of the polarization. The Jones matrix associated with the PEM is given by:

$$M(t) = \begin{pmatrix}1 & 0\\ 0 & e^{iA_0\cos\Omega t}\end{pmatrix}, \tag{2.17}$$

where A_0 is the amplitude of the retardance between the two components of the light, Ω is the modulation frequency, set at 50 kHz, and t is the time. Note that the matrix describes the PEM aligned with its fast axis at 45°to the linearly polarized probe. Therefore, the resulting beam after the PEM is given by:

$$\vec{E}(t) = M(t)\frac{1}{\sqrt{2}}\begin{pmatrix}1\\1\end{pmatrix} = \frac{1}{\sqrt{2}}\begin{pmatrix}1\\ e^{iA_0\cos\Omega t}\end{pmatrix}, \tag{2.18}$$

and indicates that if $A_0 = \pi/2$ the PEM will modulate the polarization of the light between σ_+ and σ_-. Then, the modulated probe will reach the sample. Due to the considered symmetry of the system, we can write the reflection matrix of the sample as

$$S = \sqrt{R}\begin{pmatrix}1 & -\Phi\\ \Phi & 1\end{pmatrix} \tag{2.19}$$

where R is the reflectivity, and Φ the complex phase defined in equation 2.15. The reflected beam is then sent towards the analyzer A. The matrix of the polarizer with its axis at an angle γ with respect to the horizontal axis is defined as:

$$A(\gamma) = \begin{pmatrix}\cos^2\gamma & -\cos\gamma\sin\gamma\\ -\cos\gamma\sin\gamma & \sin^2\gamma\end{pmatrix}. \tag{2.20}$$

Where γ should be placed aligned with the main axis of the PEM, which is at 45°with respect to the polarizer P1 to maximize the Kerr rotation signal. Under this configuration, the detected intensity in the photodetector is constant with a value of $R/2$. In our description, this implies $\gamma = 0$, simplifying the calculations. Hence, the resulting light at the photodetector is given by:

$$\begin{pmatrix} E_x \\ E_y \end{pmatrix} = \frac{1}{\sqrt{2}} AS \begin{pmatrix} 1 \\ e^{iA_0 \cos \Omega t} \end{pmatrix}. \tag{2.21}$$

Operating all the Jones matrices and vectors, we can determine the electric field that arrives at the photodiode detector. Then, the measured intensity at the photodetector is given by $I = \vec{E}^* \vec{E}$, which calculated results in:

$$I = R \left(\frac{1}{2} + \theta_K \cos \left[A_0 \cos(\Omega t) \right] + \varepsilon_K \sin \left[A_0 \cos(\Omega t) \right] \right). \tag{2.22}$$

However, this signal still needs to be filtered and amplified to eliminate noise and determine which frequencies of the signal are coming from a specific modulated source. With this purpose, it is convenient to expand equation 2.22 in its harmonics using the Jacobi-Anger expansion. With this, we can separate the total measured signal into three components:

$$V_{DC} = R \left(\frac{1}{2} + \theta_K J_0(A_0) \right), \tag{2.23}$$

$$V_{1\Omega} = \varepsilon_K R J_1(A_0) \cos(\Omega t), \tag{2.24}$$

$$V_{2\Omega} = \theta_K R J_2(A_0) \cos(2\Omega t), \tag{2.25}$$

where J_n is the nth order Bessel function. We can identify a DC signal (V_{DC}), a signal that depends on the frequency of the modulation (first harmonic $V_{1\Omega}$), and one that depends on double the frequency of the modulation (second harmonic $V_{2\Omega}$). From here, we observe that we can set the first lock-in amplifier to the second harmonic for detecting the Kerr rotation θ_K, but we could also set it to the first harmonic to determine the Kerr ellipticity ε_K. Also, we notice that we can maximize the signal of interest by adjusting the retardance A_0 of the PEM. Due to the relation with the Bessel function, we can select the retardance to maximize J_1 for Kerr ellipticity, or J_2 for Kerr rotation. In this work, we are interested in the last one, which implies A_0=3.054, used in our experiments. Finally, the filtered signal will be sent to the second lock-in, set at the frequency of the chopper, to amplify the signal of the probe modulated by the pump.

2.7 Differential reflectivity

One important tool for monitoring charge dynamics is time-resolved differential reflectivity (TRDR). Using pump-probe, this technique measures and analyzes the variations in the reflectivity of a sample when it is excited ($R_{pump\ on}$), comparing it to the reflection observed without excitation ($R_{pump\ off}$). It is defined as

$$\frac{\Delta R}{R} = \frac{R_{pump\ on} - R_{pump\ off}}{R_{pump\ off}}. \tag{2.26}$$

Depending on the type of interaction of the sample with the light, it is possible to classify the signal response into three: photobleaching, photoinduced absorption, and stimulated emission (see Figure 14). In photobleaching (PB) the pump pulse excites and saturates the accessible states in the conduction band, therefore, fewer probe photons are absorbed by the material, resulting in a higher reflectivity, compared to the absorption of the material before the pump. In photoinduced absorption (PIA), the pump pulse excites occupied states in the conduction band, which let new accessible states for the probe beam. This results in negative signals of differential reflectivity, as the material is temporarily able to absorb more probe photons. Finally, in stimulated emission, when the material is excited by the pump pulse, electrons are raised to higher energy levels. Later, when the probe photons arrive, if they possess the same energy as the excited state to the ground state transition, they can stimulate the excited electrons to recombine radiatively. These emitted photons are coherent with the incoming ones, resulting in an amplification of the overall signal.

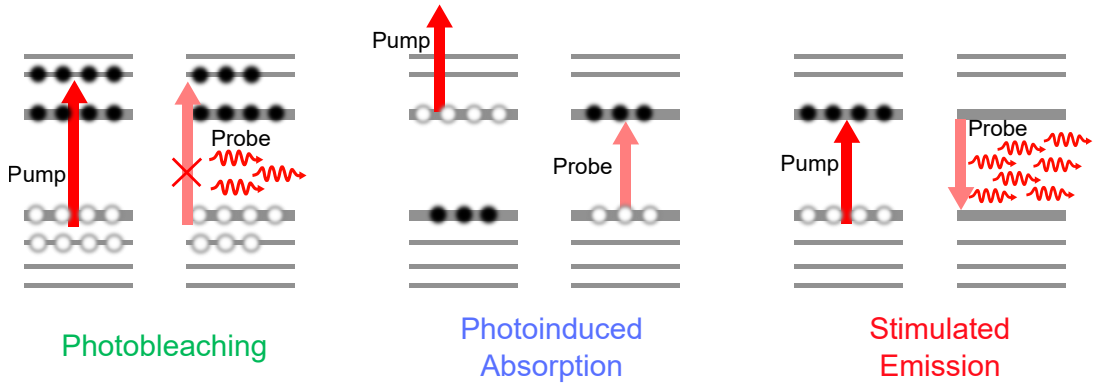

Figure 14 – Schematics of the three main responses in TRDR measurements: photobleaching, photoinduced absorption, and stimulated emission.

We proceed now to detail the polarization and detection system shown in Figure 12b and used in our TRDR measurements. We used linearly polarized light for both pump and probe beams. Therefore, we set the fast axis of the quarter-waveplate QWP parallel to the axis of the polarizer P2 to keep the polarization of the beam unchanged. For the detection, we used the double modulation technique as depicted in Figure 12b, and set the analyzer (A) parallel to the polarizer P1 in the probe. The fast axis of the PEM is oriented at 45°respect to P1 and set to a retardance of 3.054, which induces an oscillation of the polarization of the probe from right circularly polarized to left circular polarized, with a frequency of Ω=50 kHz. This oscillation signal is sent as a reference to lock-in 1. As the

polarization keeps oscillating, the light will be at a linearly polarized state with a frequency of 2Ω. Hence, we set lock-in 1 to filter and amplify the signal from the photodetector in the second harmonic configuration 2Ω. Here, the Jones matrix calculation, with $\Phi \sim 0$, the signal of interest is given by $V_{2\Omega} = RJ_2(A_0)\cos(2\Omega t)$. Finally, the second lock-in is set at the same frequency chopper of the pump, at 70 Hz. This gives us the pump-induced change in reflectivity.

CHAPTER 3

Photoluminescence and charge transfer in the prototypical 2D/3D semiconductor heterostructure MoS_2/GaAs

The new generation of two-dimensional (2D) materials has shown a broad range of applications for optical and electronic devices. Understanding the properties of these materials when integrated with the more traditional three-dimensional (3D) semiconductors is an important challenge for the implementation of ultra-thin electronic devices. Recent observations have shown that by combining MoS_2 with GaAs it is possible to develop high quality photodetectors and solar cells. Here, we present a study of the effects of intrinsic GaAs, p-doped GaAs, and n-doped GaAs substrates on the photoluminescence of monolayer MoS_2. We observe a decrease of an order of magnitude in the emission intensity of MoS_2 in all MoS_2/GaAs heterojunctions, when compared to a control sample consisting of a MoS_2 monolayer isolated from GaAs by a few layers of hexagonal boron nitride. We also see a dependence of the trion to A-exciton emission ratio in the photoluminescence spectra on the type of substrate, a dependence that we relate to the static charge exchange between MoS_2 and the substrates when the junction is formed. Scanning Kelvin probe microscopy measurements of the heterojunctions suggest type-I band alignments, so that excitons generated on the MoS_2 monolayer will be transferred to the GaAs substrate. Our results shed light on the charge exchange leading to band offsets in 2D/3D heterojunctions which play a central role in the understanding and further improvement of electronic devices.

Chapter published in Applied Physics Letters **119**, 233101 (2021) [76].

3.1 Introduction

Layered transition metal dichalcogenides (TMDs) are among the most studied two-dimensional (2D) materials in the last decade. Their atomically-thin structure and physical properties have attracted attention not only because of their interesting fundamental physics but also due to their potential applications for ultra-thin technological devices [77–84]. Similar to graphene, these materials can be mechanically exfoliated to obtain single layers. Of special interest are MoS_2, $MoSe_2$, WS_2 and WSe_2, TMDs that have been widely studied mostly because they suffer a transition from an indirect to a direct bandgap semiconductor when the monolayer thickness is achieved [2, 4]. As a consequence, the photoluminescence (PL) of the monolayer of these materials is much more intense when compared to that of the bulk material [4]. Also, owing to their two-dimensional nature, TMD monolayers have their PL spectra dominated by excitonic effects. For monolayer MoS_2, a characteristic PL spectrum can usually be decomposed into three main peaks related to the recombination of different excitons, the so-called A and B excitons, and charged excitons, the trions [85]. The large spin-orbit splitting (SOS) at the top of the valence band is responsible for the existence of the two exciton states, A and B [4, 11], while the third PL peak routinely observed in the PL spectrum of monolayer MoS_2 corresponds to charged A-excitons, or trions, which are tightly bound and are observed even at room temperature [6].

In the monolayer limit, the properties of all TMDs are highly affected by the substrate on which they are deposited [44,86]. One interesting substrate for these monolayer materials is GaAs, a prototypical semiconductor which has been extensively studied and employed for electronics and optoelectronics applications that take advantage of its direct gap (1.42 eV at room temperature) and relatively high electron mobility (up to 8000 $cm^2\ V^{-1}\ s^{-1}$ at room temperature) [87]. The combination of the optical and electronic properties of TMDs and GaAs as a substrate has already shown promising results for implementation of solar cells [83], with a power conversion efficiency of up to 9.03%, and photodetectors [79, 81, 82, 88], with a detectivity of up to 1.9×10^{14} Jones. The success of these proof-of-concept studies urges the need to investigate in detail the properties of MoS_2/GaAs heterojunctions, in order to further improve device quality [89]. Particularly, the band alignment between the two materials is still not well established although it is of major importance for applications involving these 2D/3D semiconductor architectures.

Here, we present a study of the effect of GaAs substrates on monolayer MoS_2 by analyzing the changes in the photoluminescence spectra of monolayer MoS_2 on GaAs substrates with different doping levels. We used three types of commercially-available GaAs substrates that we identify hereon as i-GaAs for intrinsic GaAs (semi-insulating), p-GaAs for Zn-doped p-type GaAs and n-GaAs for Si-doped n-type GaAs. The doping concentrations are $\sim 10^{18}\ cm^{-3}$ for both n-GaAs and p-GaAs. As a reference, we have control

samples on two substrates, SiO_2/Si and n-GaAs, with the transferred MoS_2 monolayer isolated from the substrates by a bulk hexagonal boron nitride (hBN) flake. We propose a type-I band alignment, with a charge transfer between GaAs and the MoS_2 monolayer which depends on the GaAs doping. This band alignment model is supported by Scanning Kelvin Probe Microscopy (SKPM) measurements in the heterostructures.

3.2 Experimental Methods

Monolayers of MoS_2 (ML-MoS_2) were mechanically exfoliated and transferred to the substrates through the all-dry viscoelastic stamp method [63]. Similar processes were used to exfoliate and transfer the hBN bulk to the Si/SiO_2 and n-GaAs substrates. To confirm the single layer character of the MoS_2 flakes we used Raman spectroscopy to monitor the separation in frequency of the well-known A_{1g} and E^1_{2g} Raman modes [90, 91], see Figure 19 in the Appendices 3.5.

The samples were studied in two sets. The first set was composed of a control sample of ML-MoS_2 on hBN/SiO_2/Si substrate (MoS_2/hBN/SiO_2) and three samples of ML-MoS_2 on GaAs with different doping: MoS_2/i-GaAs, MoS_2/p-GaAs and MoS_2/n-GaAs. The second set is composed of two samples, one ML-MoS_2 on n-GaAs and one ML-MoS_2 control sample on hBN/n-GaAs substrate (MoS_2/hBN/n-GaAs). The second set of samples allowed us to verify the reproducibility of the results obtained for ML-MoS_2 as well as to produce a control sample with a dielectric environment that allows better comparisons of SKPM measurements made on different samples (see sec. 3.5.2 for further details).

3.3 Results and discussion

We start our considerations by the PL measurements, which were accomplished with the same experimental conditions for all the samples. We are cautious with the laser exposure and spectra acquisition to minimize changes in the PL caused by photodoping effects [92] and to allow the comparison of PL spectra from different samples (details are provided in the Appendix 3.5.4). The ML-MoS_2 spectra were obtained after removing the background photoluminescence from the GaAs substrate when applicable (Appendix 3.5.4). In Figure 15a we present the ML-MoS_2 emission for the first set of samples. The intensity of the emission from ML-MoS_2 is approximately the same (within experimental resolution) for all MoS_2/x-GaAs (x=p, n, i) samples. However, their PL signals are around 10 times less intense than that of the ML-MoS_2 from the MoS_2/hBN/SiO_2 control sample. This observation suggests an important quenching mechanism for the ML-MoS_2 photoluminescence in the MoS_2/x-GaAs 2D/3D heterostructures, which is independent

of the substrate doping level. We suggest two main paths for the reduction of PL from MoS_2 on GaAs: exciton dissociation through the junction and exciton transfer from MoS_2 to GaAs. The first process will contribute more if ML-MoS_2/x-GaAs form a type II heterojunction and the latter will be more important in a type I heterojunction. Therefore, we will try to elucidate the band alignment of the heterojunctions with other observations and the discussion that follows.

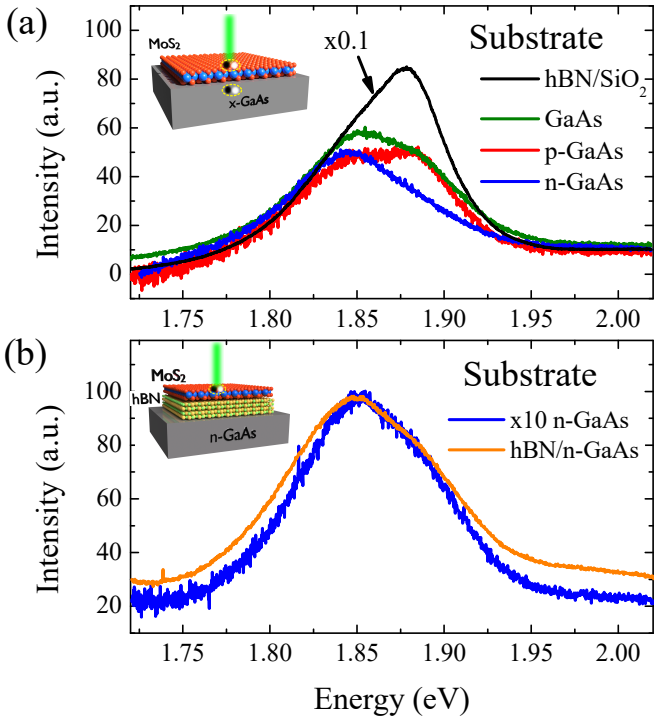

Figure 15 – Photoluminescence spectra of ML-MoS_2 from the first set of samples (a) and from the second set of samples (b). Insets: Representation of the studied samples on x-GaAs substrate (a) and on hBN/n-GaAs substrate (b).

The results shown in Figure 15a are consistent with measurements on a second set of samples: MoS_2/hBN/n-GaAs and MoS_2/n-GaAs. We observe a 10:1 relation between the PL of the sample containing the hBN spacer to the one without this spacer (Figure 15b). This confirms that the hBN bulk layer worked well to isolate the ML-MoS_2 from the n-GaAs substrate, preventing exciton dissociation/transfer. From now, we are going to consider just the control sample of the second set, as it presents a comparable dielectric environment with the first set of samples.

To further understand the interaction between MoS_2 and GaAs in the heterostructures we decompose the PL spectra into peaks corresponding to the radiative recombination of different exciton species on ML-MoS_2. In Figure 16 we present the PL spectra and their constituent peaks for all ML-MoS_2 on GaAs from the first set of samples and for the MoS_2/hBN/n-GaAs control sample. Four peaks with a Voigt lineshape were identified in the fitted spectra, the A and B exciton peaks, the trion peak (T), and a fourth peak (L),

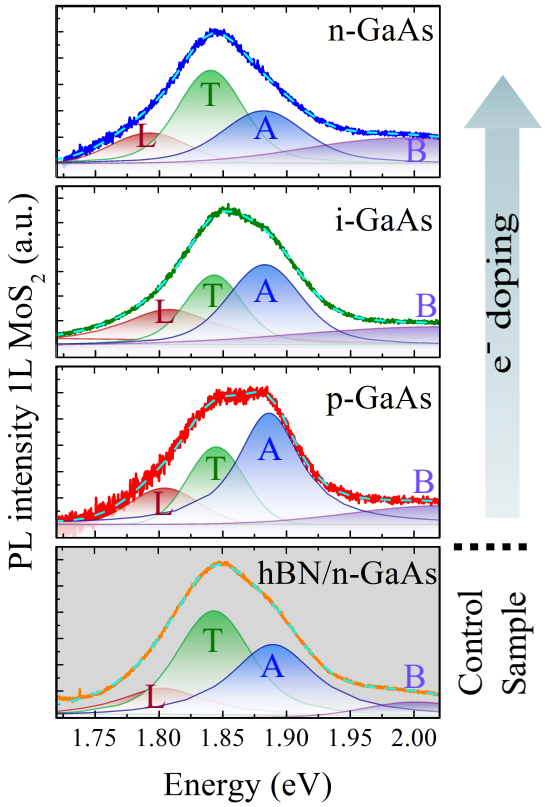

Figure 16 – Peak decomposition of the photoluminescence spectra of ML-MoS_2 on different substrates. The peaks are contributions from: localized states (L), trions (T), A excitons (A), and B exciton (B) emissions. The solid lines are experimental data and the dashed lines represent the sum of the component peaks.

which has been previously assigned to the recombination of excitons bound to localized states [85, 93–95].

The presence of a peak from recombination of trions, which are charged excitons, allows us to infer the existence of free charge, or an excess charge density, in ML-MoS_2. Exfoliated ML-MoS_2 are usually found to be intrinsically n-type [96, 97], having excess electrons in its conduction band. Thus, by comparing the integrated PL intensities of the trion peak, I_T, and of the A-exciton peak, I_A (see Table 2) we can quantify the excess charge density comparatively among the samples and identify the relationship between the doping level of the substrate and the excess charge density on ML-MoS_2. A higher value of the ratio I_T/I_A indicates higher excess charge density, as was observed for monolayers under electric gating [6, 80, 95]. Based on I_T/I_A values (table 2) we can say that the excess charge density on ML-MoS_2 in our samples increases, depending on the substrate, in the following order: p-GaAs, i-GaAs, hBN/n-GaAs and n-GaAs. By assumption, the ML-MoS_2 in the control sample does not exchange charge with the substrate, therefore its I_T/I_A is a measure of the isolated ML-MoS_2 excess electron density. The high contribution of trions in the control sample PL spectrum corroborates this assumption since it agrees with the already mentioned intrinsic n-type nature of exfoliated ML-MoS_2 samples, mostly

related to sulfur vacancies [96,97]. Comparing the I_T/I_A of the MoS_2/x-GaAs samples with the control sample we can infer that the n-GaAs substrate is the only one that transfers electrons to the monolayer, while inversely the i-GaAs and p-GaAs substrates receive electrons transferred from the MoS_2 monolayer.

The excess charge density on ML-MoS_2 is controlled by its Fermi level position. We expect that when the ML-MoS_2 and the substrate enter into contact they exchange charge carriers until their Fermi levels align, achieving an equilibrium state. This process may change the surface potential of GaAs causing some band bending but its Fermi level position is fixed by the bulk far from the surface. For ML-MoS_2, however, charge exchange will change its Fermi level position. Thus, the relations between I_T/I_A among the samples give us a hint about the Fermi level change in ML-MoS_2 when it comes into contact with each substrate. Then, from a band alignment point of view, we may say that the Fermi level of ML-MoS_2, before contacting the substrate, is positioned somewhere between the Fermi level of the intrinsic and n-doped GaAs substrates. Nevertheless, from the I_T/I_A connections alone, we cannot determine the band alignments for the different heterojunctions.

Sample	I_A	I_T	I_T/I_A
MoS_2/n-GaAs	19.66	26.25	1.33
MoS_2/i-GaAs	27.86	19.12	0.69
MoS_2/p-GaAs	37.13	16.31	0.44
MoS_2/hBN/n-GaAs	666.82	745.26	1.12

Table 2 – Integrated photoluminescence intensities of the A exciton, I_A, and the trion, I_T, emission peaks of ML-MoS_2 in each sample, in arbitrary units, and their ratio, I_T/I_A.

In order to elucidate the band offsets of the three ML-MoS_2/x-GaAs heterojunctions, we used Scanning Kelvin Probe Microscopy (SKPM), which measures the contact potential difference (CPD) between the cantilever tip of an atomic force microscope and the surface of the sample [98, 99]. In the biased tip configuration, which we used for the SKPM measurements, by measuring the CPD and knowing the work function of the tip, ϕ_{tip}, it is possible to determine the surface work function of the sample, ϕ_{samp}, through the relation $e \cdot CPD = \phi_{tip} - \phi_{samp}$, where e is the electron charge. We performed the experiments under standard ambient conditions, which can affect the precision of the specific values. Nevertheless, all uncertainties affect all samples equally, and we can confidently extract relationships between the surface work functions of the different materials in each sample measured.

To extract the CPD at each material we used the mean value of homogeneous areas of the monolayers, shown in Figure 17 by dashed black lines, and the clean areas at each

x-GaAs substrate, shown by dashed white lines in the figure. Optical images and sample details are shown in the Appendices 3.5. Therefore, it is possible to determine the difference between the work functions of the ML-MoS_2 and its corresponding substrate by the negative of the value of the CPD contrast, or $\Delta\phi_{MoS_2-GaAs} = \phi_{MoS_2} - \phi_{GaAs} = e\,(V_{GaAs} - V_{MoS_2})$ (see Table 3). We observe that the obtained difference is positive for all samples, which indicates that the work function of MoS_2 is larger than the work function at the surface of GaAs in all samples.

To relate the work function of a material with its conduction and valence band edges we need to know the electron affinity χ and band gap E_g of the material. The GaAs parameters are well established in literature: $\chi_{GaAs} = 4.07$ eV and $E_{g,GaAs} = 1.42$ eV [87]. For ML-MoS_2, reports in the literature have a range of $\chi_{MoS_2} = 3.74$ - 4.1 eV [100, 101] and the bandgap will suffer modulations owing to the dielectric screening from the environment, which in our samples should imply a value of $E_{gMoS_2} \sim 2.2$ eV considering the dielectric constant of GaAs as κ_{GaAs}= 12.88 [102]. To propose a band alignment for our heterojunctions we will consider $\chi_{MoS_2} = 4.0$ eV, which was the value used in other works on MoS_2/GaAs [82, 83, 89] and the electronic bandgap.

Since the position of the conduction band can be described as $E_c = \phi - \chi$, with respect to the Fermi level, we approximate the difference in the conduction band edge between the MoS_2 layer and the x-GaAs substrate by $\Delta E_c = E_{c,MoS_2} - E_{c,GaAs} = \Delta\phi_{MoS_2-GaAs} + \Delta\chi_{GaAs-MoS_2}$. As both quantities are positive, the conduction band edge

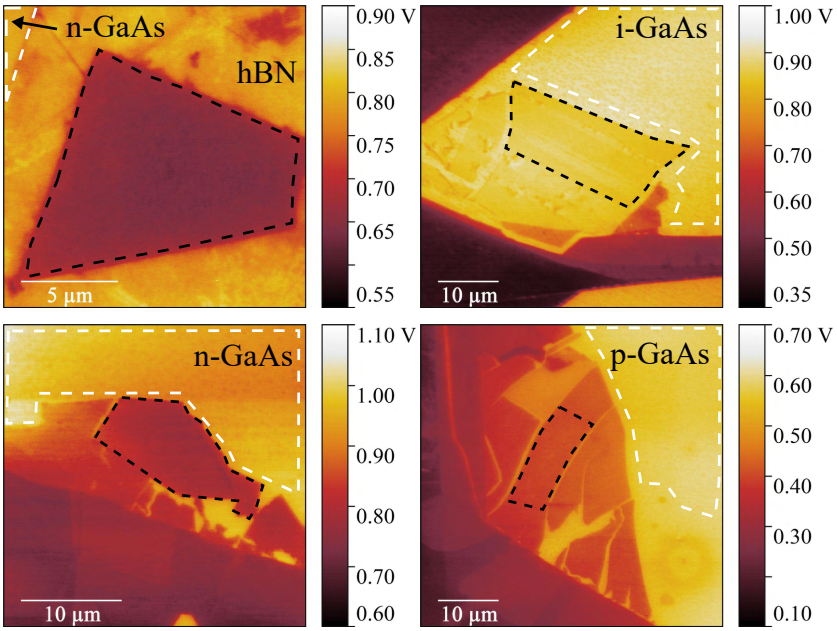

Figure 17 – Contact potential difference maps obtained by SKPM of the studied heterojunctions. ML-MoS_2 (substrate) analyzed areas are delimited by black (white) dashed lines. The type of substrate is indicated in each map in a region of the image that corresponds to the substrate.

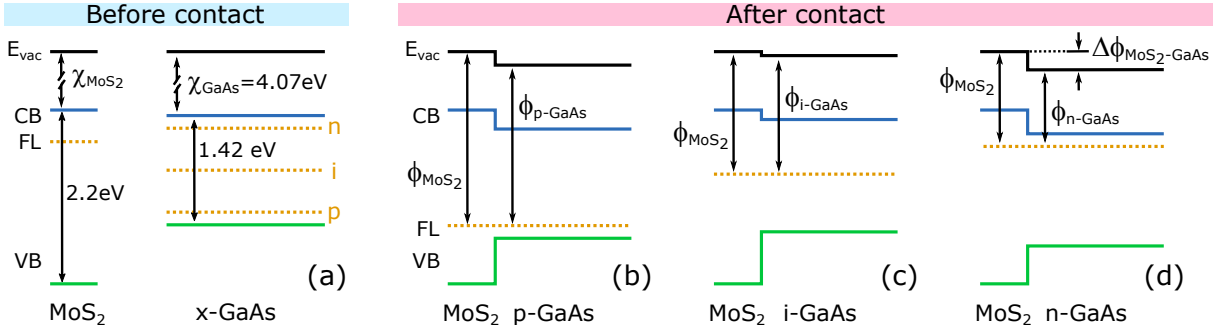

Figure 18 – Schematic band offsets of ML-MoS_2 and x-GaAs before contact (a), and after ML-MoS_2/x-GaAs heterojunction formation (b-d). E_{vac}, CB, FL, VB, χ, and Φ represent the vacuum level, the bottom of the conduction band, the Fermi level, the top of the valence band, the electron affinity, and the work function respectively.

Sample	$\Delta\phi_{MoS_2-GaAs}$ (eV)
MoS_2/n-GaAs	0.23 ± 0.04
MoS_2/i-GaAs	0.05 ± 0.05
MoS_2/p-GaAs	0.22 ± 0.03
MoS_2/hBN/n-GaAs	0.14 ± 0.01

Table 3 – Work function difference between ML-MoS_2 and GaAs extracted from the SKPM maps shown on Figure 17.

of MoS_2 is always at a higher energy than that of GaAs, with their Fermi levels aligned.

Figure 18 presents schematically the band offsets we propose for the ML-MoS_2/x-GaAs heterojunctions based on our analysis of the PL and SKPM results. In Figure 18a we present the band edges and Fermi levels of each material before contact. Fermi levels are represented by the yellow dotted lines and, in GaAs, are labeled n, i, and p for the type of substrate doping. As inferred from the PL I_T/I_A analysis, we position the Fermi level of MoS_2 between those of i-GaAs and n-GaAs. Heterojunction band alignments after contact are shown in Figures 18b, 18c and 18d. According to our proposal, ML-MoS_2 and GaAs form type I heterojunctions for all GaAs doping levels studied.

The SKPM data does not give a quantitative, exact value of the conduction band offset in the heterojunction (see Appendix 3.5.2 for more details on the technique). Nevertheless, there is a clear indication that the steps in conduction band at the junction are of comparable magnitude for all three types of GaAs substrates. After establishing the conduction band step at the junction, the position of the Fermi level is set by the doping of the GaAs substrate, according to the assumption that the Fermi level is pinned down by the bulk of the material. This determines the position of the Fermi level in the MoS_2 side of the junction.

As the estimated differences in work function obtained from SKPM are between the surface work functions, the band alignments we present in Figure 18 assume that the surface work function of GaAs is the same as its bulk work function, or that the GaAs bands are flat. We prefer not to speculate on the curvature of the bands inside GaAs because our experiments do not provide sufficient evidence to support it. This means that, although at the interface the band positions we proposed should be correct, the curvature of the GaAs bands may change as one moves from the surface to the bulk, which means that the Fermi level positioning should also be reexamined. Therefore, we propose the band alignments in Figure 18 as a first approximation, to contribute to the discussion and analysis of the surface and charge dynamics in these 2D/3D heterostructures and we expect to instigate other works aiming to elucidate the shape of the bands inside GaAs on these types of junctions, since band bending can affect the operation of devices based on them.

Most of the work done on MoS_2/GaAs junctions so far employ n-doped GaAs [79,81–83,89]. Nearly all of these works propose a type II band alignment for MoS_2/n-GaAs. That is not in complete disagreement with our proposal, since the transition to type II alignments for the MoS_2/n-GaAs junctions would only imply that the conduction band step is larger than the one we estimated, which is based in comparisons of the experimental data for the three types of MoS_2/x-GaAs junction and the control sample. Furthermore, it is worth pointing out that the devices studied in these other works were built with MoS_2 produced by chemical vapour deposition (CVD) [82, 83, 89], thermal decomposition [81] or solution processing [79, 88], while we used exfoliated ML-MoS_2. That could be relevant since it is well known that the defects, and thus doping, of MoS_2 monolayers obtained through each method can be quite different.

Our proposed type I band alignments for all the studied heterojunctions implies that the mechanism behind the quenching of the ML-MoS_2 photoluminescence in the heterojunctions should be the transfer of excitons from MoS_2 to GaAs and not exciton dissociation through the junction. Additionally, the different Fermi level positions in ML-MoS_2 on different substrates allows us to explain the variations in the relative intensity of the emission from the trion and the A exciton that were observed.

3.4 Conclusions

In conclusion, we presented the photoluminescence spectra of monolayers of MoS_2 on commercial GaAs substrates with different doping levels. The results revealed an important reduction of the PL intensity of the monolayers, when compared with a control sample. In addition, the spectra presented a dependence of the ratio of the trion to exciton emission intensities on the doping level of the substrate. This behavior evidences different

ammounts of excess charge in the single layers related to a charge exchange process with their substrates. Scanning Kelvin probe microscopy measurements provided an estimation of the difference in work function between the materials in the heterojunctions and allowed us to propose a type I band alignment for all MoS_2/x-GaAs heterojunctions we studied. Our proposal is consistent with the analysis of the photoluminescence measurements and suggests exciton migration as the main mechanism behind the PL intensity reduction. The results reported here contribute to the understanding of the charge transfer processes in 2D/3D semiconductor heterojunctions which are of central importance for the implementation of the next generation of electronic and optoelectronic devices.

Acknowledgments

An important part of the work reported here was done at the LCPNano laboratory at UFMG. We thank Freddie Hendriks for the calculations of thin-film interference effects shown in the Appendices. This work was financially supported by the Brazilian funding agencies CNPq, FAPEMIG and the Coordenação de Aperfeiçoamento de Pessoal de Nível Superior - Brasil (CAPES).

3.5 Appendices

3.5.1 Sample fabrication and characterization

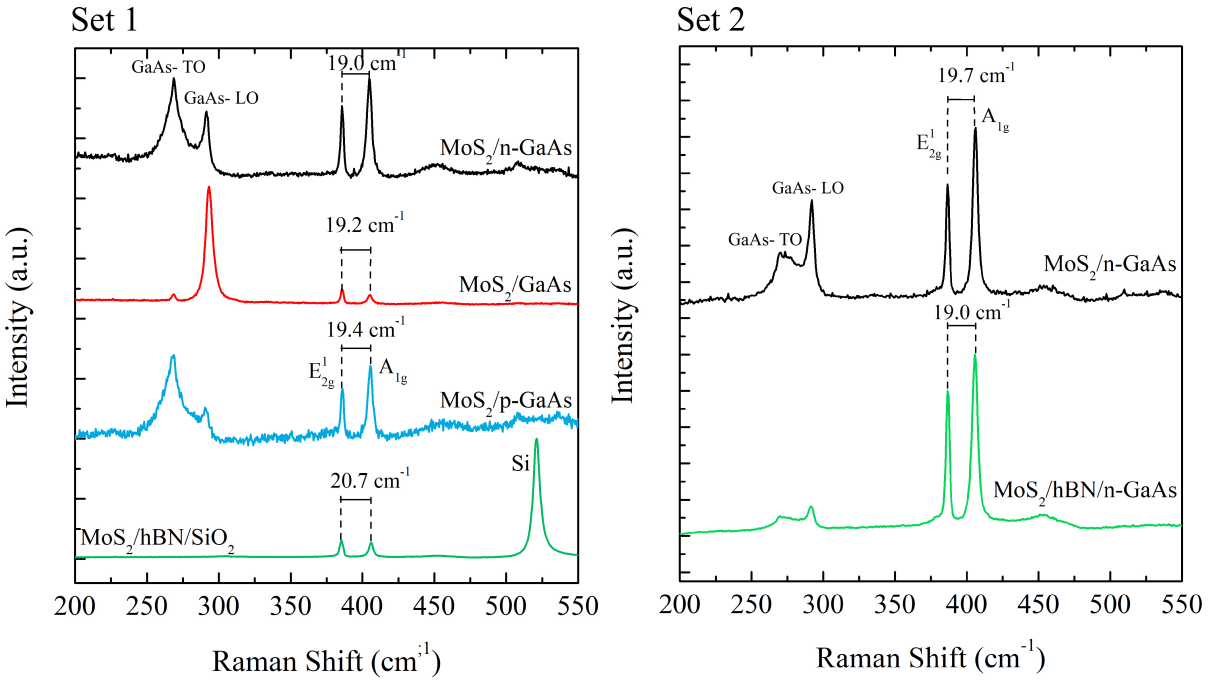

Figure 19 – Raman spectra of ML MoS_2 on the studied substrates. All samples show the Raman shift separation between the MoS_2 A_{1g} and E_{2g} peaks that is characteristic of MoS_2 single layers. Optical phonon modes from the substrates can also be seen in the spectra.

The samples were studied in two sets. The first set was composed of a control sample of monolayer MoS_2 on hBN/SiO_2/Si substrate (MoS_2/hBN/SiO_2) and three samples of ML-MoS_2 on GaAs with different doping: MoS_2/i-GaAs, MoS_2/p-GaAs and MoS_2/n-GaAs. The second set is composed of two samples, one ML-MoS_2 on n-GaAs and one ML-MoS_2 control sample on hBN/n-GaAs substrate (MoS_2/hBN/n-GaAs). The second set of samples allowed us to confirm the insulating quality of hBN on the control samples as well as to verify the reproducibility of the results obtained for ML-MoS_2 on n-GaAs.

To fabricate the samples, we cleaned the Si/SiO_2 substrate via isopropyl alcohol and acetone baths for 5 minutes each, followed by high-pressure N_2 gas to eliminate any possible impurity. In addition, GaAs substrates were also cleaned by Ar plasma for 15 minutes at 0.300 Torr and 250 W RF power after the wet cleaning. Monolayers of MoS_2 (ML-MoS_2) were mechanically exfoliated and transferred to the substrates through the all-dry viscoelastic stamp method [63]. Similar processes were used to exfoliate and transfer the hBN bulk to the Si/SiO_2 and n-GaAs substrates.

To confirm the monolayer nature of the MoS_2 in our samples , we used Raman spectroscopy, with a 532 nm laser at 0.5 mW. In monolayer MoS_2, the separation in frequency of the well-known A_{1g} and E^1_{2g} Raman modes, should be close to, or smaller than, 19 cm^{-1} [90, 91]. The obtained spectra are presented in Figure 19. In addition to the mentioned peaks, we can see the TO and LO Raman modes of the GaAs substrates as well as the Si peak of the control sample in set 1.

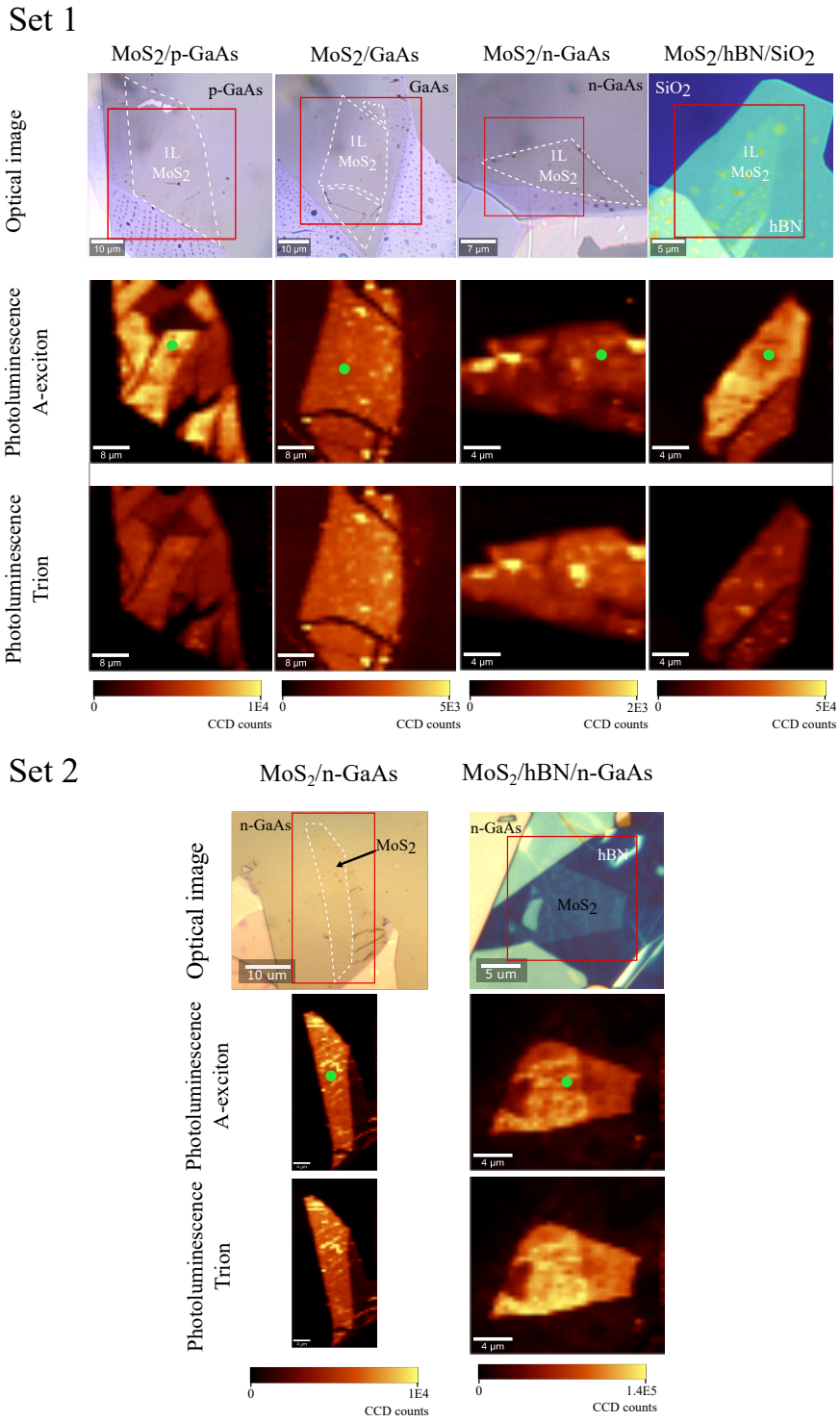

Figure 20 – Optical images and photoluminescence maps of the studied samples.

Photoluminescence spectra were measured in a WITec *alpha 300A* experimental setup with a laser power of 300 μW, at a wavelength of 457 nm. The spectra presented in Figures 1 and 2 of the main document were acquired as the average of 4 consecutive measurements accumulated for 40 seconds, at the points shown by the green dots in Figure 20. The latter presents the optical image of the samples and two sets of PL maps, obtained by integrating the PL spectrum at each point in a region of 20 meV width, with the center in 1.88 eV for the middle panel, and 1.84 eV for the bottom panel. The color scale is the same for both panels of each sample and is shown at the bottom of the figure. The PL maps in Figure 20 were acquired with accumulation time of approximately one second per spectra and obtained with spatial steps of 0.5 μm. Raman spectra were measured with acquisitions of 1 minute. PL spectra and Raman spectra were obtained at different representative points of the sample and the PL maps were done afterwards, to minimize photodoping effects.

3.5.2 SKPM measurements

There are several types of SKPM methods (amplitude-modulation (AM), frequency-modulation (FM), homodyne-detection, heterodyne-detection and others) [69, 103–105]. Some good reviews on this subject are presented in references [103] to [105] and references therein. As a general rule, AM-based SKPM in ambient conditions yields qualitative surface potential values, whereas FM-based SKPM is employed when quantitative surface potential values are needed. This is mainly due to the strong influence of the cantilever (and not only the tip apex) on the SKPM signal in AM-based methods [69, 103–105]. In the present work, the SPM system used is capable of conventional AM-based SKPM only and, thus, the yielded results should be considered qualitative.

To work within the limitations of the method and still be able to make reliable comparisons between samples we elect the control sample from the second set, with a substrate of n-GaAs below the hBN flake, as the better control sample for SKPM measurements. It allows us to have a similar cantilever-substrate interaction effect on the SKPM measurements.

In particular, our measurements were conducted on Bruker Multimode 8 with a Nanoscope V controller, at normal atmospheric pressure and room temperature.

3.5.3 Atomic force microscopy

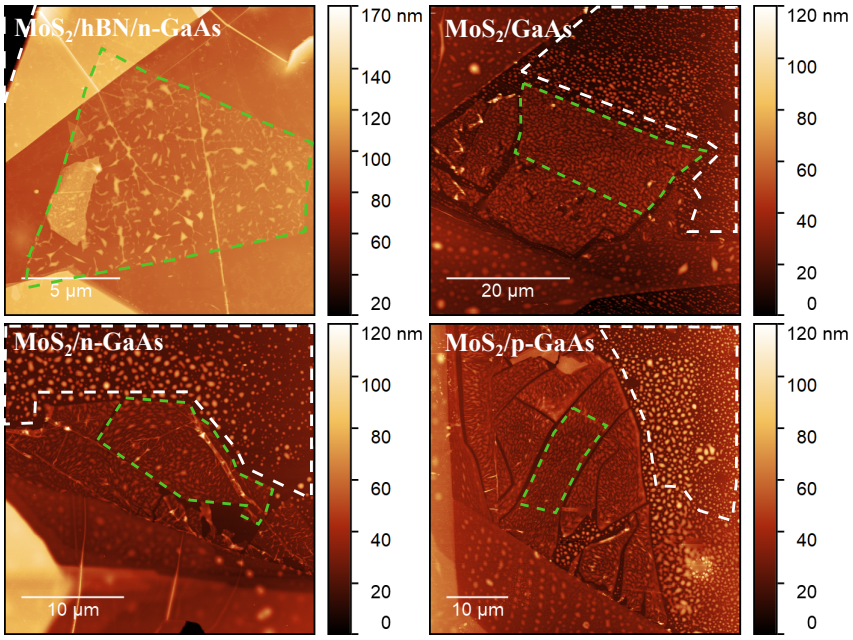

Figure 21 – Atomic force microscopy topographic images of the studied samples. ML-MoS_2 (substrate) analyzed areas are delimited by green (white) dashed lines.

3.5.4 Photoluminescence

Since GaAs and MoS_2 have direct bandgaps with relatively close energy values and owing to the atomic thickness of the MoS_2, the photoluminescence spectra obtained from MoS_2/GaAs heterojunctions are composed of emissions from both materials. By subtracting the emission of the substrate from the heterojunction spectra we are left with the ML-MoS_2 emission. For the MoS_2/hBN/SiO_2 control sample, the substrate does not have a strong PL signal and the PL spectrum measured on the heterostructure is already the ML-MoS_2 emission. Figure 22 illustrates the separation process for the spectrum of MoS_2 on n-GaAs.

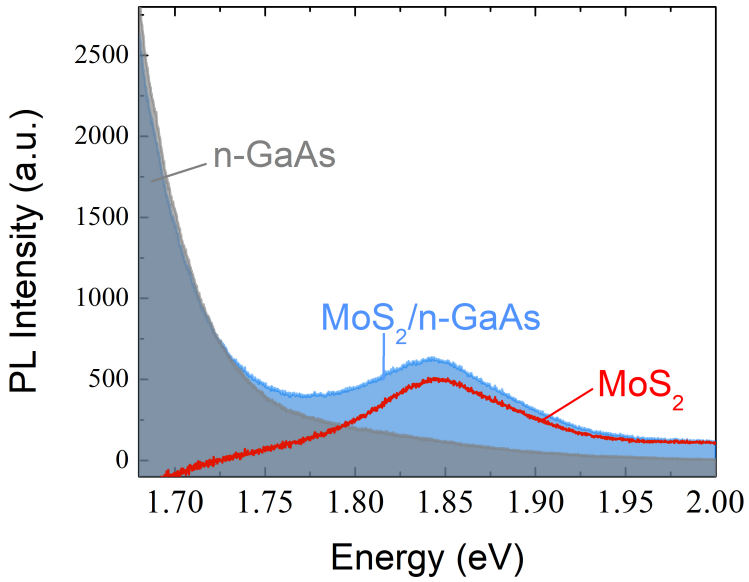

Figure 22 – Photoluminescence (PL) spectra substraction of MoS_2/n-GaAs. In gray the PL from the bare substrate, in blue the PL measured on the monolayer MoS_2 on the n-GaAs substrate, in red the resulting PL of gray minus blue.

3.5.4.1 Photodoping effect

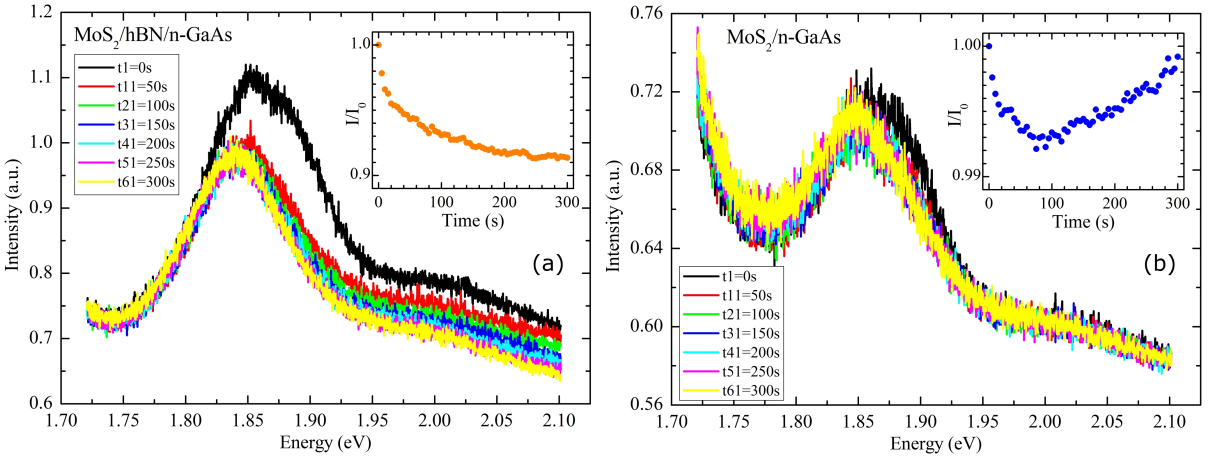

Figure 23 – Photodoping effect investigation. Spectra obtained by continuously illuminating the sample with the 457 nm laser, with power of 300 μW and accumulation time of 1 s for the MoS_2/hBN/n-GaAs in (a) and 3 s for MoS2/n-GaAs in (b). Spectra were acquired every 5 s, but we only show the spectra obtained at times 0, 50, 100, 150, 200, 250 and 300 s, for clarity. Insets show the time (exposure) dependence of the relative integrated intensity, I/I0, which is the integrated intensity of each spectrum divided by the integrated intensity of the first spectrum at t = 0 s. The intensity variation along the measurement is less than 10% for MoS_2/hBN/n-GaAs, and less than 1% for MoS_2/n-GaAs. The plots show raw data where MoS_2 and GaAs emissions were not separated, the tail of the GaAs emission peak (centered near 1.4 eV) is clear in the low energy signal of the MoS_2/n-GaAs sample data.

3.5.4.2 Interference effects

To evaluate the magnitude of cavity effects on the reflectivity of our samples, we performed transfer matrix calculations of the reflectivity for our samples and find that no large changes should be expected. Figure 24 shows the reflectivity of a MoS_2/hBN/GaAs stack as a function of the hBN thickness, for the laser excitation wavelength. At the thickness determined by atomic force microscopy of the hBN layer on our samples, t_{hBN} = (66 ± 5) nm, the reflectivity of the whole stack is just below 0.2, as compared to 0.43 for a sample without hBN. Thus, the excitation laser absorption does not change by more than 20%. A similar estimate for the interference effects at the luminescence wavelength indicates a destructive interference with the addition of the hBN layer. Therefore, cavity effects do not explain the large change in PL intensity between the control samples and MoS_2/GaAs.

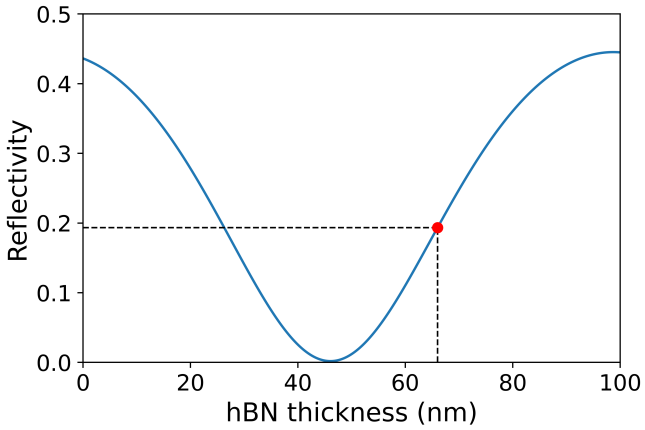

Figure 24 – Interference effect on the reflectivity of a MoS_2/hBN/GaAs stack as a function of the hBN thickness for the laser excitation wavelength of λ = 457 nm.

CHAPTER 4

Charge dynamics in the 2D/3D semiconductor heterostructure WSe_2/GaAs

Understanding the relaxation and recombination processes of excited states in two-dimensional (2D)/three-dimensional (3D) semiconductor heterojunctions is essential for developing efficient optical and (opto)electronic devices which integrate new 2D materials with more conventional 3D ones. In this work, we unveil the carrier dynamics and charge transfer in a monolayer of WSe_2 on a GaAs substrate. We use time-resolved differential reflectivity to study the charge relaxation processes involved in the junction and how it changes when compared to an electrically decoupled heterostructure, WSe_2/hBN/GaAs. We observe that the monolayer in direct contact with the GaAs substrate presents longer optically-excited carrier lifetimes (3.5 ns) when compared with the hBN-isolated region (1 ns), consistent with a strong reduction of radiative decay and a fast charge transfer of a single polarity. Through low-temperature measurements, we find evidence of a type-II band alignment for this heterostructure with an exciton dissociation that accumulates electrons in the GaAs and holes in the WSe_2. The type-II band alignment and fast photo-excited carrier dissociation shown here indicate that WSe_2/GaAs are promising junctions for new photovoltaic and other optoelectronic devices, making use of the best properties of new (2D) and conventional (3D) semiconductors.

4.1 Introduction

Transition metal dichalcogenides (TMDs) have received a lot of attention because of their atomically-thin thickness and interesting optical and electronic properties [2–4]. Their thickness confines the charges in the plane of the monolayer, resulting in strikingly different properties from their bulk counterpart [3, 106, 107]. Additionally, the stacking and/or twisting of consecutive monolayers into heterostructures has been shown to give rise to new physical phenomena and makes them strong candidates for the next generation of nanodevices [46, 108]. Their low dimensionality also makes them very sensitive to local changes, such as defects in the crystal lattice, strain, or impurities [109–111]. The interaction with the environment can also modify the properties of the two-dimensional (2D) semiconductor through, for instance, the interaction with gases or substrates with different electronic properties [44, 86]. The dielectric environment for the Coulomb interaction that gives place to excitonic phenomena in TMDs is particularly important and has been shown to be able to modulate its optical properties [43]. Therefore, we can use this as an advantage for developing new nanodevices such as gas sensors, photodetectors, and solar cells [82, 83, 112].

Gallium arsenide (GaAs) is one of the most studied semiconductors because of its applications in electronics as well as its very high electronic mobility, which allows for efficient gate-induced quantum confinement to one or two dimensions [113]. In particular, previous studies have demonstrated that the junction of this three-dimensional (3D) semiconductor with TMDs (i.e., 2D semiconductors) is a promising junction for optoelectronic devices [76, 79, 81–83]. In order to optimize and manipulate such systems for improving the design of new (opto)electronic devices, we need to obtain a high level of understanding of the electronic properties and time-evolution of their excited states. Nonetheless, the charge dynamics and band alignment between these materials are still largely unexplored.

In this work, we study the carrier dynamics in a monolayer of WSe_2 in contact with a GaAs substrate. We use an optical pump-probe approach, by measuring the time-resolved differential reflectivity (TRDR) of the junction and compare it with an electrically-isolated WSe_2, by adding a hexagonal boron nitride (hBN) layer (Fig 25.a). The WSe_2 monolayer in direct contact with the GaAs shows carriers that decay much slower with respect to the isolated WSe_2 at low temperatures. This can be understood through a type-II band alignment that dissociates the optically-excited excitons and creates an excess of electrons in the GaAs substrate and an excess of holes in the WSe_2 layer. Nonetheless, at room temperature we did not observe any important differences in the dynamics between the two regions, indicating a strong role of thermal effects on the relaxation process of photoexcited carriers.

4.2 Experimental Details

Our samples were fabricated by mechanical exfoliation of WSe_2 and hBN from their bulk crystals (supplied by HQ Graphene). The hBN flakes were exfoliated directly onto a commercial undoped (100) GaAs substrate (supplied by Wafer Technology) and the monolayers WSe_2 transferred on top by the viscoelastic stamp method [63]. We identified WSe_2 monolayers by optical contrast and photoluminescence in an optical microscope. The hBN thickness for the sample for which the results are shown here was around (21±2) nm, determined by atomic force microscopy. Time-resolved measurements were performed with a tunable Ti:Sapphire pulsed laser with a pulse width < 300 fs. We used a single-color (degenerate) pump-probe technique in a double modulation configuration as described in detail in our previous works [114,115]. All measurements were carried out at a temperature of 70 K unless otherwise indicated.

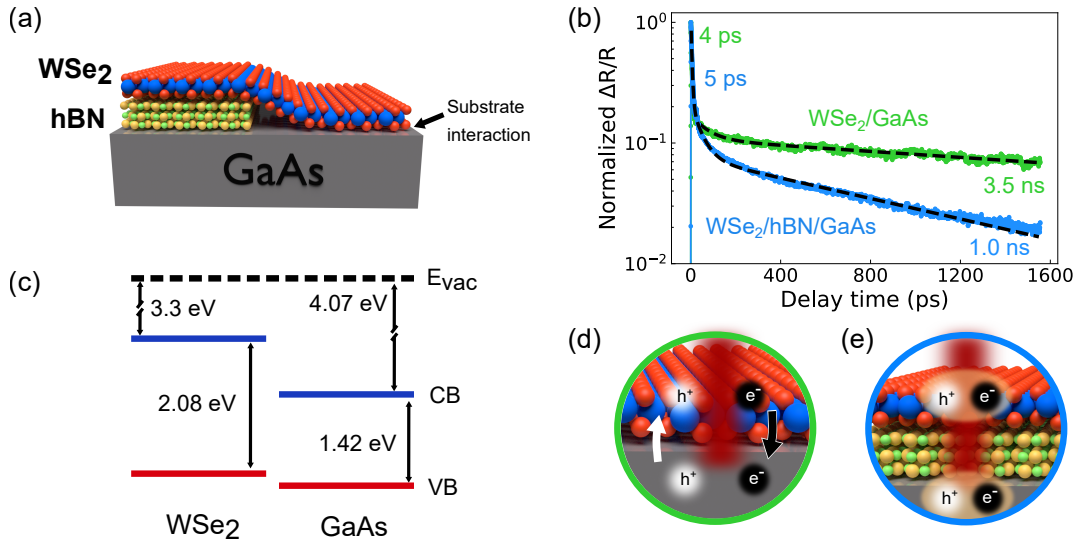

Figure 25 – (a) Schematics of our sample indicating the two regions of interest WSe_2/hBN/GaAs, and WSe_2/GaAs. (b) Normalized differential reflectivity of the two regions using laser energy for excitation in resonance with the WSe_2 exciton. (c) Estimated band alignment of the 2D/3D semiconductor heterojunction with E_{vac} the vacuum energy, CB the energy of the conduction band, and VB the valence band. Presented values consider T = 300 K. (d) Representation of the excitons generated in the WSe_2/GaAs region of the sample. Photo-excited excitons in the monolayer and in the substrate dissociate generating an excess of electrons in the GaAs and holes in the WSe_2. (e) In the WSe_2/hBN/GaAs region, the hBN prevents a charge transfer giving a more dominant role to radiative recombination processes under this configuration.

4.3 Results and Discussion

Figure 25.b shows the normalized TRDR of the two regions of the sample: the direct contact (WSe_2/GaAs - green) and the isolated (WSe_2/hBN/GaAs - blue) heterostructures when excited in resonance with the exciton transition of the WSe_2 layer as identified by TRDR spectroscopy (see below). Our results are well described by a three-processes exponential decay fit, $\Delta R/R = \sum R_{0i} e^{-t/\tau_i}$, with i from 1 to 3. Such multi-exponential decay has been reported by several works in literature, but the origin of the different decay processes has been attributed to various sources, depending on the specifics of the system. Overall, it has been observed that radiative processes occur in no longer than a few hundred picoseconds, while non-radiative phenomena may last longer [116–120].

From our results, we observe a longer-lived component determined to be (3.50 ± 0.04) ns in the region of direct contact compared with (1.00 ± 0.01) ns for the isolated one. To understand the origin of this difference, it is necessary to look into the bandgap alignment between the materials as it provides a picture of the possible charge dynamics in a junction. For instance, previous reports observed that a junction of semiconductors with a type-I band alignment can result in a reduction of the lifetime of the material with the larger band gap when placed in such a junction [121, 122]. This phenomenon can be associated with an energy transfer process where, for instance, the optically generated exciton in one material transfers energy generating an exciton in the other material [123]. On the other hand, a type-II band offset has been observed to enlarge the lifetime of the studied process [120, 124]. In those cases, the photo-generated excitons dissociate, resulting in the charge transfer, with electrons lying in one material and holes in the other. In light of this, our measurements point towards the existence of a type-II band offset in the WSe_2/GaAs heterojunction.

Simple band alignment estimations, as shown in Figure 25.c, further corroborate the proposed type-II band offset between monolayer WSe_2 and GaAs. Here, we consider an electron affinity of 3.3 eV and an electronic bandgap of 2.08 eV for WSe_2, as determined in a previous work [125]. While the bandgap E_g and electronic affinity χ of GaAs are well-established in the literature, for WSe_2 these values can change from one reference to another. The sensitivity of monolayer TMDs with the electric environment and other experimental and theoretical details can lead to a variation of these values, making it challenging for an accurate determination of these properties in a generic fashion. Nevertheless, even if differences in the exact values may arise, our work sets an upper boundary for a type-II band offset, where $\chi_{WSe_2} + E_{g(WSe_2)} < 5.49$ eV, as the valence band maximum of WSe_2 should remain at a higher energy than the maximum of the valence band of GaAs.

This type-II band alignment implies a dissociation of photo-excited carriers with a charge transfer between the two materials. When the junction - monolayer and substrate - is

excited, electrons at the conduction band will accumulate in the GaAs substrate, while the holes in the valence band will accumulate in the WSe_2 monolayer (Figure 25.d). As a result, longer lifetimes of the excited states can be linked to larger role of non-radiative scattering processes and a lack of available states in the valence (conduction) band for electrons (holes) to relax radiatively. In contrast, when considering the case of a WSe_2 isolated by hBN, charge transfer is restrained, and as a result, radiative exciton recombination is again the faster pathway for the relaxation of carriers (see Figure 25.e) Therefore, our results point towards a photoexcited carrier transfer between GaAs and WSe_2.

In Figure 25b, we also observe a fast decay time (τ_1) of 4 ps for the WSe_2 in direct contact with GaAs and 5 ps for the isolated region. We attribute this fast process in part to a stimulated emission, related to our single-color pump-probe excitation, as well as to exciton recombination out of thermal equilibrium [116–118, 126]. Despite the resolution of our measurements, we cannot associate the small difference in the relaxation times as arising exclusively from the interaction with the substrate, as stress or defects in the monolayer can modify the charge dynamics within the observed difference. Finally, we observed an intermediate decay time (τ_2) of 90 ps for the monolayer in direct contact and 50 ps in the isolated region, consistent with previous measurements of trion recombination lifetime [117, 119]. We associate the difference in the relaxation times τ_2 with an increase in the density of one type of charge carrier in the WSe_2 that protects the trion from fast recombination. In particular, in our sample, two phenomena can give origin to this imbalance of carriers: the reduction of the Fermi level of the WSe_2 due to the formation of the joint-Fermi level of the heterojunction with the GaAs, and the dissociation and charge transfer from the photo-excited carriers [76]. Moreover, the interaction of the WSe_2 with the GaAs can increase the dielectric disorder, which can result in an increase of recombination centers, such as defects and localized states [43, 127].

In order to gain further insight into the properties of our 2D/3D semiconductor junction, we study the dependence of the dynamics with the excitation wavelength. Figure 26 shows the intensity of the TRDR signal as a function of the laser wavelength at 2, 10, and 50 ps in the two regions of our system, direct contact and hBN separated. We observe that optical resonance is different for the two regions: 705 nm for WSe_2/GaAs and 708 nm for the WSe_2/hBN/GaAs region, indicating a blue-shift on the signal of the WSe_2 exciton in direct contact with the GaAs. We associate this effect with a combination of the interaction of the WSe_2 with a different dielectric environment and a possible effect of strain induced by the transfer onto GaAs, which should be reduced in the hBN region due to its higher smoothness and lack of dangling bonds. We also observed that the transient reflectivity of the WSe_2 in contact with the GaAs is smaller, almost half, at the wavelengths of resonance of the free exciton in WSe_2 when compared to the intensity of the hBN isolated region, indicating a higher absorption of the TMD in direct contact. This response can be related to the change of the Fermi level due to the formation of

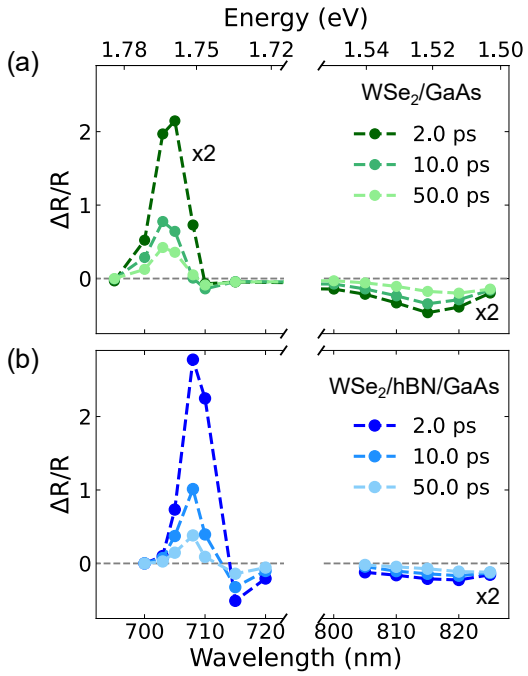

Figure 26 – (a) TRDR intensity as a function of the excitation and probing wavelengths at 2 ps, 10 ps, and 50 ps pump-probe delay time in $WSe_2/GaAs$ and (b) $WSe_2/hBN/GaAs$. For easier comparison the intensity values are presented as twice their real value in (a) and in the large wavelength region in (b).

the heterojunction, which reduces the electron density in the TMD. Moreover, the charge transfer at the junction allows for the presence of free states in the WSe_2 conduction band, which can be accessed by the photo-excited electrons, thereby enhancing the absorption of the region. In contrast, in the hBN-isolated area, stimulated emission and photobleaching will play an important role in reducing the absorption of the flake and increasing the reflectivity. For the wavelengths in the resonance with the free excitons in GaAs (800 nm - 830 nm), we observe a higher, negative, reflectivity in the sample in direct contact when compared to the isolated one. This observation is consistent with an increment of the photoinduced absorption of GaAs, produced by the larger density of electrons in the substrate resulting from a shift of the bands in the heterojunction.

By fitting the TRDR of the measurements for different wavelengths, we extract the energy-dependence of the decay lifetimes of the two regions of interest, which are presented in Figure 27. We did not observe any clear trend with the wavelength for the fast decay (τ_1) other than a slightly faster decay in the sample in direct contact as described previously. On the other hand, the results for the second decay time (τ_2) present a clearer trend, revealing one maximum lifetime at 705 nm for the TMD in direct contact with the GaAs substrate and at 708 nm in the isolated region, which matches with the resonances of WSe_2 exciton recombination of each area. Furthermore, we observe another maximum, and the highest τ_2 value, when exciting with a wavelength of 715 nm, which is related to the signal

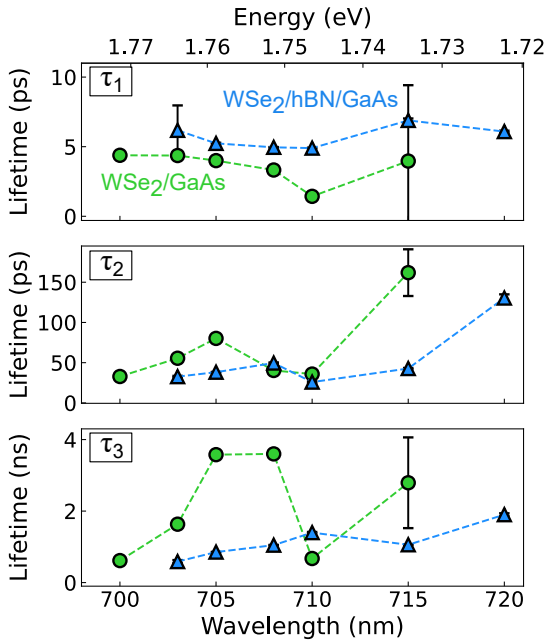

Figure 27 – Lifetimes of the TRDR signals as a function of the wavelength extracted from the three exponential decay processes described in the main text. When not shown, the error bars, obtained by the fit, are smaller than the point size.

coming from the negative, less intense, differential reflectivity in Figure 26.b. Data points for 720 nm in the direct contact region were discarded as the signal-to-noise ratio was too low to allow fitting. Although negative signals are commonly associated with photoinduced absorption, it has also been observed that in TMDs, bandgap renormalization plays an important role in this effect [128]. Therefore, we associate the different lifetimes obtained at this wavelength with the different origins of the relaxation path involved. Lastly, the obtained long lifetimes (τ_3) make clear the longer-lived character of the photo-excitated carriers in the TMD in direct contact with the GaAs, close to the resonance.

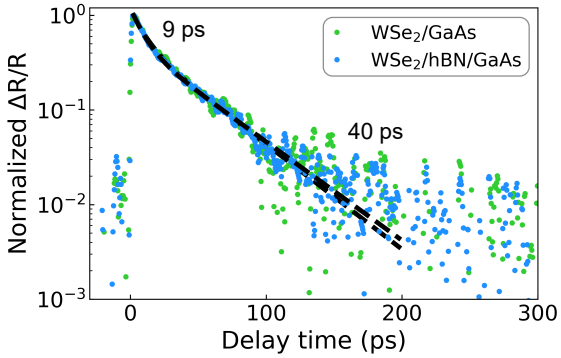

Figure 28 – Normalized TRDR for the $WSe_2/GaAs$ (green) and $WSe_2/hBN/GaAs$ (blue) regions at room temperature. The laser was tuned to be resonant with the WSe_2 exciton, at $\lambda = 740$ nm.

To determine the role of thermal effects, we measured the TRDR at room tempera-

ture (Figure 28), in the two regions of interest, exciting at the WSe_2 exciton resonance, $\lambda = 740$ nm. Our results show an overall shorter lifetime of the generated excitations when compared with the measurements at low temperature. We observe a similar behavior for both regions of the sample with just two clear decay processes: a fast decay of 9 ps and a slower decay of around 40 ps. If compared with our previous analysis at low temperature, we obtain a longer decay time τ_1, a shorter decay time τ_2, and the total absence of the presence of τ_3 decay process at room temperature. These findings are in agreement with earlier studies reporting longer decay times τ_1 of monolayer WSe_2 when increasing temperature [116, 129]. One possible explanation for this phenomenon is the important role of dark states in tungsten-based TMD monolayers which are observed for instance in the enhancement of the photoluminescence when increasing the temperature [130]. In our experiments at low temperature, the excitation in resonance with low laser power results in a reduced source for the electrons in dark states to transit into bright states. At high temperatures, electron-phonon interactions mediate the transition and cause an increase in the population and lifetimes of the two fastest processes in both regions of the sample. At the same time, this relaxation path, as well as other intralayer processes, become preferred over the charge transfer to the substrate, effectively eliminating the long-lived component τ_3 of the dynamics observed at low temperatures. Another possible relaxation channel is a change in the band alignment with the temperature. In this case, the small difference in the valence band maximum considered in Figure 29c could be enough for them to switch positions with the change in the temperature. Under this hypothesis, $WSe_2/GaAs$ would be type-I band offset at room temperature and switch to a type-II band alignment when reducing the temperature.

4.4 Conclusions

Our observation of a type-II band alignment and charge transfer between the prototypical 2D/3D semiconductors, WSe_2 and GaAs, indicates the promise of using such junctions in future optical and optoelectronic devices [79, 81–83]. The long-lived (3.5 ns) opto-excited carriers observed here should allow for a long enough time for these carriers to be transported away from the junction region, and used in photovoltaic devices. Additionally, a long decay time is a crucial element for lasers. Therefore, the combination of a long carrier lifetime with the unique spintronic properties of both WSe_2 and GaAs such as long spin lifetimes and electric control over the spin information [131–134], makes these junctions particularly appealing for lasers which make use of the spin degree-of-freedom, i.e. spin lasers [135], which have been shown to be able to operate at much higher modulation frequencies than conventional lasers [136]. We envision that such junctions, as the one shown here, using novel 2D semiconductors in combination with well-established and

industrially-proved 3D systems, can lead to an easier uptake of 2D materials in industrial settings, leading to new device architectures.

Acknowledgments

We thank J. G. Holstein, H. de Vries, F. van der Velde, H. Adema, and A. Joshua for their technical support. This work was supported by the Dutch Research Council (NWO — STU.019.014), the Zernike Institute for Advanced Materials, and the Brazilian funding agencies CNPq, FAPEMIG and the Coordenação de Aperfeiçoamento de Pessoal de Nível Superior - Brasil (CAPES) - Project code 88887.476316/2020-00. Sample fabrication was performed using NanoLabNL facilities.

CHAPTER 5

Magnetic field control of light-induced spin accumulation in monolayer $MoSe_2$

Semiconductor transition metal dichalcogenides (TMDs) have equivalent dynamics for their two spin/valley species. This arises from their energy-degenerated spin states, connected via time-reversal symmetry. When an out-of-plane magnetic field is applied, time-reversal symmetry is broken and the energies of the spin-polarized bands shift, resulting in different bandgaps and dynamics in the K_+ and K_- valleys. Here, we use time-resolved Kerr rotation to study the magnetic field dependence of the spin dynamics in monolayer $MoSe_2$. We show that the magnetic field can control the light-induced spin accumulation of the two valley states, with a small effect on the recombination lifetimes. We unveil that the magnetic field-dependent spin accumulation is in agreement with hole spin dynamics at the longer timescales, indicating that the electron spins have faster relaxation rates. We propose a rate equation model that suggests that lifting the energy-degeneracy of the valleys induces an ultrafast spin-flip toward the stabilization of the valley with the higher valence band energy. Our results provide an experimental insight into the ultrafast charge and spin dynamics in TMDs and a way to control it, which will be useful for the development of new spintronic and valleytronic applications.

Chapter published in 2D Matterials **10**, 035013 (2023) [115].

5.1 Introduction

Atomically-thin transition metal dichalcogenides (TMDs) offer the possibility to optically address the spin and valley degrees-of-freedom of charge carriers. Through circularly polarized light, σ_+ or σ_-, one can excite electron-hole pairs at opposite points at the edges of the Brillouin zone, known as K_+ and K_- valleys [13, 14, 137]. The high spin-orbit coupling in these materials further causes a spin splitting of the levels, connecting the spin and valley degrees-of-freedom and their dynamics. For this reason, TMDs are very attractive for (opto)valleytronic and (opto)spintronic applications [3, 20, 21, 138, 139]. One of the main bottlenecks for such applications is the control of these degrees-of-freedom. Magnetic fields have been shown to strongly affect the valley polarization. This has been demonstrated by photoluminescence (PL) measurements of TMD monolayers under high out-of-plane magnetic fields, showing a linear shift of the emission peaks reflecting the reduction of the band gap for one valley and the increase of the other [29–33]. This effect became known as the valley-Zeeman effect. These experiments extract an exciton and trion g-factor of ~ -4, which is in agreement with theoretical expectations [37, 140, 141]. Different works have reported the dynamics of electrons, excitons, and trions by performing time-resolved photoluminescence (TRPL) [142–144], time-resolved differential reflectivity (TRDR) [145–147], and time-resolved Kerr rotation (TRKR) [57–59, 114, 148, 149], with most works focusing on either zero or in-plane external magnetic fields. More recently, Zhang et al. [150] showed the effect of out-of-plane magnetic fields on polarized TRPL, but without any clear difference between the results obtained at different circularly polarized excitation and high magnetic fields. Nonetheless, PL is solely sensitive to the valley polarization and radiative decay of excitons and trions. Therefore, PL is insensitive to light-induced spin polarization of resident carriers which can sustain the spin information over much longer times. The understanding of the decay processes and possibilities of control of resident carriers are of huge importance for the engineering of a new generation of opto-spintronic devices [19, 21, 151, 152]. However, the use of an out-of-plane magnetic field to control the long-lived spin dynamics in monolayer TMDs – beyond the radiative recombination times – remains largely unexplored.

Here we show that the spin information of long-lived carriers in monolayer $MoSe_2$ can be effectively controlled via the valley-Zeeman effect. Using time-resolved magneto-optic Kerr effect, we show that magnetic fields can induce an ultrafast spin-valley scattering and enhancement of a light-induced spin accumulation with a preference for the valley with higher valence band energy. While we find that the spin scattering rates do not show a clear trend for the external magnetic field strength, the magneto-optical signal strength shows a clear linear behavior. Particularly, we observe a nearly field-independent long spin lifetime of $\sim$2 ns. The magnetic field dependence of the light-induced spin accumulation

we measure agrees with hole spin dynamics and resident carrier recombination at longer timescales, while we argue that electron spins may have faster relaxation rates. Our results are well described by a simple rate-equation model, which takes into consideration a field-dependent carrier recombination and intervalley scattering. Our model indicates that the magnetic field has a stronger effect on the hole transfer between valleys than in electrons, resulting in a spin imbalance with a larger population of carriers from the valley with the smaller bandgap. In this way, we demonstrate here that an applied magnetic field can be used to effectively control the optically-generated spin accumulation in TMDs.

5.2 Experimental Methods

Our samples were prepared by mechanical exfoliation of a bulk $MoSe_2$ crystal (HQ Graphene) onto a polydimethylsiloxane (PDMS - Gel Pack) and then transferred to a 285 nm SiO_2/Si substrate. The spin dynamics in our samples was measured by TRKR, which presents a higher sensitivity to spin-related phenomena, compared with TRPL or TRDR. We perform a single-color (degenerated) pump-probe technique in a dual-frequency modulation (see Appendix 5.5.1) using a similar experimental setup as described elsewhere [114]. When a high intensity circularly polarized ($\sigma_{\pm}$) laser pulse (pump) excites the monolayer, electrons of a single valley ($K_{\pm}$) are excited to the conduction band and can generate a spin imbalance. By shining a linearly polarized (probe) pulse at a certain time-delay after the pump pulse, the spin/valley imbalance is measured by a change on the polarization axis of the reflected beam, which is rotated by an angle θ_K (Fig. 29a). Finally, the time evolution of the spin imbalance in the sample is measured by changing the delay time (dt) between the pump and probe pulses. All measurements were performed at low-temperature T = 6 K.

5.3 Results and Discussion

Figure 29d shows the TRKR at zero magnetic field and how the sign of the Kerr rotation depends on which valley we are exciting: a positive (negative) Kerr rotation is observed upon shining σ_+ (σ_-) polarized pump pulses. This behavior is a fingerprint of the symmetry and spin selectivity of the two valleys of the TMD, when excited with circularly polarized light [57, 114, 148, 149, 153]. Two decay time constants are visible in our measurements, a faster ($\tau_1 \sim 1.5$ ps) and a longer one ($\tau_2 \sim 2$ ns) that goes beyond the measurement range.

We observe a drastic change on the TRKR dynamics upon an applied magnetic field. Figure 29c and e show the TRKR signal of our sample for an applied magnetic field

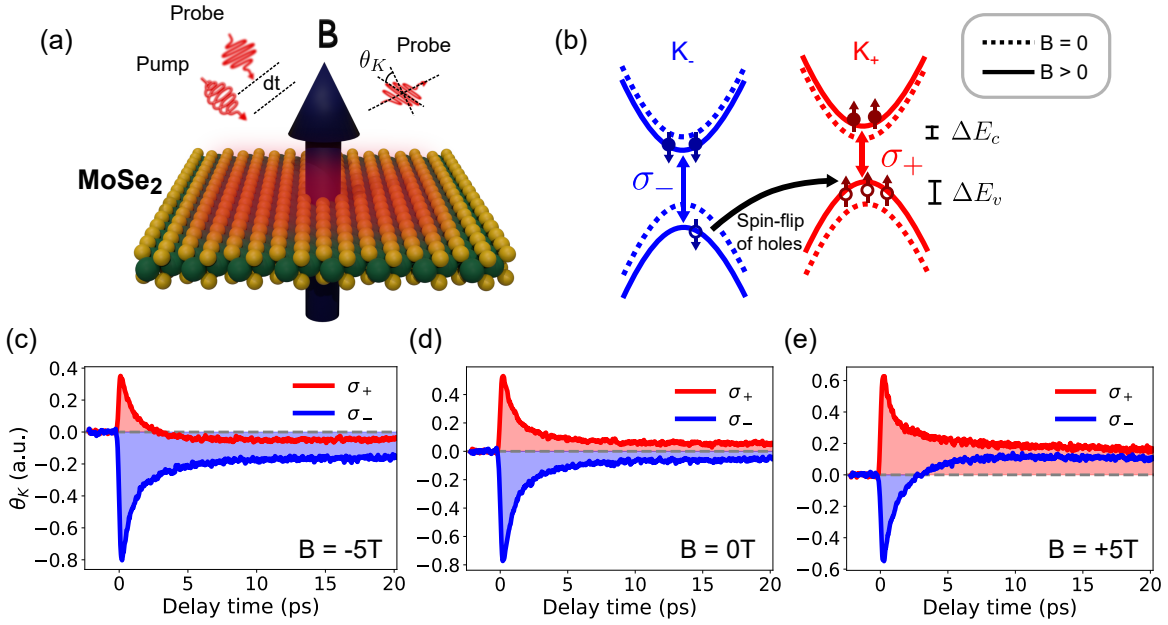

Figure 29 – (a) Schematics of the TRKR measurements with an external magnetic field. (b) Valley-Zeeman effect on the K_+ and K_- spin states of monolayer $MoSe_2$. Dashed lines indicates the zero magnetic field spin states while solid lines represent the magnetic field shifted states. The Valley-Zeeman effect results in larger energy shifting in the valence band ΔE_v than in the conduction band ΔE_c. (c) TRKR signal for σ_+ (red) and σ_- (blue) polarized pump, at different magnetic fields: B = -5 T, 0 T (d), +5 T (e), for λ= 755 nm and T = 6 K.

of -5 T and +5 T, respectively. Within the first 3 ps after excitation we observe a reversal of the TRKR signal for one pump polarization, while a stabilization for the other. This can be explained by an out-of-plane magnetic field lifting the valley degeneracy causing an opposite shift on the TMD bands of opposite valleys [30–33] (Fig 29b). Due to the different net angular momenta of the valence and conduction bands, the energy shifts for the conduction (ΔE_c) and valence bands (ΔE_v) are also different. The resulting effect is that the lowest energy state for holes lies within one valley, while for electrons lies in the other.

These observations reveal that our TRKR signal is dominated by hole relaxation. Upon populating the K_- valley through a σ_--polarized pump, we observe a reversal of the signal from negative to positive for positive magnetic fields. For this case, the electron ground state lies in the conduction band of the K_- valley, while the ground state of holes is located at the K_+ valley. The fact that we observe a positive TRKR signal after $\sim$ 3 ps, indicates a higher spin population of the K_+ valley, implying a fast intervalley scattering and that the spin accumulation measured in our experiments arises from the hole spin. When the direction of the magnetic field is reversed, similar behavior is observed but with an opposite TRKR signal.

The long decay times we observe do not show any clear dependence with the

magnetic field. The two decay time constants are obtained through a biexponential decay of the form $\theta_K = A_1 e^{-t/\tau_1} + A_2 e^{-t/\tau_2}$, where A_n are the Kerr rotation angles at a delay time $dt = 0$ and τ_n the decay times at the fast and slow decay processes $n = 1, 2$, respectively. This is done for measurements using both directions of pump polarization and various values of applied magnetic fields, from B = -5 T to +5 T. Figures 30a and 30b show the TRKR signals at B = -5 T to +5 T over a long dt range, up to 1.55 ns. The TRKR signals are still clearly measurable even at these long-time delays. The magnetic field dependence for τ_2 is shown in Figure 30c (see the Appendix 5.5.3 for τ_1). For zero, and also high magnetic fields, we find non-zero pump-induced TRKR signals. However, for $0 < |B| < 3$ T, the signal for one of the pump polarizations is within our experimental noise, and therefore only measurements for one pump polarization were used within this range. Nonetheless, we do not observe any striking features on the TRKR decay times for the whole range of magnetic fields studied, even though additional spin scattering channels are predicted to arise from the breaking of time-reversal symmetry [28]. This indicates that, while the intervalley scattering rate could be modified by the magnetic field, the main source of spin scattering remains unaffected for our samples.

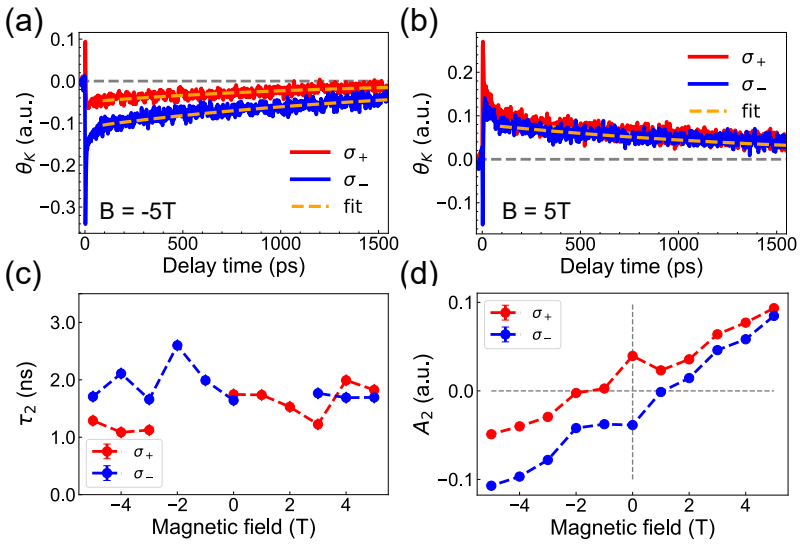

Figure 30 – (a) TRKR signal for σ_+ (red) and σ_- (blue) polarized pump, at B = -5 T (a) and +5 T (b) at long time scales. The orange dashed lines show the fit that extracts the slow relaxation times. (c) Extracted slow decay times (τ_2) and (d) amplitudes (A_2) at different magnetic fields for the two excitation polarizations.

The amplitude of our TRKR signals shows a clear linear behavior with the magnetic field, Fig. 30d. Strikingly, the slopes for the two pump polarizations are slightly different, resulting in a non-symmetric response with the magnetic field direction at long time delays. Previous measurement runs of the same sample also presented a linear trend with the magnetic field, with different slopes for each excitation polarization, see Appendix 5.5.6 for details. Although small experimental artifacts are not discarded, a phenomenological

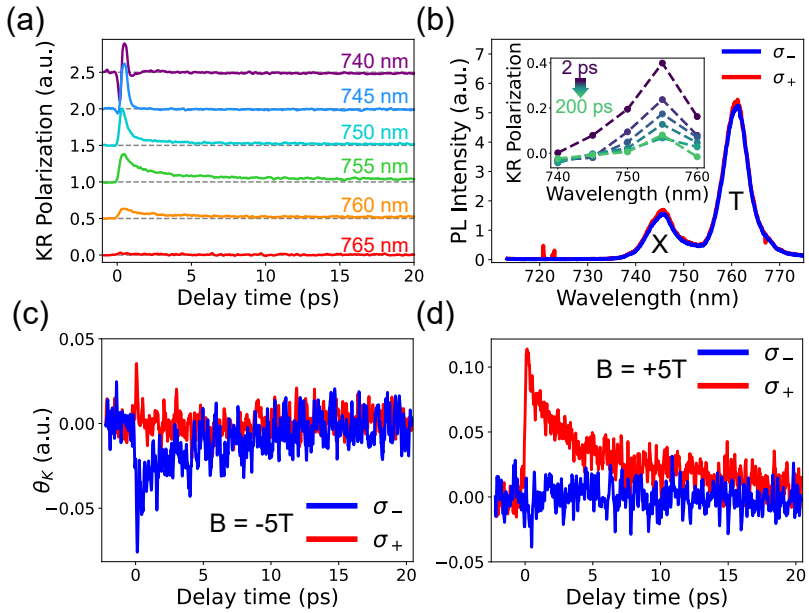

Figure 31 – (a) TRKR Polarization at different wavelengths and zero external magnetic fields. Measurements were shifted in the vertical axis for clarity. (b) Polarized photoluminescence spectra of our sample at B = 0 T. Inset: Intensity profile of the TRKR Polarization at different delay times: 2, 4, 6, 10, 100, and 200 ps. (c) TRKR for σ_+ (red) and σ_- (blue) polarized pump at λ = 765 nm for B = -5 T (c) and +5 T (d) at T = 6 K.

origin of these results would be inconsistent with a simple description involving solely a Zeeman energy shift of the energy states. We currently do not have a clear understanding of the origin of such an effect, which should be explored in more detail in later studies.

By studying the dependence of the TRKR signal on the excitation wavelength, we can probe the contribution of excitons and trions to the spin signal. To reduce spurious effects which are independent of the valley/spin polarization, here we use the polarization of the Kerr rotation, namely the difference of the TRKR measurements for the two polarizations of excitation $(\theta_K(\sigma_+) - \theta_K(\sigma_-))/2$ [114]. As expected, our signal is strongly modulated upon a change of the wavelength when going over the exciton and trion resonances (Fig. 31a). We observe that when exciting with $\lambda \leqslant 745$ nm, KR polarization decays in the first couple of picoseconds. On the other hand, when exciting at $\lambda \geqslant 750$ nm, the spin imbalance remains finite, within the time range of our measurements. The largest signal is seen at λ = 755 nm, see inset of Figure 31b. A comparison to photoluminescence measurements (Fig. 31b) reveals that our findings are consistent with short-lived signals coming from excitations at and below the wavelength of the exciton resonance (X), while the long-lived signals come from energies close to the peak of trion emission (T). Our observations are in agreement with previous reports in literature [57, 60, 142, 143] showing that trions dominate the spin signal in TMDs monolayers.

We observe an interesting effect arising from the magnetic field-induced reduction

of the bandgap for one valley with respect to the other. For high magnetic fields (B = ±5 T) and with excitation wavelengths with energies below the absorption edge (765 nm), we only observe a TRKR signal above our noise level for one pump polarization, Figure 31c and d. For the positive magnetic field, the bandgap of the K_+ valley is reduced and produces a spin accumulation when excited with σ_+. Nevertheless, as the bandgap at K_- is increased, the energy of the pumping photons is not enough to excite the electrons and generate any spin imbalance, resulting in no TRKR signal for σ_- excitation. A similar behavior is observed for negative magnetic fields, but with opposite spin accumulation in the K_- valley and no signal for σ_+ excitation. Additional measurements of wavelength dependence with the magnetic field can be found in Appendix 5.5.4.

To quantitatively describe the spin dynamics and to elucidate the relaxation processes behind our measurements, we use a rate-equation model similar to what has been proposed before [57], but including the effect of an external magnetic field. We consider three main carrier scattering processes: direct radiative recombination at the same valley, the spin-valley flip of electrons in the conduction band, and the spin-valley flip of holes in the valence band. The breaking of the energy degeneracy of the K_+ and K_- valleys is represented by different intervalley scattering rates. Therefore, considering the more general case, where conduction and valence band transfer rates, and also radiative recombination of both valleys, are different, we get to the set of equations

$$\frac{dn_+}{dt} = -\frac{n_+p_+}{\tau_+} - \frac{n_+}{\tau_{c+-}} + \frac{n_-}{\tau_{c-+}} \tag{5.1}$$

$$\frac{dn_-}{dt} = -\frac{n_-p_-}{\tau_-} - \frac{n_-}{\tau_{c-+}} + \frac{n_+}{\tau_{c+-}} \tag{5.2}$$

$$\frac{dp_+}{dt} = -\frac{n_+p_+}{\tau_+} - \frac{p_+}{\tau_{v+-}} + \frac{p_-}{\tau_{v-+}} \tag{5.3}$$

$$\frac{dp_-}{dt} = -\frac{n_-p_-}{\tau_-} - \frac{p_-}{\tau_{v-+}} + \frac{p_+}{\tau_{v+-}} \tag{5.4}$$

where n_i and p_i are the photo-excited populations at the K_i valley for electrons and holes, respectively. The first term at the right side of each equation represents the radiative recombination at a specific valley with recombination time $\tau_\pm$. The second term represents the population of carriers that is transferred to the opposite valley in the conduction or valence bands with an intervalley scattering time $\tau_{c,v_{\pm\mp}}$. Finally, the last term relates to the carrier transfer coming from the opposite valley (source term). As Kerr rotation measures the spin/valley imbalance of the system, we model our measurements as the difference between the valley populations $\theta_K = (n_+ + p_+) - (n_- + p_-)$. Here, it is worth pointing out that the listed relaxation times are not directly related to the decay times obtained by fitting the experimental data, e.g. Fig 2.c. Instead, our model intends to unveil the role of the different relaxation paths in those time scales observed experimentally.

The initial conditions allow us to consider the two types of excitation, for instance, $n_+(0) = N/2$, $p_+(0) = N/2$, $n_-(0) = 0$, and $p_-(0) = 0$ for σ_+ excitation, where $N/2$ is the number of excited carriers. In particular, to consider the effect of the resident carriers we consider the initial population of holes as $p_+(0) = N/2 + p_0/2 + \alpha B$ and $p_-(0) = p_0/2 - \alpha B$ for σ_+ excitation, where p_0 is the initial population of resident carriers equally distributed in both valleys. Also, we have included a linear dependence with the magnetic field (α), as a first approach, that is related to the change of the initial carrier population due to the valley-Zeeman shift of the bands (see Figure 32c).

The results obtained by solving our rate-equation system are in good agreement with the experimental measurements with and without magnetic fields. In Figure 32a we compare our experimental and theoretical results at zero magnetic field, where valley degeneracy is still present. We based our initial guesses and ranges of values on previous works of different scattering and relaxation lifetimes. We noticed that to properly reproduce our measurements, the radiative recombination rate could not be either the shorter nor the longer decay process, and instead, good results were achieved by using decay times (τ) of tens of picoseconds. The latter agrees with previous reports of the trion lifetime for $MoSe_2$ [59, 142, 143, 150]. Therefore, as our results point to a spin accumulation of holes at the long time range ($\tau_v \sim 2$ ns), the fast decay ($\tau_c = 1.8$ ps) is assigned to electron transfer at the conduction band. This is consistent with previous reports pointing out to the fast depolarization of electrons in the conduction band when compared to the holes, and even radiative recombination of trions [57, 154].

To simulate our results at high magnetic fields (Figure 32b) we introduce an asymmetry in the scattering times of the different considered processes (see Appendices 5.5.5 and 5.5.9 for details). Our model indicates that the main process responsible for the fast switch of spin polarization is a strong reduction of the hole inter-valley scattering through the valley with higher valence band energy. In the right panel of Figure 32b we show the result of the TRKR calculation just with the effect of an asymmetric scattering process at the valence band, by considering $\tau_{v_{-+}} = 5$ ps, three orders of magnitude smaller than $\tau_{v_{+-}} = 3$ ns. Meanwhile, the introduction of different scattering times for the electrons in the conduction band and different radiative recombination times at the two valleys can help to refine the result at the short lifetimes but they have no major impact on the total decay profile. Additionally, we considered the effect of the resident carriers that best fit our data with $p_0 = 0.1$ and $\alpha = 0.01$. We observed that the initial population of holes p_0 contributes to the longer decay time of the signal, while the magnetic dependence coefficient α generates an asymmetry in the absolute maximum/minimum values of the KR signal. Therefore, our results are consistent with an important contribution of the resident charge carriers to the long-lived component of the dynamics, which is in agreement with previous reports [57–60].

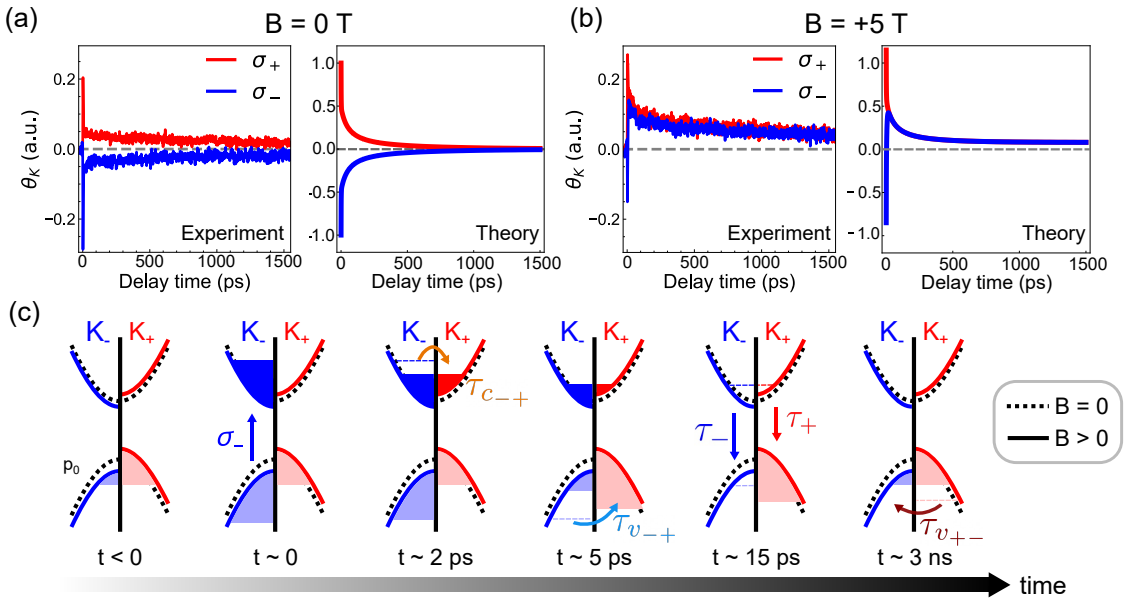

Figure 32 – (a) Experimental (left) and theoretical (right) results for B = 0 T with $\tau_+ = \tau_- = 15$ ps, $\tau_{c+-} = \tau_{c-+} = 1.8$ ps and $\tau_{v+-} = \tau_{v-+} = 1.5$ ns. (b) Experimental (left) and theoretical (right) results for B = +5 T with an asymmetric hole scattering time $\tau_{v-+} = 5$ ps, $\tau_{v+-} = 3$ ns, $\tau_+ = \tau_- = 15$ ps, $\tau_{c+-} = \tau_{c-+} = 1.8$ ps, $p_0 = 0.1$, $\alpha = 0.01$. (c) Representation of the dynamics of the spin population under positive magnetic fields: the ground state of the system with an initial hole population is photo-excited (σ_-) at the valley K_-. Later, electrons are scattered between valleys in the conduction band followed by the scattering of holes from K_- to K_+. Subsequently, excited states recombine radiatively. Finally, resident holes in K_+ reach thermal equilibrium with K_-. The represented transfer times indicate the dominant process at each panel.

In Figure 32c, we illustrate the obtained spin dynamics for positive magnetic field and an optical excitation of the K_- valley. We illustrate the six main steps in the dynamics of the system. Before excitation, there is an initial population of resident carriers (p_0), with a degree of asymmetry (α) between valleys induced by the magnetic field. The pump pulse σ_- excites the carriers at the K_- valley (t $\sim$ 0). In the first few picoseconds, the dominant relaxation process is the intervalley electron scattering τ_{c-+} equilibrating the electron population in the conduction band of both valleys. Afterwards, a fast and anisotropic hole scattering τ_{v-+} takes place (t $\sim$ 5 ps) scattering holes from the higher energy K_- valley to the lower energy K_+ valley. Radiative recombination takes place at a characteristic time $\tau_\pm$ (around 15 ps) resulting in a dominant K_+ spin/valley population. Finally, the long-lived component τ_{v+-} causes a relaxation of the remaining holes to the initial state in a time of up to 3 nanoseconds.

5.4 Conclusions

Our results show that optically-generated spins in TMDs can be very effectively controlled by magnetic fields, which is explained by a strong field-induced asymmetry on the intervalley scattering rates. We envision that the external magnetic field used in our experiments could be replaced by magnetic proximity to van der Waals magnets. These heterostructures have already shown to result on a significant control over valley polarization in photoluminescence measurements [19], and our work implies that a significant polarization of long-lived resident carriers can potentially be efficiently obtained and controlled via proximity effects, with lifetimes of several ns opposed to a few ps for excitons/trions. We believe that this will open new directions for opto-spintronic devices based on TMDs which do not depend on the stabilization of bound electron-hole pairs, but make use of the full potential of the long spin lifetimes offered by resident carriers in these materials.

Acknowledgments

We thank J. G. Holstein, H. de Vries, F. van der Velde, H. Adema, and A. Joshua for their technical support. This work was supported by the Dutch Research Council (NWO—STU.019.014), the Zernike Institute for Advanced Materials, and the Brazilian funding agencies CNPq, FAPEMIG and the Coordenação de Aperfeiçoamento de Pessoal de Nível Superior - Brasil (CAPES) - Project code 88887.476316/2020-00.

5.5 Appendices

5.5.1 Details on the experimental setup

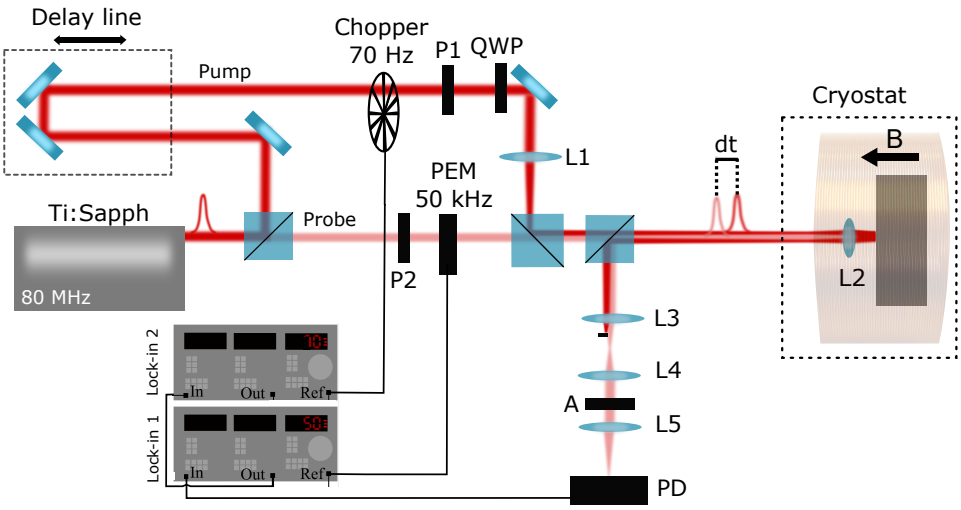

Figure 33 – Experimental setup used for our time-resolved measurements.

For measuring time-resolved data we used a single-color (degenerated) pump-probe technique in a double modulation configuration. Figure 33 pictures our experimental setup with the key elements represented on it. For excitation, we used a tunable Ti:sapphire laser (Mai Tai - Spectra Physics) with a repetition rate of 80 MHz and a pulse width < 300 fs. With a beam-splitter and a set of neutral density filters (not shown in Figure 33), we set the pump and probe beams to a 4:1 fluence ratio with a ~ 6 μJ/cm^2 probe fluence. The pump is set to circularly polarized light ($\sigma_{\pm}$) with a linear polarizer (P1) and a quarter wave plate (QWP) after passing through a chopper with a frequency of 70 Hz. For blocking the pump beam after the reflection on the sample we use the set of lenses L1, L3, and L4 that help focus the beam in a different place between L3 and L4, on its way back from the cryostat. The lens L1 also ensures a larger spot size for the pump beam at the sample, due to a different focal point. The probe beam is linearly polarized (P2) and its polarization is modulated by a photoelastic modulator (PEM) at a frequency $\Omega = 50$ kHz. The beam is detected on the way back from the sample by an amplified photodetector (PD) after passing through a linear polarizer (A), set cross-polarized with the probe for detecting the Kerr rotation signal.

The presence of the chopper in the pump path and the PEM in the probe path has the purpose of improving the signal-to-noise ratio, also known as the double modulation technique. The PEM is set with its fast axis at 45° to the axis of polarization of the incident beam that makes the polarization of the probe oscillate between circularly and linearly polarized with a frequency 2Ω. The difference in the modulation frequencies allows

us to separate the signal coming from each beam. With this configuration, the reflected signal is sent to one lock-in amplifier with the reference to the PEM oscillation frequency, which helps clean the signal coming from the probe beam. The output of the filtered signal is sent to a second lock-in amplifier that has its reference on the chopper frequency and helps to improve the signal from the probe which is affected by the pump. Using the Jones matrix formalism, it is possible to determine that the intensity of the signal at the second harmonic of the PEM oscillation frequency is related to the Kerr rotation as $I_{2\Omega} = \theta_K R J_2(\rho)\cos(2\Omega t)$ [114, 155], where θ_K the Kerr rotation, R is the average reflected intensity, J_2 the spherical Bessel function of the first kind and $\rho = 3.041$ is the retardation given by the PEM to optimize the signal. Therefore, the first lock-in amplifier is set to detect and amplify the second harmonic which is proportional to the Kerr rotation signal.

5.5.2 Photoluminescence at high magnetic fields

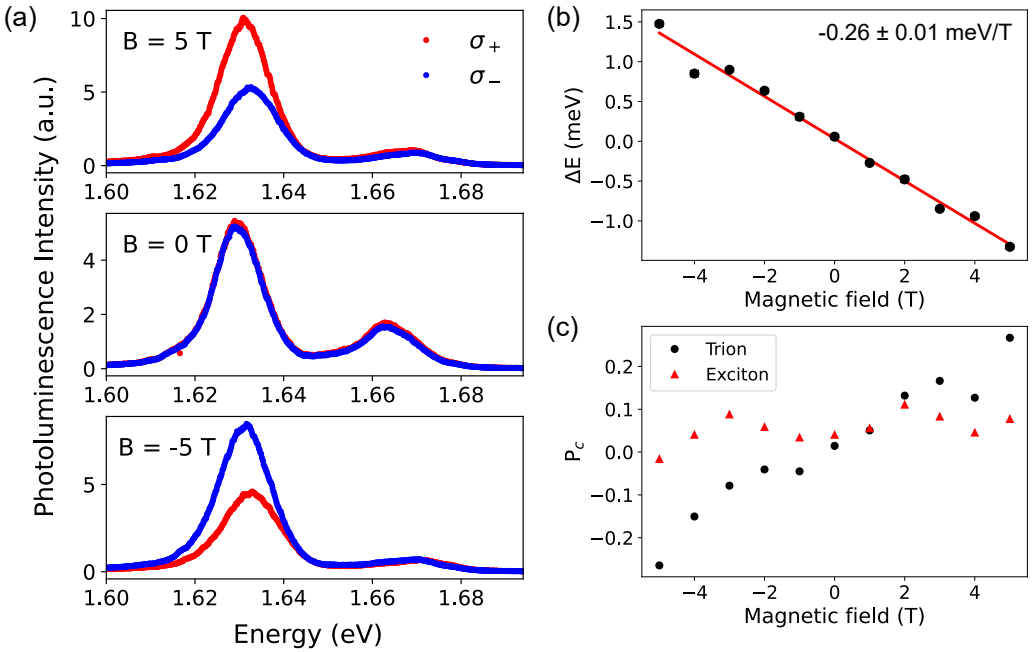

Figure 34 – Photoluminescence spectra of 1L $MoSe_2$ at different magnetic fields for the two polarization excitations. (b) Valley-Zeeman splitting for the trion peak, calculated as the difference of the energies $E_{\sigma_+} - E_{\sigma_-}$. (c) Degree of circular polarization (Pc) of excitons and trions at different magnetic fields.

Photoluminescence measurements were performed with $\lambda = 690$ nm laser diode with a power of 100 μW at a temperature of 6 K. For controlling the polarization, we set the fast axis of a quarter wave plate (QWP) aligned to the polarization of the excitation light. When the emitted light from the sample, $E_+\hat{\sigma}_+ + E_-\hat{\sigma}_-$, with $\hat{\sigma}_+$ the Jones matrix associated to the circularly polarized light, passes again through the waveplate, the fast axis is no longer aligned with the polarization of the light. The latter will decompose most

of the signal of the circularly polarized states at $\pm\pi/4$ with respect to the axis of the QWP. Therefore, by placing an analyzer (polarizer) at those angles, we can independently measure the intensity $|E_+|^2$ and $|E_-|^2$.

Figure 34a shows the photoluminescence spectra of our sample at different magnetic fields B = 0, ±5 T. Each spectrum was measured at the two polarizations, σ_+ (red) and σ_- (blue). The two characteristic peaks of $MoSe_2$ are observed: one coming from exciton recombination (1.664 eV) and the other from the emission of trions (1.630 eV). For analyzing the valley-Zeeman shifting we fitted the trion peak for both polarizations and plotted the difference of the peak centers E_{σ_+}-E_{σ_-} as a function of the magnetic field (Figure 34b). We obtained a linear behavior with a slope of (-0.26 ± 0.01) meV/T, indicating a g-factor of -4.5, which is in good agreement with previous reports in the literature [29, 32, 156]. Figure 34c shows the degree of circular polarization of the exciton and trion peaks as a function of the magnetic field calculated as the difference of the integrated intensity at the two different polarizations $P_c = (I_{\sigma_+} - I_{\sigma_-})/(I_{\sigma_+} + I_{\sigma_-})$.

5.5.3 Fast decay process in TRKR vs. Magnetic field

Figure 35 shows the fast decay times τ_1 and corresponding amplitudes A_1 obtained from the biexponential decay fits of the Kerr rotation angles measured at different magnetic fields.

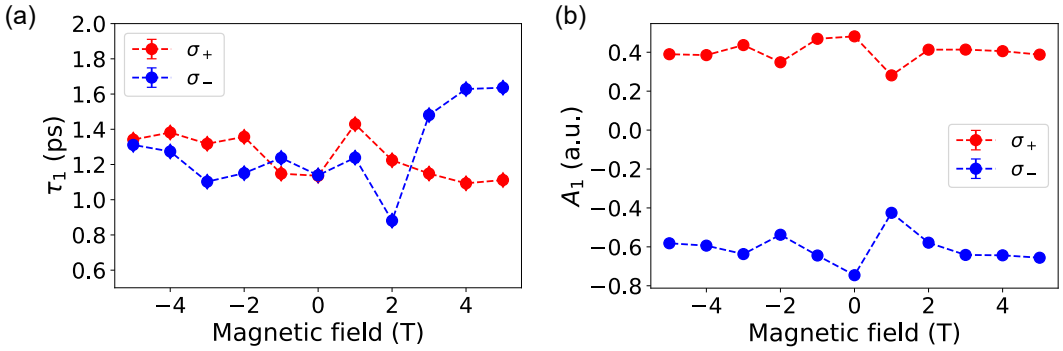

Figure 35 – Extracted fast decay times τ_1 and (b) amplitudes A_1 from the fits of TRKR presented in the main manuscript.

5.5.4 Spin dynamics: wavelength dependence

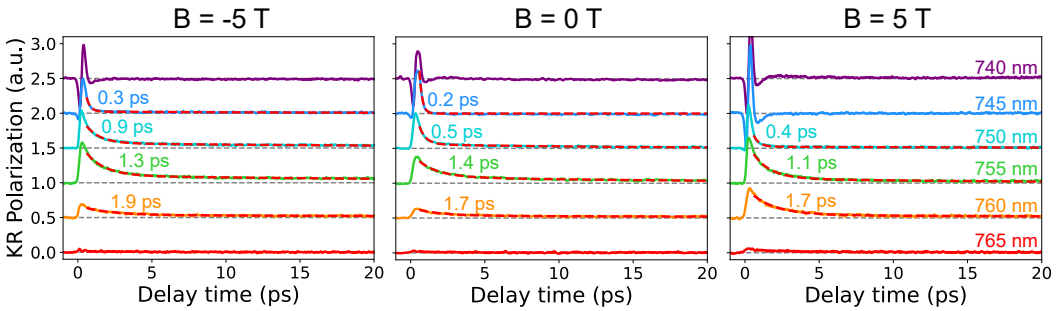

Figure 36 – Kerr rotation polarization of our sample at different wavelengths studied with an out-of-plane magnetic field B=±5 T and at B = 0 T. Extracted lifetimes are shown at each plot.

For keeping track of the wavelength dependence of the Kerr rotation with the magnetic field, we also measured the TRKR at the two polarizations ($\sigma_{\pm}$) for different wavelengths at B = 0 T, B = ±5 T. To reduce spurious effects and simplify the analysis, we calculate the Kerr rotation polarization defined as $(\theta_K(\sigma_+) - \theta_K(\sigma_-))/2$. The results are shown in Figure 36. In all the cases, we observe that the stronger and long-lived signals are associated with the wavelengths between λ = 755 nm and 760 nm. Therefore, the magnetic field does not induce clear changes in the KR signal close to exciton resonances nor change (significantly) the resonance close to the trion energy peak.

5.5.5 Rate equation Model -Different parameters

Figure 37a shows all the different decay paths considered in our model. When a magnetic field is applied, valley degeneracy breaking can affect the recombination and scattering times of excited spins at each valley. To start exploring the effect of such asymmetry, we first pursued the reproduction of our results at zero magnetic field, Figure 37b. In Figure 37(c-h) we present the TRKR calculated for different sets of parameters. As for zero magnetic field valley degeneracy is still present, equal scattering and recombination rates are considered for both valleys: $\tau_+ = \tau_- = \tau_r$, $\tau_{v_{+-}} = \tau_{v_{-+}} = \tau_v$, and $\tau_{c_{+-}} = \tau_{c_{-+}} = \tau_c$.

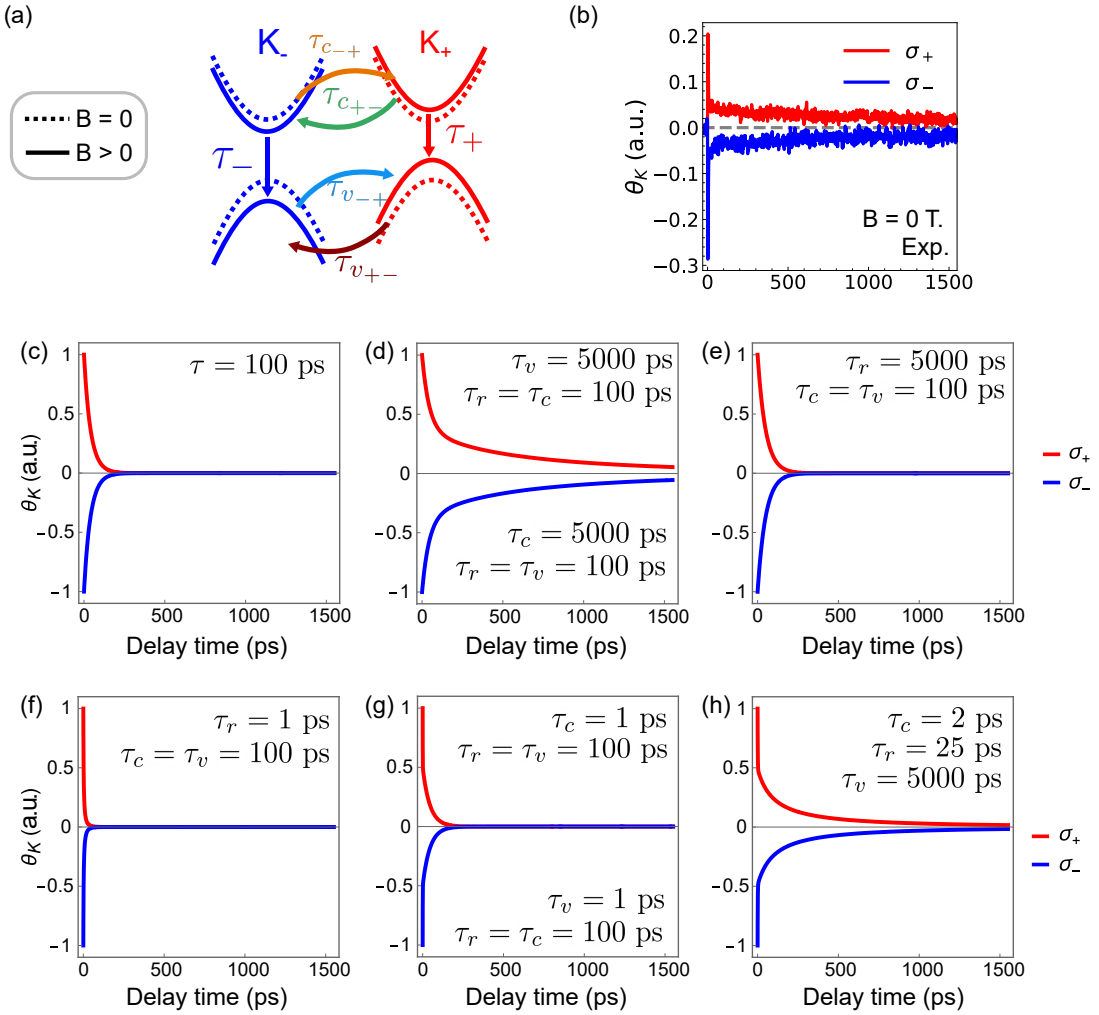

Figure 37 – (a) Representation of the valley-Zemman shifting and carrier transfer process of the bands at the vallleys $K_\pm$ under a positive magnetic field. (b) Experimental result of TRKR in $MoSe_2$ at zero magnetic field for the two pump polarizations $\sigma_\pm$ at T = 6 K. (c-h) Simulation of the TRKR using the model presented in the main text. The parameters for the calculation are presented in each figure. When two sets of parameters are presented on the same figure, it indicates that the same result is obtained for both cases.

With the obtained parameters at zero magnetic field (Figure 37h), we proceed

to study the effect of the magnetic field introducing the assymetry in the decay times. Figure 38 show the results of TRKR calculted with different parameters for reproducing our experimental results at B = ± 5 T.

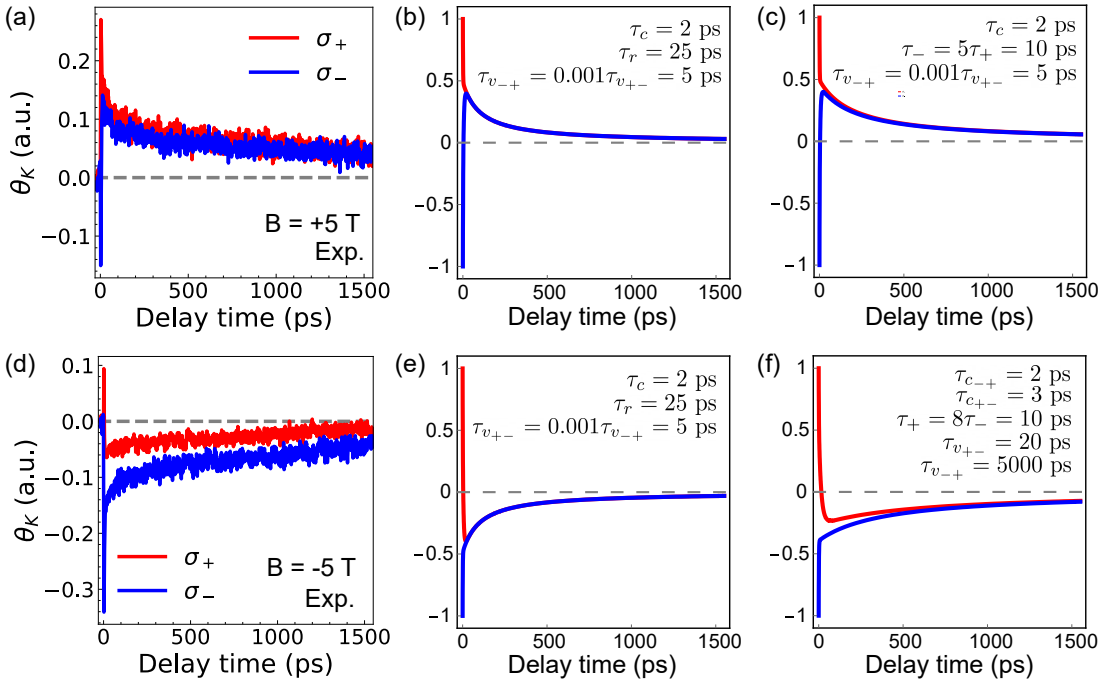

Figure 38 – (a) Experimental TRKR of $MoSe_2$ at B = 5 T. (b-c) Calculated TRKR for modeling (a). (d) Experimental result at B = -5 T. (e-f) Simulated TRKR for modeling the results shown in (d)

5.5.6 TRKR vs. B - Different set of measurements

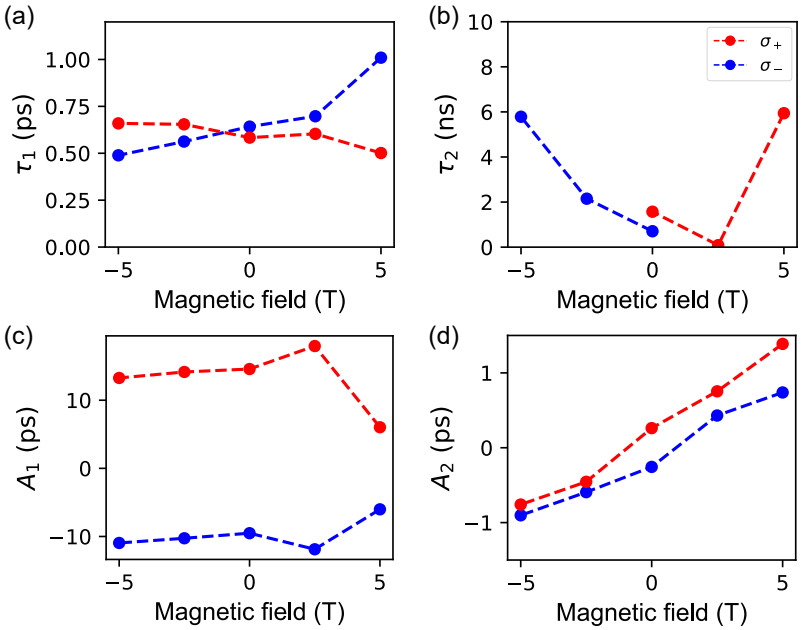

Figure 39 – (a-b) TRKR decay times and (c-d) amplitudes extracted at a different point of the sample, in a different cool down of the same sample, with a different alignment with $\lambda = 755$ nm, $F_{pump} = 100\ \mu J/cm^2$, $F_{probe} = 10\ \mu J/cm^2$, T = 6 K.

5.5.7 Further discussion on fitting the decay process

For fitting the spin dynamics in the main document we considered a simple approach of two exponential decay, as it is within the scope of our paper. For the fits, we use the data measured in two ranges with different acquisition parameters. One for short-time scale analysis up to 20 ps, acquired at 0.1 ps/s, and a long one for the slow decay process up to 1550 ps, with a velocity of acquisition of 3 ps/s. For each data set is possible to accurately fit either the fast or the slow decay process. Nevertheless, fits for intermediate decay times (tens of ps) can fail for some curves (see Figure 40a). Here, we present an alternative three-decay process fit ($A_1e^{-t/\tau_1} + A_2e^{-t/\tau_2} + A_3e^{-t/\tau_3}$) over the long-range data set that helps to elucidate the dynamics of the intermediate process and its effect on the results of the two-exponential decay.

Figure 40b presents the fits of the TRKR when exciting with polarization σ_+ at three different magnetic fields. In Figure 41 we present the extracted lifetimes and amplitudes of each decay process. We observe a consistent result for the fast and slow decay processes when compared with the data presented with the two-exponential decay case. For τ_2 we observed lifetimes of tens to a hundred picoseconds, which is consistent

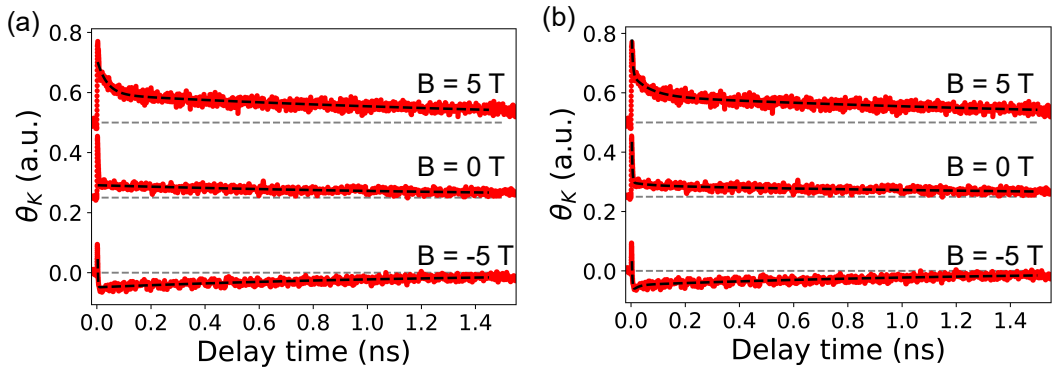

Figure 40 – (a) TRKR at different magnetic fields for a σ_+ excitation fitted with a bi-exponential decay and (b) a three-exponential decay (black dashed line).

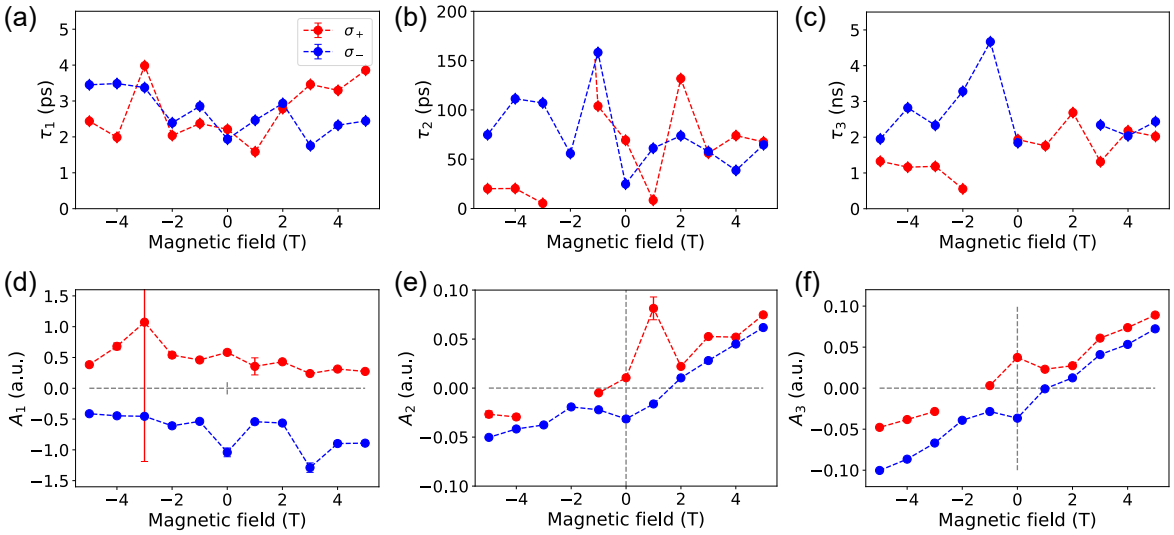

Figure 41 – Fitting parameters extracted from a three exponential decay fit.

with the trion recombination lifetime reported in the literature [57, 60, 142, 143]. Also, for the amplitude A_2, we observe a linear behavior with the magnetic field as observed for A_3.

5.5.8 TRKR modeling - Full magnetic field dependent data set

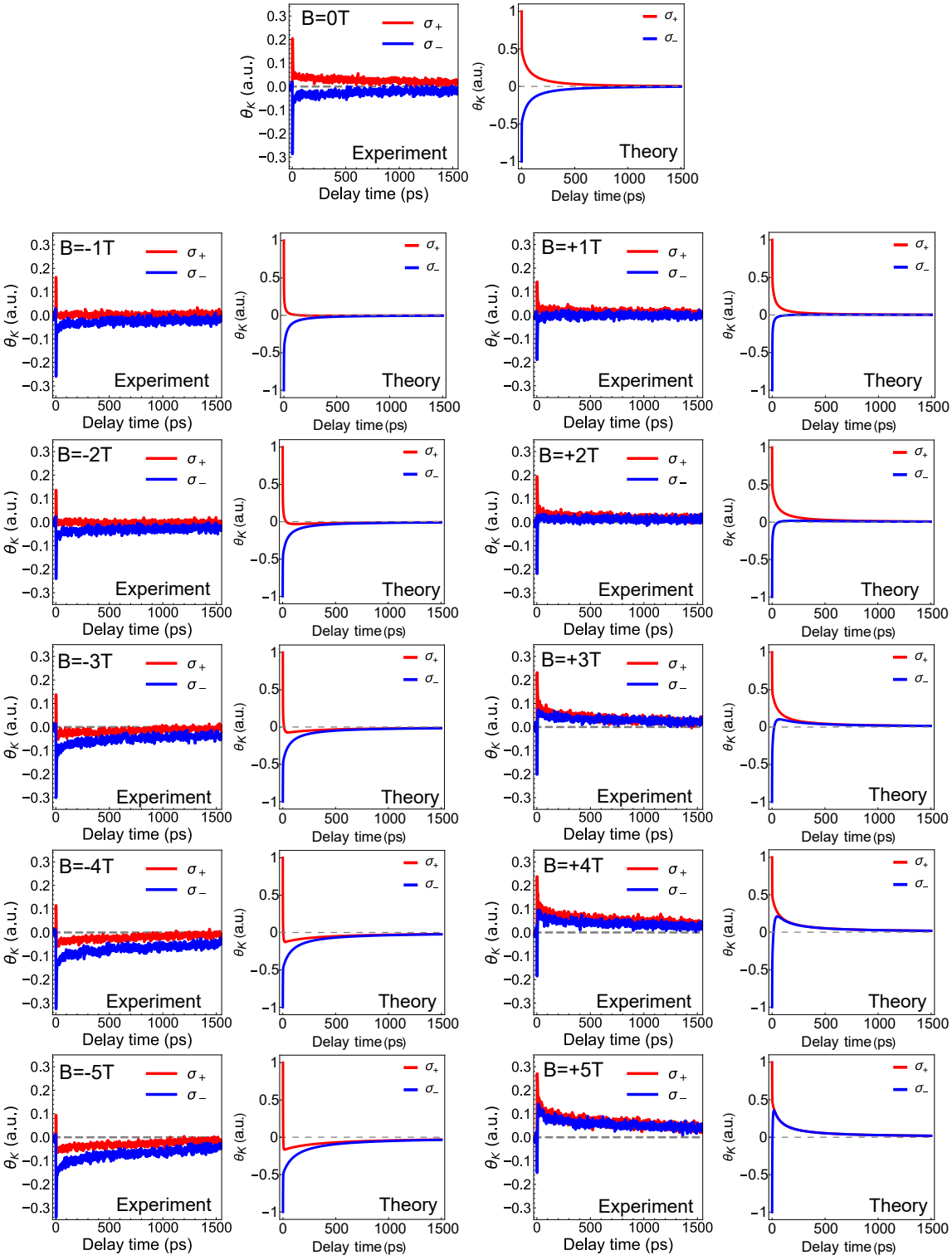

Figure 42 – Time-resolved Kerr rotation of the sample at different magnetic fields. Theoretical results using the model discussed in the main text are presented at the right side of the respective experimental measurement. Hole transfer and radiative lifetimes are presented in Figure 43, electron transfer lifetime was kept fix at 1.8 ps in all cases.

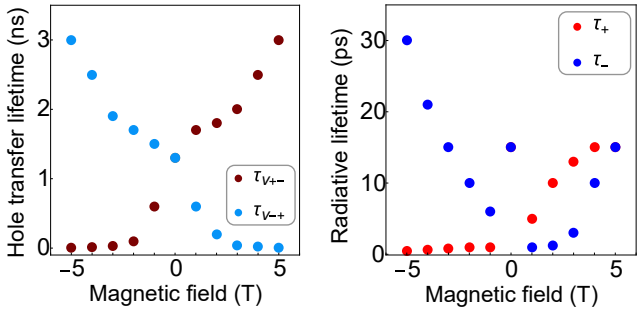

Figure 43 – Hole transfer and radiative lifetimes from the results presented in Figure 42.

5.5.9 TRKR - Effect of resident carriers at B = 5 T

.

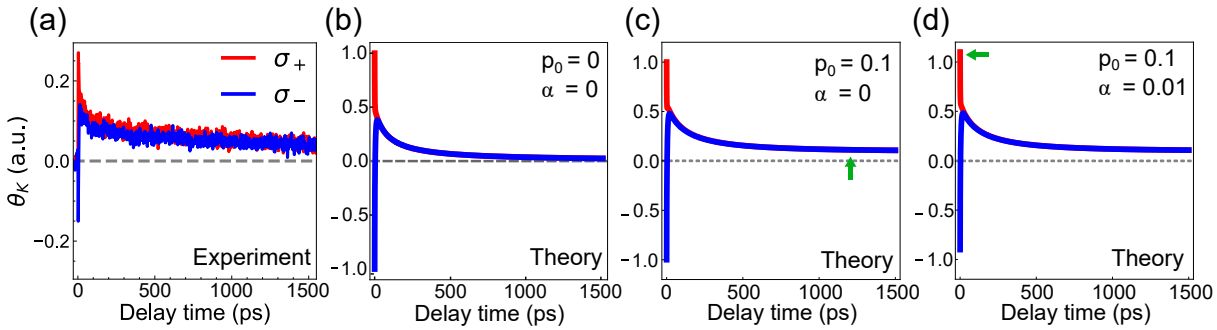

Figure 44 – (a) Experimental result of TRKR at B = 5 T. (b) Modeling of our measurements without considering resident carriers. (c) Result of an initial population of resident carriers p_0 contributing to the long-lived component. (d) Effect of the magnetic field-induced anisotropy to the initial population p_0, described in our initial conditions by the coefficient α. We observe an asymmetry in the maximum/minimum KR signal. The green arrows indicate the main effect of the parameters to the dynamics.

5.5.10 Time-Resolved Differential Reflectivity at B = 0 T

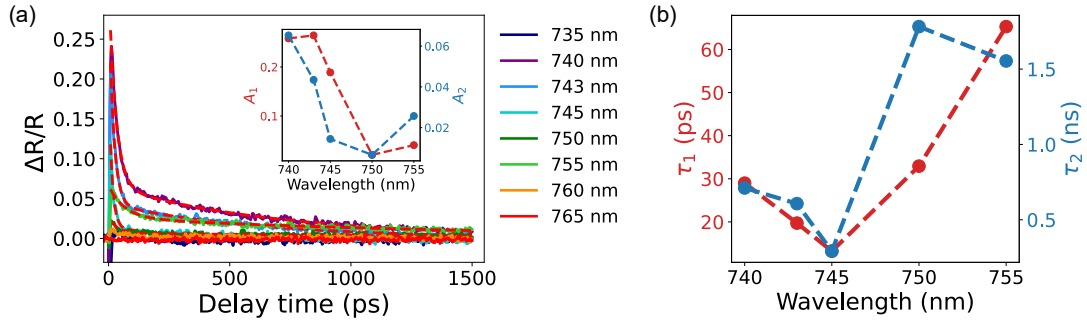

Figure 45 – (a) Time-resolved differential reflectivity studied at different wavelengths and their fits (red dashed lines). Inset: extracted amplitudes A_i and; (b) extracted lifetimes τ_i of the bi-exponential fit.

CHAPTER 6

General conclusions and outlook

In this thesis we discussed the effects of GaAs substrates on the charge dynamics of TMD monolayers by using optical techniques such as photoluminescence and time-resolved differential reflectivity. Furthermore, we study the changes in the spin dynamics of monolayer $MoSe_2$ under high magnetic fields by measuring time resolved Kerr rotation. Our findings in both cases are oriented towards the better understanding and control of the excitations of these systems that provide valuable results for further research for a connection with the applied outcome such as an optoelectronic device. Below, we present some of our main findings and their possible extension for further understanding and application of our results.

Effects of GaAs substrate

In chapters 3 and 4 we study the effects of GaAs substrates on the intrinsic properties of the studied monolayers. We were able to determine the band offset and charge dynamics of the junctions MoS_2/GaAs and WSe_2/GaAs. For the first case, our measurements were consistent with a type-I band alignment that results in the injection of the photo-excited excitons into the GaAs substrate. This configuration is of interest for increasing the range of light absorption of the intrinsic spectrum of GaAs and is of particular interest in the design of LEDs where electron-hole recombination is desired [157]. Nevertheless, we must say that due to the small difference observed in the band alignment, in particular in the conduction band offset, and the high sensitivity of the TMD monolayers, it is possible to consider a tunable band alignment with a transition to a type-II configuration [83].

The latter opens space to further studies on how to effectively control the desired band alignment by doping the TMD monolayer [158].

For the case of the WSe_2/GaAs junction, we determined a type-II band alignment that produces the dissociation of the optically generated excitons. After the dissociation, the free electrons are transferred toward the substrate and the holes to the monolayer. Our time-resolved measurements revealed that at low temperatures the carrier relaxation times can reach up to 3.5 nanoseconds, becoming of interest for further manipulation and design of optoelectronic devices. Nevertheless, our results at room temperature showed no difference in the time decay between the studied junction and an isolated monolayer. This could be associated to an important role of the thermal effects which reduce the time for the recombination and scattering of the carriers.

Finally, we envision that our results on junctions of TMD with GaAs can lead to the implementation of these junctions on optoelectronic devices but also in basic research in the study of confined systems and polaritonics [159, 160].

Effects of the magnetic field

Our results in chapter 5 showed how we can effectively control the spin population in a TMD monolayer using optical excitation and a high magnetic field. We investigate the spin imbalance in the spin imbalance generated on the sample at high magnetic fields via time-resolved measurements. We were able to experimentally observe the dynamics of the optically induced spin imbalance in the $MoSe_2$ monolayer, observing relaxation times of up to 2 nanoseconds. Using a rate equation modeling, we propose an asymmetric scattering of the carriers, resulting in a fast spin-flip (intervalley scattering) of holes as the main source of the spin imbalance. Also, we point to the resident carriers of the monolayer as playing an important role in this imbalance, a conclusion that is supported by our measurements and theoretical modeling. We expect that our work can inspire further studies such as the analysis of an electrostatic gating on the spin dynamics at high magnetic fields. Also, it suggests the study of the spin dynamics on samples that combine the TMD monolayers with layered ferromagnets that can modify the spin population of the TMD semiconductor through magnetic exchange, in a nonvolatile manner. Additional research, as the effect of magnetic doping, such as with vanadium, is of high interest for the increase in the g-factor, reducing the need for high magnetic fields to induce large spin imbalances [161, 162]. Overall, our work supports the vision of TMDs as materials with a large potential for implementation in optospintronic nanodevices [22, 163, 164].

Bibliography

[1] Novoselov, K. S., A. K. Geim, S V Morozov, D Jiang, Y Zhang, S V Dubonos, I V Grigorieva, A A Firsov, and K. S. Novoselov: *Electric Field Effect in Atomically Thin Carbon Films*. Science, 306:666–669, 2004. Citado na página 13.

[2] Mak, Kin Fai, Changgu Lee, James Hone, Jie Shan, and Tony F Heinz: *Atomically thin MoS_2: A new direct-gap semiconductor*. Physical Review Letters, 105(13):136805, 2010. Citado 4 vezes nas páginas 14, 27, 48, and 65.

[3] Mak, Kin Fai and Jie Shan: *Photonics and optoelectronics of 2D semiconductor transition metal dichalcogenides*. Nat. Photon., 10:216–226, April 2016, ISSN 17494893. Citado 3 vezes nas páginas 14, 65, and 74.

[4] Splendiani, Andrea, Liang Sun, Yuanbo Zhang, Tianshu Li, Jonghwan Kim, Chi Yung Chim, Giulia Galli, and Feng Wang: *Emerging photoluminescence in monolayer MoS_2*. Nano Letters, 10(4):1271–1275, 2010. Citado 3 vezes nas páginas 14, 48, and 65.

[5] Liu, Hsiang Lin, Chih Chiang Shen, Sheng Han Su, Chang Lung Hsu, Ming Yang Li, and Lain Jong Li: *Optical properties of monolayer transition metal dichalcogenides probed by spectroscopic ellipsometry*. Applied Physics Letters, 105(20), 2014. Citado na página 14.

[6] Mak, Kin Fai, Keliang He, Changgu Lee, Gwan Hyoung Lee, James Hone, Tony F Heinz, and Jie Shan: *Tightly bound trions in monolayer MoS_2*. Nature Materials, 12(3):207–211, 2013. Citado 3 vezes nas páginas 14, 48, and 51.

[7] Currie, M., A. T. Hanbicki, G. Kioseoglou, and B. T. Jonker: *Optical control of charged exciton states in tungsten disulfide*. Applied Physics Letters, 106(20), 2015. Citado na página 14.

[8] Xiao, Di, Gui Bin Liu, Wanxiang Feng, Xiaodong Xu, and Wang Yao: *Coupled spin and valley physics in monolayers of* mos_2 *and other group-vi dichalcogenides*. Phys. Rev. Lett., 108:196802, 2012. Citado 3 vezes nas páginas 14, 16, and 17.

[9] Cao, Ting, Gang Wang, Wenpeng Han, Huiqi Ye, Chuanrui Zhu, Junren Shi, Qian Niu, Pingheng Tan, Enge Wang, Baoli Liu, *et al.*: *Valley-selective circular dichroism of monolayer molybdenum disulphide*. Nature communications, 3(1):887, 2012. Citado 3 vezes nas páginas 14, 16, and 17.

[10] Kośmider, K., J. W. González, and J. Fernández-Rossier: *Large spin splitting in the conduction band of transition metal dichalcogenide monolayers*. Phys. Rev. B, 88:245436, 2013. Citado na página 14.

[11] Zhu, Z. Y., Y. C. Cheng, and U. Schwingenschlögl: *Giant spin-orbit-induced spin splitting in two-dimensional transition-metal dichalcogenide semiconductors*. Phys. Rev. B, 84:153402, 2011. Citado 2 vezes nas páginas 14 and 48.

[12] Mak, Kin Fai, Di Xiao, and Jie Shan: *Light–valley interactions in 2D semiconductors*. Nature Photonics, 12(8):451–460, 2018. Citado na página 15.

[13] Mak, Kin Fai, Keliang He, Jie Shan, and Tony F. Heinz: *Control of valley polarization in monolayer* MoS_2 *by optical helicity*. Nat. Nanotech., 7:494–498, 2012, ISSN 17483395. Citado 2 vezes nas páginas 15 and 74.

[14] Zeng, Hualing, Junfeng Dai, Wang Yao, Di Xiao, and Xiaodong Cui: *Valley polarization in* MoS_2 *monolayers by optical pumping*. Nat. Nanotech., 7:490–493, 2012, ISSN 17483395. Citado 2 vezes nas páginas 15 and 74.

[15] Li, Hai, Zongyou Yin, Qiyuan He, Hong Li, Xiao Huang, Gang Lu, Derrick Wen Hui Fam, Alfred Iing Yoong Tok, Qing Zhang, and Hua Zhang: *Fabrication of single- and multilayer MoS 2 film-based field-effect transistors for sensing NO at room temperature*. Small, 8(1):63–67, 2012. Citado na página 15.

[16] Lopez-Sanchez, Oriol, Dominik Lembke, Metin Kayci, Aleksandra Radenovic, and Andras Kis: *Ultrasensitive photodetectors based on monolayer* MoS_2. Nature Nanotechnology, 8(7):497–501, 2013. Citado na página 15.

[17] Tsai, Meng Lin, Sheng Han Su, Jan Kai Chang, Dung Sheng Tsai, Chang Hsiao Chen, Chih I. Wu, Lain Jong Li, Lih Juann Chen, and Jr Hau He: *Monolayer* MoS_2 *heterojunction solar cells*. ACS Nano, 8(8):8317–8322, 2014. Citado na página 15.

[18] Liu, Yunjie, Lanzhong Hao, Wei Gao, Zhipeng Wu, Yali Lin, Guixia Li, Wenyue Guo, Lianqing Yu, Huizhong Zeng, Jun Zhu, and Wanli Zhang: *Hydrogen gas sensing properties of MoS_2/Si heterojunction*. Sensors and Actuators, B: Chemical, 211:537–543, 2015. Citado na página 15.

[19] Seyler, Kyle L., Ding Zhong, Bevin Huang, Xiayu Linpeng, Nathan P. Wilson, Takashi Taniguchi, Kenji Watanabe, Wang Yao, Di Xiao, Michael A. McGuire, Kai Mei C. Fu, and Xiaodong Xu: *Valley manipulation by optically tuning the magnetic proximity effect in WSe_2/CrI_3 heterostructures*. Nano Letters, 18:3823–3828, June 2018, ISSN 15306992. Citado 3 vezes nas páginas 15, 74, and 82.

[20] Zhong, Ding, Kyle L. Seyler, Xiayu Linpeng, Ran Cheng, Nikhil Sivadas, Bevin Huang, Emma Schmidgall, Takashi Taniguchi, Kenji Watanabe, Michael A. McGuire, Wang Yao, Di Xiao, Kai Mei C. Fu, and Xiaodong Xu: *Van der Waals engineering of ferromagnetic semiconductor heterostructures for spin and valleytronics*. Sci. Adv., 3(5):e1603113, 2017. Citado 2 vezes nas páginas 15 and 74.

[21] Luo, Yunqiu Kelly, Jinsong Xu, Tiancong Zhu, Guanzhong Wu, Elizabeth J. McCormick, Wenbo Zhan, Mahesh R. Neupane, and Roland K. Kawakami: *Opto-valleytronic spin injection in monolayer MoS_2/few-layer graphene hybrid spin valves*. Nano Lett., 17:3877–3883, June 2017, ISSN 15306992. Citado 2 vezes nas páginas 15 and 74.

[22] Hidding, Jan and Marcos H D Guimarães: *Spin-orbit torques in transition metal dichalcogenide/ferromagnet heterostructures*. Frontiers in Materials, 7:594771, 2020. Citado 2 vezes nas páginas 15 and 95.

[23] Tonndorf, Philipp, Robert Schmidt, Robert Schneider, Johannes Kern, Michele Buscema, Gary A. Steele, Andres Castellanos-Gomez, Herre S. J. van der Zant, Steffen Michaelis de Vasconcellos, and Rudolf Bratschitsch: *Single-photon emission from localized excitons in an atomically thin semiconductor*. Optica, 2(4):347, 2015. Citado na página 15.

[24] Liu, Xiaoze, Tal Galfsky, Zheng Sun, Fengnian Xia, Erh chen Lin, Yi Hsien Lee, Stéphane Kéna-Cohen, and Vinod M Menon: *Strong light–matter coupling in two-dimensional atomic crystals*. Nature Photonics, 9(1):30–34, 2015. Citado na página 15.

[25] Glazov, Mikhail M, Eougenious L Ivchenko, Gang Wang, Thierry Amand, Xavier Marie, Bernhard Urbaszek, and BL Liu: *Spin and valley dynamics of excitons in transition metal dichalcogenide monolayers*. physica status solidi (b), 252(11):2349–2362, 2015. Citado na página 16.

[26] Zhang, Xiao Xiao, Yumeng You, Shu Yang Frank Zhao, and Tony F Heinz: *Experimental evidence for dark excitons in monolayer wse 2*. Physical review letters, 115(25):257403, 2015. Citado na página 16.

[27] Liu, Gui Bin, Wen Yu Shan, Yugui Yao, Wang Yao, and Di Xiao: *Three-band tight-binding model for monolayers of group-vib transition metal dichalcogenides*. Physical Review B, 88(8):085433, 2013. Citado na página 16.

[28] Gilardoni, Carmem M., Freddie Hendriks, Caspar H. van der Wal, and Marcos H. D. Guimarães: *Symmetry and control of spin-scattering processes in two-dimensional transition metal dichalcogenides*. Phys. Rev. B, 103:115410, March 2021. Citado 2 vezes nas páginas 16 and 77.

[29] Koperski, Maciej, Maciej R. Molas, Ashish Arora, Karol Nogajewski, Miroslav Bartos, Jan Wyzula, Diana Vaclavkova, Piotr Kossacki, and Marek Potemski: *Orbital, spin and valley contributions to Zeeman splitting of excitonic resonances in $MoSe_2$, WSe_2 and WS_2 monolayers*. 2D Mater., 6:015001, January 2019, ISSN 20531583. Citado 4 vezes nas páginas 16, 19, 74, and 85.

[30] Li, Yilei, Jonathan Ludwig, Tony Low, Alexey Chernikov, Xu Cui, Ghidewon Arefe, Young Duck Kim, Arend M. van der Zande, Albert Rigosi, Heather M. Hill, Suk Hyun Kim, James Hone, Zhiqiang Li, Dmitry Smirnov, and Tony F. Heinz: *Valley splitting and polarization by the Zeeman effect in monolayer $MoSe_2$*. Phys. Rev. Lett., 113:266804, December 2014. Citado 5 vezes nas páginas 16, 17, 19, 74, and 76.

[31] Aivazian, G., Zhirui Gong, Aaron M. Jones, Rui Lin Chu, J. Yan, D. G. Mandrus, Chuanwei Zhang, David Cobden, Wang Yao, and X. Xu: *Magnetic control of valley pseudospin in monolayer WSe_2*. Nat. Phys., 11:148–152, January 2015, ISSN 17452481. Citado 5 vezes nas páginas 16, 17, 19, 74, and 76.

[32] MacNeill, David, Colin Heikes, Kin Fai Mak, Zachary Anderson, Andor Kormányos, Viktor Zólyomi, Jiwoong Park, and Daniel C. Ralph: *Breaking of valley degeneracy by magnetic field in monolayer $MoSe_2$*. Phys. Rev. Lett., 114:037401, January 2015, ISSN 10797114. Citado 6 vezes nas páginas 16, 17, 19, 74, 76, and 85.

[33] Srivastava, Ajit, Meinrad Sidler, Adrien V. Allain, Dominik S. Lembke, Andras Kis, and A. Imamoğlu: *Valley Zeeman effect in elementary optical excitations of monolayer WSe_2*. Nat. Phys., 11:141–147, January 2015, ISSN 17452481. Citado 5 vezes nas páginas 16, 17, 19, 74, and 76.

[34] Bayer, M., S. N. Walck, T. L. Reinecke, and A. Forchel: *Exciton binding energies and diamagnetic shifts in semiconductor quantum wires and quantum dots*. Phys. Rev. B, 57:6584–6591, 1998. Citado na página 19.

[35] Walck, S. N. and T. L. Reinecke: *Exciton diamagnetic shift in semiconductor nanostructures*. Phys. Rev. B, 57:9088–9096, 1998. Citado na página 19.

[36] Lyons, Thomas P, Scott Dufferwiel, Matthew Brooks, Freddie Withers, T Taniguchi, Kenji Watanabe, KS Novoselov, Guido Burkard, and Alexander I Tartakovskii: *The valley Zeeman effect in inter-and intra-valley trions in monolayer WSe_2*. Nature communications, 10(1):2330, 2019. Citado na página 19.

[37] WoŹniak, Tomasz, Paulo E. Faria Junior, Gotthard Seifert, Andrey Chaves, and Jens Kunstmann: *Exciton g factors of van der Waals heterostructures from first-principles calculations*. Phys. Rev. B, 101:235408, June 2020. Citado 2 vezes nas páginas 19 and 74.

[38] Förste, Jonathan, Nikita V Tepliakov, Stanislav Yu Kruchinin, Jessica Lindlau, Victor Funk, Michael Förg, Kenji Watanabe, Takashi Taniguchi, Anvar S Baimuratov, and Alexander Högele: *Exciton g-factors in monolayer and bilayer WSe_2 from experiment and theory*. Nature Communications, 11(1):4539, 2020. Citado na página 19.

[39] Li, Qiang, Qionghua Zhou, Li Shi, Qian Chen, and Jinlan Wang: *Recent advances in oxidation and degradation mechanisms of ultrathin 2D materials under ambient conditions and their passivation strategies*. Journal of Materials Chemistry A, 7(9):4291–4312, 2019. Citado na página 20.

[40] Longo, Roberto C, Rafik Addou, Santosh KC, Ji Young Noh, Christopher M Smyth, Diego Barrera, Chenxi Zhang, Julia W P Hsu, Robert M Wallace, and Kyeongjae Cho: *Intrinsic air stability mechanisms of two-dimensional transition metal dichalcogenide surfaces: basal versus edge oxidation*. 2D Materials, 4(2):025050, 2017. Citado na página 20.

[41] Guo, Y, D Liu, and JJAPL Robertson: *Chalcogen vacancies in monolayer transition metal dichalcogenides and fermi level pinning at contacts*. Applied Physics Letters, 106(17):173106, 2015. Citado na página 20.

[42] Park, Jaeseo, Jihun Mun, Jae Soo Shin, and Sang Woo Kang: *Highly sensitive two-dimensional MoS_2 gas sensor decorated with pt nanoparticles*. Royal Society open science, 5(12):181462, 2018. Citado na página 20.

[43] Raja, Archana, Lutz Waldecker, Jonas Zipfel, Yeongsu Cho, Samuel Brem, Jonas D. Ziegler, Marvin Kulig, Takashi Taniguchi, Kenji Watanabe, Ermin Malic, Tony F. Heinz, Timothy C. Berkelbach, and Alexey Chernikov: *Dielectric disorder in two-dimensional materials*. Nat. Nanotechnol., 14:832–837, September 2019, ISSN 17483395. Citado 3 vezes nas páginas 20, 65, and 68.

[44] Sun, Yinghui, Rongming Wang, and Kai Liu: *Substrate induced changes in atomically thin 2-dimensional semiconductors: Fundamentals, engineering, and applications.* Applied Physics Reviews, 4(1):011301, 2017. Citado 3 vezes nas páginas 20, 48, and 65.

[45] Conley, Hiram J, Bin Wang, Jed I Ziegler, Richard F Haglund Jr, Sokrates T Pantelides, and Kirill I Bolotin: *Bandgap engineering of strained monolayer and bilayer MoS_2.* Nano letters, 13(8):3626–3630, 2013. Citado na página 20.

[46] Ciarrocchi, Alberto, Fedele Tagarelli, Ahmet Avsar, and Andras Kis: *Excitonic devices with van der Waals heterostructures: valleytronics meets twistronics.* Nature Reviews Materials, 7:449–464, June 2022, ISSN 20588437. Citado 2 vezes nas páginas 22 and 65.

[47] He, Feng, Yongjian Zhou, Zefang Ye, Sang Hyeok Cho, Jihoon Jeong, Xianghai Meng, and Yaguo Wang: *Moiré patterns in 2D materials: a review.* ACS nano, 15(4):5944–5958, 2021. Citado na página 22.

[48] Huang, Di, Junho Choi, Chih Kang Shih, and Xiaoqin Li: *Excitons in semiconductor moiré superlattices.* Nature Nanotechnology, 17(3):227–238, 2022. Citado na página 22.

[49] Trovatello, Chiara, Florian Katsch, Nicholas J Borys, Malte Selig, Kaiyuan Yao, Rocio Borrego-Varillas, Francesco Scotognella, Ilka Kriegel, Aiming Yan, Alex Zettl, *et al.*: *The ultrafast onset of exciton formation in 2D semiconductors.* Nature communications, 11(1):5277, 2020. Citado na página 22.

[50] Steinleitner, Philipp, Philipp Merkl, Philipp Nagler, Joshua Mornhinweg, Christian Schüller, Tobias Korn, Alexey Chernikov, and Rupert Huber: *Direct observation of ultrafast exciton formation in a monolayer of WSe_2.* Nano Letters, 17(3):1455–1460, 2017. Citado na página 22.

[51] Chen, Hailong, Xiewen Wen, Jing Zhang, Tianmin Wu, Yongji Gong, Xiang Zhang, Jiangtan Yuan, Chongyue Yi, Jun Lou, Pulickel M Ajayan, *et al.*: *Ultrafast formation of interlayer hot excitons in atomically thin MoS_2/WS_2 heterostructures.* Nature communications, 7(1):12512, 2016. Citado na página 22.

[52] Singh, Akshay, Galan Moody, Kha Tran, Marie E. Scott, Vincent Overbeck, Gunnar Berghäuser, John Schaibley, Edward J. Seifert, Dennis Pleskot, Nathaniel M. Gabor, Jiaqiang Yan, David G. Mandrus, Marten Richter, Ermin Malic, Xiaodong Xu, and Xiaoqin Li: *Trion formation dynamics in monolayer transition metal dichalcogenides.* Phys. Rev. B, 93:041401, 2016. Citado na página 22.

[53] Genco, Armando, Chiara Trovatello, Charalambos Louca, Kenji Watanabe, Takashi Taniguchi, Alexander I Tartakovskii, Giulio Cerullo, and Stefano Dal Conte: *Ultrafast exciton and trion dynamics in high-quality encapsulated MoS_2 monolayers*. physica status solidi (b), page 2200376, 2022. Citado na página 22.

[54] Christopher, Jason W, Bennett B Goldberg, and Anna K Swan: *Long tailed trions in monolayer MoS_2: Temperature dependent asymmetry and resulting red-shift of trion photoluminescence spectra*. Scientific reports, 7(1):14062, 2017. Citado na página 23.

[55] Sousa, Frederico B, Raül Perea-Causin, Sean Hartmann, Lucas Lafetá, Bárbara Rosa, Samuel Brem, Chirag Palekar, Stephan Reitzenstein, Achim Hartschuh, Ermin Malic, *et al.*: *Ultrafast hot electron–hole plasma photoluminescence in two-dimensional semiconductors*. Nanoscale, 2023. Citado na página 23.

[56] Ye, Jialiang, Tengfei Yan, Binghui Niu, Ying Li, and Xinhui Zhang: *Nonlinear dynamics of trions under strong optical excitation in monolayer $MoSe_2$*. Scientific reports, 8(1):2389, 2018. Citado na página 23.

[57] Hsu, Wei Ting, Yen Lun Chen, Chiang Hsiao Chen, Pang Shiuan Liu, Tuo Hung Hou, Lain Jong Li, and Wen Hao Chang: *Optically initialized robust valley-polarized holes in monolayer WSe_2*. Nat. Commun., 6:8963, November 2015, ISSN 20411723. Citado 7 vezes nas páginas 23, 74, 75, 78, 79, 80, and 90.

[58] Ersfeld, Manfred, Frank Volmer, Pedro Miguel M.C. De Melo, Robin De Winter, Maximilian Heithoff, Zeila Zanolli, Christoph Stampfer, Matthieu J. Verstraete, and Bernd Beschoten: *Spin states protected from intrinsic electron-phonon coupling reaching 100 ns lifetime at room temperature in $MoSe_2$*. Nano Lett., 19:4083–4090, June 2019, ISSN 15306992. Citado 3 vezes nas páginas 23, 74, and 80.

[59] Anghel, S., F. Passmann, C. Ruppert, A. D. Bristow, and M. Betz: *Coupled exciton-trion spin dynamics in a $MoSe_2$ monolayer*. 2D Mater., 5:045024, September 2018, ISSN 20531583. Citado 3 vezes nas páginas 23, 74, and 80.

[60] Schwemmer, M., P. Nagler, A. Hanninger, C. Schüller, and T. Korn: *Long-lived spin polarization in n-doped $MoSe_2$ monolayers*. Appl. Phys. Lett., 111:082404, August 2017, ISSN 00036951. Citado 4 vezes nas páginas 23, 78, 80, and 90.

[61] Zhang, Yu, Yuyu Yao, Marshet Getaye Sendeku, Lei Yin, Xueying Zhan, Feng Wang, Zhenxing Wang, and Jun He: *Recent progress in CVD growth of 2D transition metal dichalcogenides and related heterostructures*. Advanced materials, 31(41):1901694, 2019. Citado na página 26.

[62] *Nitto innovation for customers.* `https://www.nitto.com/eu/en/products/semicon/dicing015/`. Accessed: 2023-05-15. Citado na página 27.

[63] Castellanos-Gomez, Andres, Michele Buscema, Rianda Molenaar, Vibhor Singh, Laurens Janssen, Herre S J van der Zant, and Gary A Steele: *Deterministic transfer of two-dimensional materials by all-dry viscoelastic stamping.* 2D Materials, 1(1):011002, 2014. Citado 4 vezes nas páginas 27, 49, 57, and 66.

[64] Li, Hong, Qing Zhang, Chin Chong Ray Yap, Beng Kang Tay, Teo Hang Tong Edwin, Aurelien Olivier, and Dominique Baillargeat: *From bulk to monolayer MoS_2: evolution of raman scattering.* Advanced Functional Materials, 22(7):1385–1390, 2012. Citado na página 29.

[65] Berkdemir, Ayse, Humberto R Gutiérrez, Andrés R Botello-Méndez, Néstor Perea-López, Ana Laura Elías, Chen Ing Chia, Bei Wang, Vincent H Crespi, Florentino López-Urías, Jean Christophe Charlier, *et al.*: *Identification of individual and few layers of WS_2 using Raman spectroscopy.* Scientific reports, 3(1):1755, 2013. Citado na página 29.

[66] Lee, Changgu, Hugen Yan, Louis E Brus, Tony F Heinz, James Hone, and Sunmin Ryu: *Anomalous lattice vibrations of single-and few-layer MoS_2.* ACS nano, 4(5):2695–2700, 2010. Citado na página 29.

[67] Van 't Erve, Olaf M.J., Aubrey T. Hanbicki, Adam L. Friedman, Kathleen M. McCreary, Enrique Cobas, Connie H. Li, Jeremy T. Robinson, and Berend T. Jonker: *Graphene and monolayer transition-metal dichalcogenides: Properties and devices.* Journal of Materials Research, 31(7):845–877, 2016, ISSN 20445326. Citado na página 30.

[68] *WITec focus innovations.* `https://www.witec.de/`. Accessed: 2021-07-28. Citado na página 30.

[69] Ma, Zong Mine, Lili Kou, Yoshitaka Naitoh, Yan Jun Li, and Yasuhiro Sugawara: *The stray capacitance effect in kelvin probe force microscopy using fm, am and heterodyne am modes.* Nanotechnology, 24:22, 2013. Citado 2 vezes nas páginas 36 and 59.

[70] Glatzel, Th, M Ch Lux-Steiner, E Strassburg, A Boag, and Y Rosenwaks: *Principles of kelvin probe force microscopy.* Scanning Probe Microscopy: Electrical and Electromechanical Phenomena at the Nanoscale, pages 113–131, 2007. Citado na página 36.

[71] Jankov, IR, ID Goldman, and Roberto Nunes Szente: *Principles of the kelvin probe force microscopy.* Rev. Bras. Ensino Física, 22:503–509, 2000. Citado na página 36.

[72] Anderson, Mitchell D., Santiago Tarrago Velez, Kilian Seibold, Hugo Flayac, Vincenzo Savona, Nicolas Sangouard, and Christophe Galland: *Two-color pump-probe measurement of photonic quantum correlations mediated by a single phonon*. Phys. Rev. Lett., 120:233601, June 2018. Citado na página 36.

[73] Zhang, Delong, Ping Wang, Mikhail N. Slipchenko, and Ji Xin Cheng: *Fast vibrational imaging of single cells and tissues by stimulated raman scattering microscopy*. Accounts of Chemical Research, 47(8):2282–2290, 2014. Citado na página 36.

[74] McGee, Nigel WE: *The Magneto-Optical Kerr Effect: Theory, Measurement and Application*. PhD thesis, Master Thesis, Eindhoven University of Technology, 1991. Citado na página 42.

[75] Sato, Katsuaki: *Measurement of magneto-optical Kerr effect using piezo-birefringent modulator*. Japanese Journal of Applied Physics, 20(12):2403, 1981. Citado na página 42.

[76] Rojas-Lopez, Rafael R., Juliana C. Brant, Maíra S. O. Ramos, Túlio H. L. G. Castro, Marcos H. D. Guimarães, Bernardo R. A. Neves, and Paulo S. S. Guimarães: *Photoluminescence and charge transfer in the prototypical 2d/3d semiconductor heterostructure MoS_2/GaAs*. Applied Physics Letters, 119(23):233101, 2021. Citado 3 vezes nas páginas 47, 65, and 68.

[77] Yu, Woo Jong, Zheng Li, Hailong Zhou, Yu Chen, Yang Wang, Yu Huang, and Xiangfeng Duan: *Vertically stacked multi-heterostructures of layered materials for logic transistors and complementary inverters*. Nature Materials, 12(3):246–252, 2013, ISSN 14761122. Citado na página 48.

[78] Nalwa, Hari Singh: *A review of molybdenum disulfide (MoS_2) based photodetectors: From ultra-broadband, self-powered to flexible devices*. RSC Advances, 10(51):30529–30602, 2020, ISSN 20462069. Citado na página 48.

[79] Sarkar, Subhendu Sinha, Subhrajit Mukherjee, R. K. Khatri, and Samit K. Ray: *Solution-processed MoS_2 quantum dot/GaAs vertical heterostructure based self-powered photodetectors with superior detectivity*. Nanotechnology, 31:135203, 2020. Citado 4 vezes nas páginas 48, 55, 65, and 71.

[80] Pradeepa, H. L., Praloy Mondal, Aveek Bid, and Jaydeep K. Basu: *Electrical and Chemical Tuning of Exciton Lifetime in Monolayer MoS_2 for Field-Effect Transistors*. ACS Applied Nano Materials, 3(1):641–647, 2020, ISSN 25740970. Citado 2 vezes nas páginas 48 and 51.

[81] Jia, Cheng, Di Wu, Enping Wu, Jiawen Guo, Zhihui Zhao, Zhifeng Shi, Tingting Xu, Xiaowen Huang, Yongtao Tian, and Xinjian Li: *A self-powered high-performance*

photodetector based on a MoS_2/GaAs heterojunction with high polarization sensitivity. Journal of Materials Chemistry C, 7(13):3817–3821, 2019. Citado 4 vezes nas páginas 48, 55, 65, and 71.

[82] Xu, Zhijuan, Shisheng Lin, Xiaoqiang Li, Shengjiao Zhang, Zhiqian Wu, Wenli Xu, Yanghua Lu, and Sen Xu: *Monolayer MoS_2/GaAs heterostructure self-driven photodetector with extremely high detectivity.* Nano Energy, 23:89–96, 2016. Citado 5 vezes nas páginas 48, 53, 55, 65, and 71.

[83] Lin, Shisheng, Xiaoqiang Li, Peng Wang, Zhijuan Xu, Shengjiao Zhang, Huikai Zhong, Zhiqian Wu, Wenli Xu, and Hongsheng Chen: *Interface designed MoS_2/GaAs heterostructure solar cell with sandwich stacked hexagonal boron nitride.* Scientific Reports, 5(May):15103, 2015. Citado 6 vezes nas páginas 48, 53, 55, 65, 71, and 94.

[84] Wang, Qing Hua, Kourosh Kalantar-Zadeh, Andras Kis, Jonathan N. Coleman, and Michael S. Strano: *Electronics and optoelectronics of two-dimensional transition metal dichalcogenides.* Nature Nanotechnology, 7(11):699–712, 2012. Citado na página 48.

[85] Jadczak, J, J Kutrowska-Girzycka, P Kapuściński, Y S Huang, A Wojs, and L Bryja: *Probing of free and localized excitons and trions in atomically thin WSe_2, WS_2, $MoSe_2$ and MoS_2 in photoluminescence and reflectivity experiments.* Nanotechnology, 28(39):395702, 2017. Citado 2 vezes nas páginas 48 and 51.

[86] Buscema, Michele, Gary A. Steele, Herre S J van der Zant, and Andres Castellanos-Gomez: *The effect of the substrate on the Raman and photoluminescence emission of single-layer MoS_2.* Nano Research, 7(4):561–571, 2014, ISSN 19980124. Citado 2 vezes nas páginas 48 and 65.

[87] Sze, S.M. and Kwow K. Ng: *Appendix G Properties of Si and GaAs.* John Wiley & Sons, Ltd, 2006, ISBN 9780470068328. Citado 2 vezes nas páginas 48 and 53.

[88] Zhang, Yan, Yongqiang Yu, Xiaoyan Wang, Guoqing Tong, Longfei Mi, Zhifeng Zhu, Xiangshun Geng, and Yang Jiang: *Solution assembly MoS_2 nanopetals/GaAs n-n homotype heterojunction with ultrafast and low noise photoresponse using graphene as carrier collector.* Journal of Materials Chemistry C, 5(1):140–148, 2017. Citado 2 vezes nas páginas 48 and 55.

[89] Padma, R., Gilho Lee, Jeong Seob Kang, and Seong Chan Jun: *Structural, chemical, and electrical parameters of Au/MoS_2/n-GaAs metal/2D/3D hybrid heterojunction.* Journal of Colloid and Interface Science, 550:48–56, 2019. Citado 3 vezes nas páginas 48, 53, and 55.

[90] Lee, Changgu, Hugen Yan, Louis E. Brus, Tony F. Heinz, James Hone, and Sunmin Ryu: *Anomalous lattice vibrations of single- and few-layer MoS_2.* ACS Nano, 4(5):2695–2700, 2010. Citado 2 vezes nas páginas 49 and 58.

[91] Li, Hong, Qing Zhang, Chin Chong Ray Yap, Beng Kang Tay, Teo Hang Tong Edwin, Aurelien Olivier, and Dominique Baillargeat: *From Bulk to Monolayer MoS_2: Evolution of Raman Scattering.* Advanced Functional Materials, 22(7):1385–1390, 2012. Citado 2 vezes nas páginas 49 and 58.

[92] Cao, Yameng, Sebastian Wood, Filipe Richheimer, J. Blakesley, Robert J. Young, and Fernando A. Castro: *Enhancing and quantifying spatial homogeneity in monolayer WS_2.* Scientific Reports, 11(1):3–12, 2021, ISSN 20452322. Citado na página 49.

[93] Tongay, Sefaattin, Joonki Suh, Can Ataca, Wen Fan, Alexander Luce, Jeong Seuk Kang, Jonathan Liu, Changhyun Ko, Rajamani Raghunathanan, Jian Zhou, Frank Ogletree, Jingbo Li, Jeffrey C Grossman, and Junqiao Wu: *Defects activated photoluminescence in two-dimensional semiconductors: interplay between bound, charged, and free excitons.* Scientific reports, 3:2657, 2013. Citado na página 51.

[94] Saigal, Nihit and Sandip Ghosh: *Evidence for two distinct defect related luminescence features in monolayer MoS_2.* Applied Physics Letters, 109(12):122105, 2016. Citado na página 51.

[95] Greben, Kyrylo, Sonakshi Arora, Moshe G. Harats, and Kirill I. Bolotin: *Intrinsic and Extrinsic Defect-Related Excitons in TMDCs.* Nano Letters, 20(4):2544–2550, 2020. Citado na página 51.

[96] Zhang, Xixia, Shanpeng Wang, Chao Kuei Lee, Cheng Maw Cheng, Jia Chi Lan, Xinru Li, Jie Qiao, and Xutang Tao: *Unravelling the effect of sulfur vacancies on the electronic structure of the MoS_2 crystal.* Physical Chemistry Chemical Physics, 22(38):21776–21783, 2020. Citado 2 vezes nas páginas 51 and 52.

[97] Singh, Akash and Abhishek Kumar Singh: *Origin of n-type conductivity of monolayer MoS_2.* Physical Review B, 99(12):1–5, 2019. Citado 2 vezes nas páginas 51 and 52.

[98] Nonnenmacher, M., M. P. O'Boyle, and H. K. Wickramasinghe: *Kelvin probe force microscopy.* Applied Physics Letters, 58(25):2921–2923, 1991. Citado na página 52.

[99] Melitz, Wilhelm, Jian Shen, Andrew C. Kummel, and Sangyeob Lee: *Kelvin probe force microscopy and its application.* Surface Science Reports, 66(1):1–27, 2011. Citado na página 52.

[100] Keyshar, Kunttal, Morgann Berg, Xiang Zhang, Robert Vajtai, Gautam Gupta, Calvin K. Chan, Thomas E. Beechem, Pulickel M. Ajayan, Aditya D. Mohite, and

Taisuke Ohta: *Experimental Determination of the Ionization Energies of $MoSe_2$, WS_2, and MoS_2 on SiO_2 Using Photoemission Electron Microscopy.* ACS Nano, 11(8):8223–8230, 2017. Citado na página 53.

[101] Guo, Yuzheng and John Robertson: *Band engineering in transition metal dichalcogenides: Stacked versus lateral heterostructures.* Applied Physics Letters, 108(23), 2016. Citado na página 53.

[102] Ryou, Junga, Yong Sung Kim, Santosh Kc, and Kyeongjae Cho: *Monolayer MoS_2 Bandgap Modulation by Dielectric Environments and Tunable Bandgap Transistors.* Scientific Reports, 6(June):29184, 2016. Citado na página 53.

[103] Zerweck, Ulrich, Christian Loppacher, Tobias Otto, Stefan Grafström, and Lukas M. Eng: *Accuracy and resolution limits of kelvin probe force microscopy.* Phys. Rev. B, 71:125424, March 2005. Citado na página 59.

[104] Garrett, Joseph L. and Jeremy N. Munday: *Fast, high-resolution surface potential measurements in air with heterodyne Kelvin probe force microscopy.* Nanotechnology, 27(24), 2016. Citado na página 59.

[105] Axt, Amelie, Ilka M. Hermes, Victor W. Bergmann, Niklas Tausendpfund, and Stefan A.L. Weber: *Know your full potential: Quantitative Kelvin probe force microscopy on nanoscale electrical devices.* Beilstein Journal of Nanotechnology, 9(1):1809–1919, 2018. Citado na página 59.

[106] Berkelbach, Timothy C., Mark S. Hybertsen, and David R. Reichman: *Theory of neutral and charged excitons in monolayer transition metal dichalcogenides.* Phys. Rev. B, 88:045318, July 2013. Citado na página 65.

[107] You, Yumeng, Xiao Xiao Zhang, Timothy C. Berkelbach, Mark S. Hybertsen, David R. Reichman, and Tony F. Heinz: *Observation of biexcitons in monolayer WSe_2.* Nature Physics, 11(6):477–481, 2015, ISSN 17452481. Citado na página 65.

[108] Wilson, Nathan P., Wang Yao, Jie Shan, and Xiaodong Xu: *Excitons and emergent quantum phenomena in stacked 2D semiconductors.* Nature, 599:383–392, November 2021, ISSN 14764687. Citado na página 65.

[109] Refaely-Abramson, Sivan, Diana Y. Qiu, Steven G. Louie, and Jeffrey B. Neaton: *Defect-induced modification of low-lying excitons and valley selectivity in monolayer transition metal dichalcogenides.* Phys. Rev. Lett., 121:167402, October 2018. Citado na página 65.

[110] Watson, Adam J, Wenbo Lu, Marcos H D Guimarães, and Meike Stöhr: *Transfer of large-scale two-dimensional semiconductors: challenges and developments.* 2D Materials, 8(3):032001, May 2021. Citado na página 65.

[111] Jasiński, Jakub, Akshay Balgarkashi, Valerio Piazza, Didem Dede, Alessandro Surrente, Michał Baranowski, Duncan K Maude, Mitali Banerjee, Riccardo Frisenda, Andres Castellanos-Gomez, Anna Fontcuberta i Morral, and Paulina Plochocka: *Strain induced lifting of the charged exciton degeneracy in monolayer MoS_2 on a GaAs nanomembrane*. 2D Materials, 9(4):045006, July 2022. Citado na página 65.

[112] *Emerging van der Waals junctions based on TMDs materials for advanced gas sensors*. Coordination Chemistry Reviews, 447:214151, 2021, ISSN 0010-8545. Citado na página 65.

[113] Bracker, A. S., E. A. Stinaff, D. Gammon, M. E. Ware, J. G. Tischler, D. Park, D. Gershoni, A. V. Filinov, M. Bonitz, F. Peeters, and C. Riva: *Binding energies of positive and negative trions: From quantum wells to quantum dots*. Phys. Rev. B, 72:035332, July 2005. Citado na página 65.

[114] Guimarães, M. H. D. and B. Koopmans: *Spin accumulation and dynamics in inversion-symmetric van der Waals crystals*. Phys. Rev. Lett., 120:266801, June 2018. Citado 5 vezes nas páginas 66, 74, 75, 78, and 84.

[115] Rojas-Lopez, Rafael R, Freddie Hendriks, Caspar H van der Wal, Paulo S S Guimarães, and Marcos H D Guimarães: *Magnetic field control of light-induced spin accumulation in monolayer $MoSe_2$*. 2D Materials, 10(3):035013, 2023. Citado 2 vezes nas páginas 66 and 73.

[116] Yan, Tengfei, Xiaofen Qiao, Xiaona Liu, Pingheng Tan, and Xinhui Zhang: *Photoluminescence properties and exciton dynamics in monolayer WSe_2*. Applied Physics Letters, 105(10):101901, 2014. Citado 3 vezes nas páginas 67, 68, and 71.

[117] Wang, G., L. Bouet, D. Lagarde, M. Vidal, A. Balocchi, T. Amand, X. Marie, and B. Urbaszek: *Valley dynamics probed through charged and neutral exciton emission in monolayer WSe_2*. Phys. Rev. B, 90:075413, August 2014. Citado 2 vezes nas páginas 67 and 68.

[118] Cui, Qiannan, Frank Ceballos, Nardeep Kumar, and Hui Zhao: *Transient absorption microscopy of monolayer and bulk WSe_2*. ACS Nano, 8(3):2970–2976, 2014. Citado 2 vezes nas páginas 67 and 68.

[119] Yan, Tengfei, Siyuan Yang, Dian Li, and Xiaodong Cui: *Long valley relaxation time of free carriers in monolayer* wse_2. Phys. Rev. B, 95:241406, June 2017. Citado 2 vezes nas páginas 67 and 68.

[120] Ceballos, Frank, Peymon Zereshki, and Hui Zhao: *Separating electrons and holes by monolayer increments in van der Waals heterostructures*. Phys. Rev. Mater., 1:044001, September 2017. Citado na página 67.

[121] Wu, Lingling, Yuzhong Chen, Hongzhi Zhou, and Haiming Zhu: *Ultrafast energy transfer of both bright and dark excitons in 2D van der Waals heterostructures beyond dipolar coupling.* ACS Nano, 13(2):2341–2348, 2019. Citado na página 67.

[122] Li, Yujie, Hongzhi Zhou, Yuzhong Chen, Yida Zhao, and Haiming Zhu: *Efficient hot-electron extraction in two-dimensional semiconductor heterostructures by ultrafast resonant transfer.* The Journal of Chemical Physics, 153(4), July 2020. Citado na página 67.

[123] Wang, Pengzhi, Yongsheng Wang, Ang Bian, Shengcai Hao, Qing Miao, Xiaoxian Zhang, Jiaqi He, Dawei He, and Hui Zhao: *Energy transfer in a type-I van der Waals heterostructure of $WSe_2/PtSe_2$.* 2D Materials, 9(3):035019, 2022. Citado na página 67.

[124] Zereshki, Peymon, Peng Yao, Dawei He, Yongsheng Wang, and Hui Zhao: *Interlayer charge transfer in ReS_2/WS_2 van der Waals heterostructures.* Phys. Rev. B, 99:195438, May 2019. Citado na página 67.

[125] Tangi, Malleswararao, Pawan Mishra, Chien Chih Tseng, Tien Khee Ng, Mohamed Nejib Hedhili, Dalaver H. Anjum, Mohd Sharizal Alias, Nini Wei, Lain Jong Li, and Boon S. Ooi: *Band alignment at GaN/single-layer WSe_2 interface.* ACS Applied Materials & Interfaces, 9(10):9110–9117, 2017. Citado na página 67.

[126] Robert, C., D. Lagarde, F. Cadiz, G. Wang, B. Lassagne, T. Amand, A. Balocchi, P. Renucci, S. Tongay, B. Urbaszek, and X. Marie: *Exciton radiative lifetime in transition metal dichalcogenide monolayers.* Phys. Rev. B, 93:205423, May 2016. Citado na página 68.

[127] Li, Jing, M. Goryca, K. Yumigeta, H. Li, S. Tongay, and S. A. Crooker: *Valley relaxation of resident electrons and holes in a monolayer semiconductor: Dependence on carrier density and the role of substrate-induced disorder.* Phys. Rev. Mater., 5:044001, April 2021. Citado na página 68.

[128] Pogna, Eva A. A., Margherita Marsili, Domenico De Fazio, Stefano Dal Conte, Cristian Manzoni, Davide Sangalli, Duhee Yoon, Antonio Lombardo, Andrea C. Ferrari, Andrea Marini, Giulio Cerullo, and Deborah Prezzi: *Photo-induced bandgap renormalization governs the ultrafast response of single-layer MoS_2.* ACS Nano, 10(1):1182–1188, 2016. Citado na página 70.

[129] Akmaev, M. A., M. V. Kochiev, A. I. Duleba, M. V. Pugachev, A. Yu Kuntsevich, and V. V. Belykh: *Nonexponential photoluminescence dynamics in an inhomogeneous ensemble of excitons in WSe_2 monolayers.* JETP Letters, 112:607–614, November 2020, ISSN 10906487. Citado na página 71.

[130] Zhang, Xiao Xiao, Yumeng You, Shu Yang Frank Zhao, and Tony F. Heinz: *Experimental evidence for dark excitons in monolayer WSe_2*. Phys. Rev. Lett., 115:257403, December 2015. Citado na página 71.

[131] Žutić, Igor, Jaroslav Fabian, and S. Das Sarma: *Spintronics: Fundamentals and applications*. Rev. Mod. Phys., 76:323–410, Apr 2004. Citado na página 71.

[132] Xu, Xiaodong, Wang Yao, Di Xiao, and Tony F Heinz: *Spin and pseudospins in layered transition metal dichalcogenides*. Nature Physics, 10(5):343–350, 2014. Citado na página 71.

[133] Salis, Gian, Y Kato, K Ensslin, DC Driscoll, AC Gossard, and DD Awschalom: *Electrical control of spin coherence in semiconductor nanostructures*. Nature, 414(6864):619–622, 2001. Citado na página 71.

[134] Gong, Zhirui, Gui Bin Liu, Hongyi Yu, Di Xiao, Xiaodong Cui, Xiaodong Xu, and Wang Yao: *Magnetoelectric effects and valley-controlled spin quantum gates in transition metal dichalcogenide bilayers*. Nature communications, 4(1):2053, 2013. Citado na página 71.

[135] Žutić, Igor, Gaofeng Xu, Markus Lindemann, Paulo E Faria Junior, Jeongsu Lee, Velimir Labinac, Kristian Stojšić, Guilherme M Sipahi, Martin R Hofmann, and Nils C Gerhardt: *Spin-lasers: spintronics beyond magnetoresistance*. Solid State Communications, 316:113949, 2020. Citado na página 71.

[136] Lindemann, Markus, Gaofeng Xu, Tobias Pusch, Rainer Michalzik, Martin R Hofmann, Igor Žutić, and Nils C Gerhardt: *Ultrafast spin-lasers*. Nature, 568(7751):212–215, 2019. Citado na página 71.

[137] Xu, Xiaodong, Wang Yao, Di Xiao, and Tony F. Heinz: *Spin and pseudospins in layered transition metal dichalcogenides*. Nat. Phys., 10:343–350, May 2014, ISSN 17452481. Citado na página 74.

[138] Liu, Yuan, Nathan O. Weiss, Xidong Duan, Hung Chieh Cheng, Yu Huang, and Xiangfeng Duan: *Van der Waals heterostructures and devices*. Nat. Rev. Mater., 1:16042, July 2016, ISSN 20588437. Citado na página 74.

[139] Schaibley, John R., Hongyi Yu, Genevieve Clark, Pasqual Rivera, Jason S. Ross, Kyle L. Seyler, Wang Yao, and Xiaodong Xu: *Valleytronics in 2D materials*. Nat. Rev. Mater., 1:16055, August 2016, ISSN 20588437. Citado na página 74.

[140] Wang, G., L. Bouet, M. M. Glazov, T. Amand, E. L. Ivchenko, E. Palleau, X. Marie, and B. Urbaszek: *Magneto-optics in transition metal diselenide monolayers*. 2D Mater., 2:034002, June 2015, ISSN 20531583. Citado na página 74.

[141] Rybkovskiy, D. V., I. C. Gerber, and M. V. Durnev: *Atomically inspired $k \cdot p$ approach and valley Zeeman effect in transition metal dichalcogenide monolayers.* Phys. Rev. B, 95:155406, April 2017. Citado na página 74.

[142] Wang, G., E. Palleau, T. Amand, S. Tongay, X. Marie, and B. Urbaszek: *Polarization and time-resolved photoluminescence spectroscopy of excitons in $MoSe_2$ monolayers.* Appl. Phys. Lett., 106:112101, March 2015, ISSN 00036951. Citado 4 vezes nas páginas 74, 78, 80, and 90.

[143] Godde, T., D. Schmidt, J. Schmutzler, M. Aßmann, J. Debus, F. Withers, E. M. Alexeev, O. Del Pozo-Zamudio, O. V. Skrypka, K. S. Novoselov, M. Bayer, and A. I. Tartakovskii: *Exciton and trion dynamics in atomically thin $MoSe_2$ and WSe_2: Effect of localization.* Phys. Rev. B, 94:165301, October 2016. Citado 4 vezes nas páginas 74, 78, 80, and 90.

[144] Wang, Wei and Xuedan Ma: *Strain-induced trapping of indirect excitons in $MoSe_2/WSe_2$ heterostructures.* ACS Photonics, 7:2460–2467, September 2020, ISSN 23304022. Citado na página 74.

[145] Kumar, Nardeep, Jiaqi He, Dawei He, Yongsheng Wang, and Hui Zhao: *Valley and spin dynamics in $MoSe_2$ two-dimensional crystals.* Nanoscale, 6:12690–12695, November 2014, ISSN 20403372. Citado na página 74.

[146] Kumar, Nardeep, Qiannan Cui, Frank Ceballos, Dawei He, Yongsheng Wang, and Hui Zhao: *Exciton-exciton annihilation in $MoSe_2$ monolayers.* Phys. Rev. B, 89:125427, March 2014. Citado na página 74.

[147] Ye, Jialiang, Tengfei Yan, Binghui Niu, Ying Li, and Xinhui Zhang: *Nonlinear dynamics of trions under strong optical excitation in monolayer $MoSe_2$.* Sci. Rep., 8:2389, December 2018, ISSN 20452322. Citado na página 74.

[148] Zhu, C. R., K. Zhang, M. Glazov, B. Urbaszek, T. Amand, Z. W. Ji, B. L. Liu, and X. Marie: *Exciton valley dynamics probed by Kerr rotation in WSe_2 monolayers.* Phys. Rev. B, 90:161302, October 2014. Citado 2 vezes nas páginas 74 and 75.

[149] Li, Ying, Xia Wei, Jialiang Ye, Guihao Zhai, Kaiyou Wang, and Xinhui Zhang: *Gate-controlled spin relaxation in bulk WSe_2 flakes.* AIP Advances, 10:045315, April 2020, ISSN 21583226. Citado 2 vezes nas páginas 74 and 75.

[150] Zhang, Yan, Keisuke Shinokita, Kenji Watanabe, Takashi Taniguchi, Yuhei Miyauchi, and Kazunari Matsuda: *Magnetic field induced inter-valley trion dynamics in monolayer 2D semiconductor.* Adv. Funct. Mater., 31:2006064, January 2021, ISSN 16163028. Citado 2 vezes nas páginas 74 and 80.

[151] Benítez, L. Antonio, Juan F. Sierra, Williams Savero Torres, Aloïs Arrighi, Frédéric Bonell, Marius V. Costache, and Sergio O. Valenzuela: *Strongly anisotropic spin relaxation in graphene-transition metal dichalcogenide heterostructures at room temperature.* Nat. Phys., 14:303–308, March 2018, ISSN 17452481. Citado na página 74.

[152] Sierra, Juan F., Jaroslav Fabian, Roland K. Kawakami, Stephan Roche, and Sergio O. Valenzuela: *Van der Waals heterostructures for spintronics and opto-spintronics.* Nat. Nanotech., 16:856–868, August 2021, ISSN 17483395. Citado na página 74.

[153] Dal Conte, S., F. Bottegoni, E. A. A. Pogna, D. De Fazio, S. Ambrogio, I. Bargigia, C. D'Andrea, A. Lombardo, M. Bruna, F. Ciccacci, A. C. Ferrari, G. Cerullo, and M. Finazzi: *Ultrafast valley relaxation dynamics in monolayer MoS_2 probed by nonequilibrium optical techniques.* Phys. Rev. B, 92:235425, December 2015. Citado na página 75.

[154] Mai, Cong, Andrew Barrette, Yifei Yu, Yuriy G. Semenov, Ki Wook Kim, Linyou Cao, and Kenan Gundogdu: *Many-body effects in valleytronics: Direct measurement of valley lifetimes in single-layer MoS_2.* Nano Lett., 14:202–206, January 2014, ISSN 15306984. Citado na página 80.

[155] Schellekens, Adrianus Johannes: *Manipulating spins : novel methods for controlling magnetization dynamics on the ultimate timescale.* PhD thesis, Eindhoven University of Technology, 2014. `www.tue.nl/taverne`, ISBN: 978-90-386-3586-6. Citado na página 84.

[156] WoŹniak, Tomasz, Paulo E. Faria Junior, Gotthard Seifert, Andrey Chaves, and Jens Kunstmann: *Exciton g factors of van der Waals heterostructures from first-principles calculations.* Phys. Rev. B, 101:235408, June 2020. Citado na página 85.

[157] Gu, Jie, Biswanath Chakraborty, Mandeep Khatoniar, and Vinod M Menon: *A room-temperature polariton light-emitting diode based on monolayer WS_2.* Nature Nanotechnology, 14(11):1024–1028, 2019. Citado na página 94.

[158] Huang, Le, Nengjie Huo, Yan Li, Hui Chen, Juehan Yang, Zhongming Wei, Jingbo Li, and Shu Shen Li: *Electric-field tunable band offsets in black phosphorus and MoS_2 van der Waals pn heterostructure.* The journal of physical chemistry letters, 6(13):2483–2488, 2015. Citado na página 95.

[159] Hu, Fengrui and Zhe Fei: *Recent progress on exciton polaritons in layered transition-metal dichalcogenides.* Advanced Optical Materials, 8(5):1901003, 2020. Citado na página 95.

[160] Dufferwiel, Scott, Thomas P Lyons, Dmitry D Solnyshkov, Aurélien AP Trichet, Freddie Withers, Stefan Schwarz, Guillaume Malpuech, Jason M Smith, Konstantin S Novoselov, Maurice S Skolnick, *et al.*: *Valley-addressable polaritons in atomically thin semiconductors*. Nature Photonics, 11(8):497–501, 2017. Citado na página 95.

[161] Zhang, Fu, Boyang Zheng, Amritanand Sebastian, David H Olson, Mingzu Liu, Kazunori Fujisawa, Yen Thi Hai Pham, Valery Ortiz Jimenez, Vijaysankar Kalappattil, Leixin Miao, *et al.*: *Monolayer vanadium-doped tungsten disulfide: a room-temperature dilute magnetic semiconductor*. Advanced Science, 7(24):2001174, 2020. Citado na página 95.

[162] Li, Qi, Xiaoxu Zhao, Longjiang Deng, Zhongtai Shi, Sheng Liu, Qilin Wei, Linbo Zhang, Yingchun Cheng, Li Zhang, Haipeng Lu, *et al.*: *Enhanced valley Zeeman splitting in Fe-doped monolayer MoS_2*. ACS Nano, 14(4):4636–4645, 2020. Citado na página 95.

[163] Ahn, Ethan C: *2D materials for spintronic devices*. npj 2D Materials and Applications, 4(1):17, 2020. Citado na página 95.

[164] Luo, Yunqiu Kelly, Jinsong Xu, Tiancong Zhu, Guanzhong Wu, Elizabeth J McCormick, Wenbo Zhan, Mahesh R Neupane, and Roland K Kawakami: *Opto-valleytronic spin injection in monolayer MoS_2/few-layer graphene hybrid spin valves*. Nano Letters, 17(6):3877–3883, 2017. Citado na página 95.

APENDIX A - List of Publications

1. R.R. Rojas-Lopez, J.C. Brant, M.S.O. Ramos, T.H.L.G. Castro, M.H.D. Guimarães, B.R.A. Neves, P.S.S. Guimarães, *Photoluminescence and charge transfer in the prototypical 2D/3D semiconductor heterostructure $MoS_2/GaAs$*, Applied Physics Letters **119**, 233101 (2021) [Chapter 3].

2. R.R. Rojas-Lopez, F. Hendriks, C.H. van der Wal,P.S.S. Guimarães, M.H.D. Guimarães, *Charge dynamics in the 2D/3D semiconductor heterostructure $WSe_2/GaAs$*, Submitted, [Chapter 4].

3. R.R. Rojas-Lopez, F. Hendriks, C.H. van der Wal, P.S.S. Guimarães, M.H.D. Guimarães, *Magnetic field control of light-induced spin accumulation in monolayer $MoSe_2$*, 2D Materials **10**, 035013 (2023) [Chapter 5].

4. F. Hendriks, R.R. Rojas-Lopez, B. Koopmans, M.H.D. Guimarães, *Electrically-tunable magnetization dynamics in the van der Waals ferromagnetic semiconductor*, Submitted, [not in this thesis].